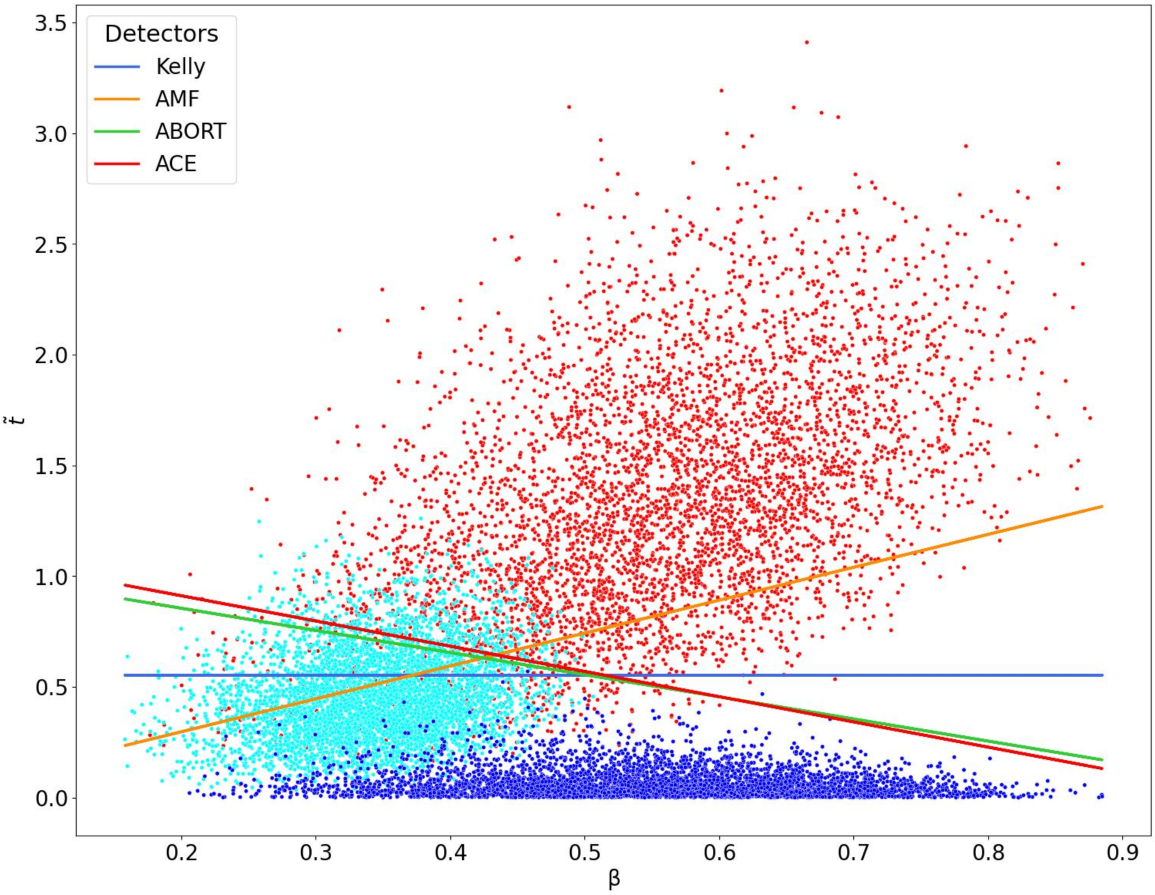

Leveraging Machine Learning in CFAR Detectors

Analyzing Cluster Characteristics and Developing Machine Learning Based Detectors in the CFAR Feature Plane

Master's Thesis in Complex Adaptive Systems

MALIN JOHANSSON & RASMUS REDEBORN

DEPARTMENT OF ELECTRICAL ENGINEERING
CHALMERS UNIVERSITY OF TECHNOLOGY
Gothenburg, Sweden 2025
www.chalmers.se

MASTER'S THESIS 2025

Leveraging Machine Learning in CFAR Detectors

Analyzing Cluster Characteristics and Implementing Machine Learning Based Detectors in the CFAR Feature Plane

MALIN JOHANSSON & RASMUS REDEBORN

Department of Electrical Engineering
CHALMERS UNIVERSITY OF TECHNOLOGY
Gothenburg, Sweden 2025

Leveraging Machine Learning in CFAR Detectors
Analyzing Cluster Characteristics and Implementing Machine Learning Based Detectors in the CFAR Feature Plane
MALIN JOHANSSON & RASMUS REDEBORN

Supervisors: Patrik Dammert, Anton Karlsson Anders Åhlander, SAAB AB
Examiner: Tomas McKelvey, Department of Electrical Engineering

Master's Thesis 2025
Department of Electrical Engineering
Chalmers University of Technology
SE-412 96 Gothenburg
Telephone +46 31 772 1000

Cover: Traditional model-based detectors in the CFAR Feature Plane.

Typeset in LaTeX
Printed by TeknologTryck
Gothenburg, Sweden 2025

Leveraging Machine Learning in CFAR Detectors
Analyzing Cluster Characteristics and Implementing Machine Learning Based Detectors in the CFAR Feature Plane
Malin Johansson & Rasmus Redeborn
Department of Electrical Engineering
Chalmers University of Technology

Abstract

Within the field of radar detection, a property called constant false alarm rate (CFAR) is of great importance. This property is used when, for example, creating generalized likelihood ratio test(GLRT)-based CFAR adaptive detectors. By using the statistics of these detectors, the authors of the article *CFAR Feature Plane: A Novel Framework for the Analysis and Design of Radar Detectors* have mapped radar data to a two dimensional feature space, called CFAR feature plane. During this work, this mapping chain was used to map data of high dimension to the plane, making it possible to compare clusters that forms in the feature plane. For larger steering vectors as input data (dimension of evaluated cell), there were less characteristics present in terms of amplitude and rotation between clusters of targets and clutter.

Furthermore, multiple estimations of the covariance matrix were used, both in terms of the amount of samples, but also together with regularization techniques, such as diagonal loading and fast maximum likelihood estimation. What could be seen was that the greater amount of data used for estimation, or by utilizing one of the regularization techniques, the more distinct clusters where formed in the CFAR feature plane, making the final classification easier. The main goal of this project was to implement different machine learning algorithms, trained in the feature plane, to investigate if it was possible to get a more robust detector in terms of mismatched targets, than the traditional model based ones, such as Kelly's detector.

Characteristics for the clusters, how each cluster is distributed in feature space, directly affect detector performance. The larger the steering vector, the more intersection between clusters, causing the trained machine learning detectors to adapt to the behavior of a Kelly's detector, performing relatively well. As for the smaller sizes of input data, it is possible to create machine learning detectors that performs better than the traditional ones, both in terms of perfect matched and mismatched targets. Such algorithms are multilayered perceptrons and symbolic classifiers.

Keywords: Radar, CFAR, CFAR Feature Plane, Detection, Classification, Invariant Statistics, Machine Learning, Covariance Matrix Estimation, Diagonal Loading, Fast Maximum Likelihood Estimation, Multilayered Perceptron, Symbolic Classifier

Acknowledgements

Firstly we would like to thank our supervisors Patrik Dammert, Anton Karlsson and Anders Åhlander at Saab for all the great support and ideas throughout this work. The weekly meetings have been of great help for us. We also want to thank Maria Stegberg and the rest of the X-Innovation Lab for the time and them including us in their team. Finally, we want to thank our examiner Tomas McKelvey for taking on this project and for the support and discussions.

Malin Johansson & Rasmus Redeborn, Gothenburg, May 2025

List of Acronyms

Below is the list of acronyms that have been used throughout this thesis listed in alphabetical order:

ABORT	Adaptive Beamformer Orthogonal Rejection Test
ACE	Adaptive Coherence Detector
AI	Artificial Intelligence
ANN	Artificial Neural Network
AMF	Adaptive Matched Filter
AUC	Area Under Curve
BCE	Binary Cross Entropy
CA-CFAR	Cell-Averaging Constant False Alarm Rate
CFAR	Constant False Alarm Rate
CFAR-FP	Constant False Alarm Rate Feature Plane
CPI	Coherent Processing Interval
CUT	Cell Under Test
CW	Continuous Waveform
DL	Diagonal Loading
ED	Energy Detector
FML	Fast Maximum Likelihood
GLRT	Generalized Likelihood Ratio Test
GP	Genetic Programming
kNN	k-Nearest Neighbors
ML	Machine Learning
MLP	Multilayer Perceptron
MTI	Moving Target Indication
NP	Neyman-Pearson
PDF	Probability Density Function
RMB loss	Reed, Mallet, and Brennan loss
ROC	Receiver Operating Characteristics
SCR	Signal-to-Clutter Ratio
SINR	Signal-to-Interference-plus-Noise Ratio
SNR	Signal-to-Noise Ratio
SR	Symbolic Regression
STAP	Space-Time Adaptive Processing
SVM	Support Vector Machine
ULA	Uniform Linear Array

Contents

List of Acronyms **ix**

List of Figures **xiii**

List of Tables **xvii**

1 Introduction **1**
- 1.1 Purpose 1
- 1.2 Research Questions 1
- 1.3 Limitations 2
- 1.4 Previous Work 2

2 Theory **3**
- 2.1 Radar Fundamentals 3
  - 2.1.1 Interference and Waveforms 4
  - 2.1.2 Ambiguities 6
    - 2.1.2.1 Range 6
    - 2.1.2.2 Doppler 7
  - 2.1.3 Target Detection 8
- 2.2 Constant False Alarm Rate 10
  - 2.2.1 CFAR-Processors 10
  - 2.2.2 CFAR Feature Plane 10
  - 2.2.3 Known Detectors 12
  - 2.2.4 Cluster Characteristics 12
- 2.3 Space-Time Adaptive Processing 14
- 2.4 Sample Covariance Estimation 15
  - 2.4.1 Diagonal Loading 16
  - 2.4.2 Fast Maximum Likelihood Estimation 17
- 2.5 Machine Learning 18
  - 2.5.1 Artificial Neural Networks 18
  - 2.5.2 K-nearest neighbors 19
  - 2.5.3 Symbolic Classification 19
  - 2.5.4 Support Vector Machine 19

3 Methods **21**
- 3.1 Data Generation 21
  - 3.1.1 Radar Configurations 23

3.2 Cluster Characteristics 23
3.3 Detection Models 24
  3.3.1 Machine Learning Implementations 24
  3.3.2 Cases for ML 24
  3.3.3 Implementations 25
  3.3.4 Evaluation 26

4 Results **27**
4.1 Cluster Characteristics 27
4.2 Detection Models 33
  4.2.1 Traditional Detectors 33
  4.2.2 Detector Performance Evaluation 35
    4.2.2.1 Case 1 36
    4.2.2.2 Case 2 39
    4.2.2.3 Final Evaluation 42

5 Conclusion **47**
5.1 Future work 48

Bibliography **49**

A Eigenvalues and Clusters **I**

B ML detectors - 1 antenna **VII**

C ML detectors - 20 antennas **XIII**

D Final Evaluation **XIX**

List of Figures

2.1 Emitted pulses and returns pulses with mentioned measures. 5
2.2 Radar datacube, STAP dimension marked in blue. 6
2.3 Emitted pulses M, M+1, M+2 and returns from targets T1 and T2. . 6
2.4 Doppler phenomena, higher frequencies in direction of velocity. 7
2.5 Layered representation of the mapping chain. 11
2.6 Schematic overview of ULA receiving signal from clutter patches in the circle Ω. 14
2.7 Eigenvalues for covariance matrices for radar configuration of N = 12 and M = 12. 17
2.8 Eigenvalues for covariance matrices for radar configuration of N = 12 and M = 12. **S** estimated with using FML. 17
2.9 Structure of an ANN with two hidden layers. 18
2.10 Visual description of how SVM works. 20

4.1 Gaussian clutter and targets mapped to the CFAR-FP for different SNR. 28
4.2 Gaussian clutter and targets mapped to the CFAR-FP for different values for K. SNR = 15 dB. 29
4.3 Gaussian clutter and targets for different methods of estimating **S**. SNR = 15 dB. 30
4.4 Clusters and eigenvalues of **S** for K = NM, N = 20, M = 20, SNR = 15 dB. Orange lines is eigenvalues for estimated covariance matrix. Green lines is eigenvalues for actual covariance and blue lines is the eigenvalues for clutter only covariance matrix. 31
4.5 Cluster behavior for N = 20 M = 20 for different levels of SNR, K = 2NM. 32
4.6 Varying length of steering vector, K = 2NM. 32
4.7 Asymptotic behavior of the center of matched and mismatched clusters, SNR = 15 dB, K = 2NM. 33
4.8 Data used for threshold tuning. 34
4.9 Traditional detectors in the CFAR-FP. 34
4.10 ROC-curves for SNR = 15 dB. 35
4.11 ROC-curves for SNR = 10, 15 and 20 dB combined. 35
4.12 Results for K = 2NM, **S** diagonally loaded. (a) SNR = 14-20 dB, (b)-(c) SNR = 16 dB, (d)-(e) SNR = 10-20 dB. 37

4.13 Results for K = 0.5NM, **S** FML estimate. (a) SNR = 14-20 dB, (b)-(c) SNR = 16 dB, (d)-(e) SNR = 10-20 dB. 38
4.14 Results for K = 2NM, **S** diagonally loaded. (a) SNR = 14-20 dB, (b)-(c) SNR = 16 dB, (d)-(e) SNR = 10-20 dB. 40
4.15 Results for K = 0.5NM, **S** FML estimate. (a) SNR = 14-20 dB, (b)-(c) SNR = 16 dB, (d)-(e) SNR = 10-20 dB. 41
4.16 Results for K = 0.5NM for Case 2, **S** FML estimated with detectors trained on K = 0.5NM with FML for Case 1. (a) SNR = 14-20 dB, (b)-(c) SNR = 16 dB, (d)-(e) SNR = 10-20 dB. 43
4.17 Results for K = 2NM for Case 1 with detectors trained on K = 0.5NM with FML for Case 1. (a) SNR = 14-20 dB, (b)-(c) SNR = 16 dB, (d)-(e) SNR = 10-20 dB. 44
4.18 Results for K = 2NM for Case 2 with detectors trained on K = 0.5NM with FML for Case 1. (a) SNR = 14-20 dB, (b)-(c) SNR = 16 dB, (d)-(e) SNR = 10-20 dB. 45

A.1 Eigenvalues and clusters at different values of K, N = 1 and M = 20, SNR = 16 dB. I
A.2 Clustering results for diagonally loaded at different values of K, N = 1 and M = 20, SNR = 16 dB. II
A.3 Eigenvalues and clusters at different values of K using FML, N = 1 and M = 20, SNR = 16 dB. III
A.4 Eigenvalues and clusters at different values of K, N = 20 and M = 20, SNR = 16 dB. IV
A.5 Eigenvalues and clusters at different values of K using DL, N = 20 and M = 20, SNR = 16 dB. V
A.6 Eigenvalues and clusters at different values of K using FML, N = 20 and M = 20, SNR = 16 dB. VI

B.1 Different detectors in CFAR-FP for 1 antenna VIII
B.2 K = 0.5NM, Diagonally loaded IX
B.3 K = NM, Diagonally loaded IX
B.4 K = NM, FML estimate X
B.5 K = 2NM, FML estimate X
B.6 K = 2NM XI

C.1 Different detectors in the CFAR-FP for 20 antennas XIV
C.2 K = 0.5NM, Diagonally loaded XV
C.3 K = NM, Diagonally loaded XV
C.4 K = NM, FML estimate XVI
C.5 K = 2NM, FML estimate XVI
C.6 K = 2NM XVII

D.1 Different detectors in the CFAR-FP with detectors trained on K = 0.5NM with FML for Case 1. XX
D.2 K = 0.5NM, Diagonally loaded, Case 1 XXI
D.3 K = 0.5NM, Diagonally loaded, Case 2 XXI

D.4 K = NM, Diagonally loaded, Case 1 XXII
D.5 K = NM, Diagonally loaded, Case 2 XXII
D.6 K = NM, FML estimated, Case 1 XXIII
D.7 K = NM, FML estimated, Case 2 XXIII
D.8 K = 2NM, Diagonally Loaded, Case 1 XXIV
D.9 K = 2NM, Diagonally loaded, Case 2 XXIV
D.10 K = 2NM, FML estimated, Case 1 XXV
D.11 K = 2NM, FML estimated, Case 2 XXV

List of Tables

2.1 Decision boundary and statistics of some traditional detectors. 12

3.1 All simulated cases. 23
3.2 Cases used for training and evaluation of ML algorithms. 25

4.1 Number of neighbors and corresponding P_{FA} for kNN. 36
4.2 Value of γ_{SVM} and corresponding P_{FA} for SVM. 36
4.3 Number of neighbors and corresponding P_{FA} for kNN. 39
4.4 Value of γ_{SVM} and corresponding P_{FA} for SVM. 39

1

Introduction

In the paper, *CFAR Feature Plane: A Novel Framework for the Analysis and Design of Radar Detectors* from 2020, the authors presented a new way of improving either robustness or selectivity for GLRT-based constant false alarm rate adaptive detectors [1]. This is by mapping data to a feature plane using maximum invariant statistics and when only using the raw sample covariance matrix estimation this leads to all detectors represented in the plane fulfilling the CFAR property. The data considered for mapping are clutter and noise, target signals, and mismatched target signals, which forms clusters in the CFAR feature plane (CFAR-FP). In the 2-D plane, detection becomes a binary classification problem, and this creates opportunities for the development of new data-driven detectors.

1.1 Purpose

This project aims to evaluate traditional model-based algorithms for detection in the CFAR-FP and use them as a benchmark for assessing detector performance. The behavior of clusters formed from radar data mapped to CFAR-FP will be analyzed and characterized. Moreover, new data-driven detectors are going to be implemented using machine learning and compared to the traditional detectors. Furthermore, the detectors will be tested on mismatched targets with the purpose of evaluating robustness.

1.2 Research Questions

The specific issues that will be investigated correspond to how well machine learning algorithms can perform compared to traditional model based detection methods, as well as the behavior of the clusters formed in CFAR-FP. This is to draw conclusions regarding how suitable the CFAR-FP is when performing target detection, and for the development of new detectors. The questions that will be answered during this Master's thesis are listed below.

- How well do data-driven machine learning detectors perform in comparison to the traditional model-based detectors, such as Kelly and AMF?
- How will the clusters in the CFAR-FP be affected by:
    - Level of mismatch and Signal-to-Noise-Ratio?
    - Different estimations of the sample covariance matrix, with different amounts of secondary data, together with methods of regularization?
    - The size of the steering vector for the chosen radar case?

1.3 Limitations

This work is limited to the detection of a target signal in two different radar configurations. The different configurations consist of 20 pulses, but for two different amounts of antennas. Moreover, the clutter covariance used in this study is simplified and follows a gaussian distribution and clutter returns are received only from the angular range $\left[\frac{-\pi}{2}, \frac{\pi}{2}\right]$. Furthermore, earth surface is assumed to be homogeneous and constant range to clutter points are used to simplify the clutter modeling. Regarding target modeling, only one target per range bin will be considered and the final implementations will be evaluated on only two levels of mismatched targets to ensure reliable comparison between detectors.

1.4 Previous Work

The foundation for this work is the invariant statistical mapping for CFAR-FP presented in article *CFAR Feature Plane: A Novel Framework for the Analysis and Design of Radar Detectors*. There are published detector implementations for CFAR-FP such as [2], [3] and even proposed machine learning implementations such as [4]. Regularization techniques for sample covariance matrix estimations can be found in [5] and [6].

2

Theory

Some background knowledge will be presented to understand the tasks faced. This includes basic radar principles, theory about CFAR and the feature plane, how the covariance matrix can be estimated and information about different machine learning algorithms. All of this will be presented and explained in this chapter.

2.1 Radar Fundamentals

What used to be a detection instrument designed for military and civilian vehicles, has now become a highly technological computer system with new applications discovering rapidly [7]. From determining the presence and range of a target such as an airborne enemy or a floating iceberg at sea to high precision detection, ranging, tracking, imaging, and classifying in varying settings.

Pulse-Doppler radar systems emits electromagnetic waves in form of radio frequency pulses [7]. Electromagnetic waves propagate through space with the speed of light c and the wave is reflected by objects. If the transmitted signal is reflected from an object, called a target, the range can be determined based on the time for the propagation, as

$$R = \frac{c\Delta t}{2}, \tag{2.1}$$

where R is the range, c is the speed of light and Δt the time of the propagation for the wave. The radar device is built up by several subsystems. The transmitter generates the waves, which through the antenna are introduced to the air. The system thereafter switches to listening mode and reflected signals are detected at the receiver. The signal is then passed through an analog-digital converter. Before or after this conversion, depending on frequency, the high-frequency carrier wave is removed and the resulting signal is then analyzed by signal processor.

The signal also contains reflections from unwanted sources, such as surfaces at ground level or in the atmosphere, which is called clutter [7]. In addition to return signal and clutter, there will be thermal, "white", noise induced by particles with a temperature above 0 K. These particles have a random thermal motion and radiate electromagnetic waves in all frequencies which will be recorded by the receiver. The source inducing the highest level of noise is actually the receiver itself. The power of the thermal noise, P_n, induced by receiver is given by

$$P_n = kT_0F_sB \tag{2.2}$$

where k is Boltzmann's constant, T_0 the standard temperature (290 K), F_s the system noise figure and B the receiver bandwidth.

Performance of radar systems is highly dependent on signal strength and specially on the relation between interfering signals and target signal [7]. The radar equation describes received target signal power from illuminated target, P_r, as

$$P_r = \frac{P_tG_tG_r\lambda^2\sigma}{(4\pi)^3R^4} \tag{2.3}$$

where P_t is the transmitted power, G_t the transmitted gain, G_r the received gain, λ the wavelength and σ the radar cross section. The radar equation is utilized to determine operable ranges, but primarily it can be use do derive useful performance measures as signal-to-noise ratio (SNR), signal-to-clutter ratio (SCR), or total signal-to-interference ratio (SINR). By dividing received target signal power with power of the noise the SNR can be calculated as

$$SNR = \frac{P_tG_tG_r\lambda^2\sigma}{(4\pi)^3R^4kT_0F_sB}. \tag{2.4}$$

2.1.1 Interference and Waveforms

Two or more waves at the same position, time, and with shared frequency will add up to a resulting wave with a complex sum [7]. This means that the amplitude of each in-phase wave will contribute to the total amplitude, this is called constructive interference. If one of the signals is phase-shifted this means that the resulting amplitude will be less than the sum, and if two signals are shifted π radians resulting signal is canceled out, this is called destructive interference. Considering an array of N antenna elements all emitting an electromagnetic signal of equal amplitude and frequency, at a distance far away in perpendicular relation to the platform, these signals will be in phase. This will result in constructive interference and a total amplitude of N times the amplitude of one signal generated by one element. In other angular directions, there will of course be destructive interference and as the angle of deviation from the normal decreases, the amplitude will decrease until it reaches zero. The angle (in both directions) at the point where the amplitude reaches zero defines what is called the main beam or the main lobe. This lobe contains most of the emitted power and the other lobes, called side lobes, have descending power.

In addition to the main and side lobes, there will be radiation in the opposite direction, called back lobes. However, this is often not considered and the systems are designed to attenuate these back lobes making their impact negligible [8]. If the relative phase of the signals differs there will be destructive interference in the perpendicular direction and by adjusting the phases properly the system can make the main lobe scan through space in the angular direction.

The emitted signals can generally be divided into two classes: continuous waveforms (CW) and pulsed waveforms [7]. For CW both the transmitter and receiver are continuously operating which also explains why a majority of these systems have bistatic configuration (transmitter and receiver are separated). Despite this separation, signal leakage will occur and the receiver will have the leakage competing with potential return signals. For the pulsed waveform, on the other hand, the transmitter is operating for some short time duration τ. Between these short time durations, the collocated receiver (otherwise isolated and protected from transmitted power) will be connected to the antenna and register present signals. One cycle transmitting for time τ and the time receiving is called pulse repetition interval T_{PR}. The pulse repetition frequency f_{PR} can be determined using:

$$f_{PR} = \frac{1}{T_{PR}}. \tag{2.5}$$

A representation of transmitted pulses and echos with notation can be seen in Figure 2.1.

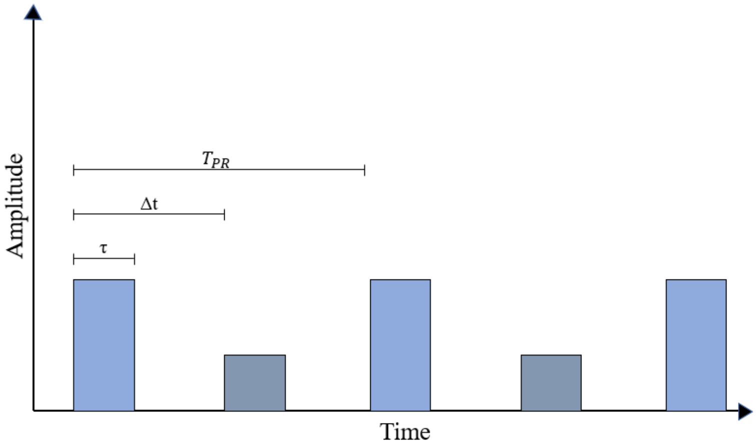

Figure 2.1: Emitted pulses and returns pulses with mentioned measures.

The received signal is sampled at discrete time intervals, with each sample representing a range bin (also called fast-time samples) corresponding to distance increments from the radar [3]. Coherent Processing Interval (CPI) is the total amount of time (both fast-time and slow-time samples) and in combination with the antenna elements the received data can be visualized in the radar datacube as in Figure 2.2.

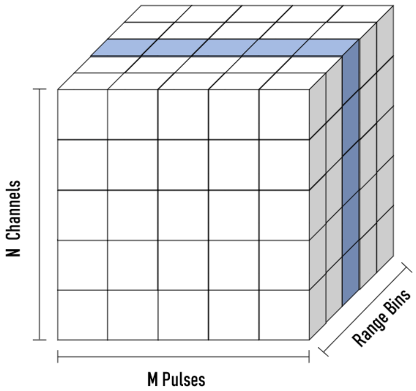

Figure 2.2: Radar datacube, STAP dimension marked in blue.

Space-time adaptive processing (STAP) combines the received signals for all the antenna elements and several pulses, meaning that one range bin, called cell under test (CUT), is evaluated at a time.

2.1.2 Ambiguities

Radar ambiguities occur when the system is unable to unambiguously determine the range or velocity to a target, imposing specific constraints on the system's f_{PR}.

2.1.2.1 Range

Range to a target can, as stated previously, be determined using propagation time for the pulse Δt [7]. This means that if there are two hypothetical targets present, $T1$ and $T2$, with $\Delta t_1 > T_{PR}$ respectively $\Delta t_2 < T_{PR}$, the echo that return for pulse M from target $T1$ will be received after transmitting pulse $M + 1$. This makes it hard to determine if the return is a close target from pulse $M+1$ or if it is a far-away target return to pulse M, see Figure 2.3.

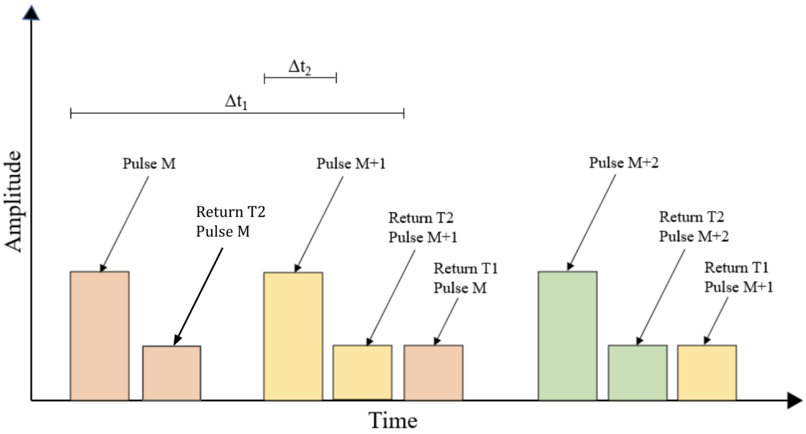

Figure 2.3: Emitted pulses M, M+1, M+2 and returns from targets T1 and T2.

The maximum unambiguous target range R_{max} can be derived from equation 2.1, stated as:

$$T_{PR} \geq \frac{2R_{max}}{c} <=> R_{max} = \frac{c * T_{PR}}{2} = \frac{c}{2 * f_{PR}}. \tag{2.6}$$

2.1.2.2 Doppler

Doppler effect describes how the wave frequency changes when the source is in motion in relation to the observer. This means that when the object has a velocity in the direction towards the observer the frequency will be higher than when the direction is away from the observer, this is visualized in Figure 2.4.

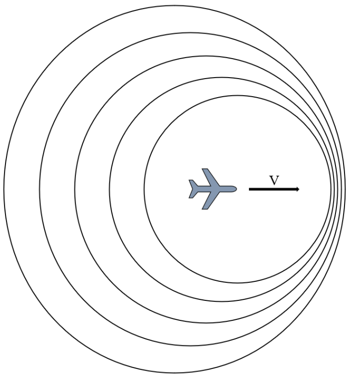

Figure 2.4: Doppler phenomena, higher frequencies in direction of velocity.

For a radar, this means that there will be a Doppler shift when the target has a relative velocity to the system [7]. The frequency Doppler shift is the difference between the frequency of the emitted signal and the frequency of the received signal echo. This is described as:

$$f_d \approx \frac{2v_t}{\lambda}, \tag{2.7}$$

where v_t is the radial component of the targets velocity towards the radar and λ is the wavelength of the signal. As recently presented, the lower f_{PR} increases the unambiguous range of the radar system. However, the Doppler effect creates an opposing ambiguity which has its roots in the Nyquist Samplings Theorem. The theorem describes that the maximum frequency that can be unambiguously measured is half the sampling rate, f_{PR}. This describes a relationship between the f_{PR} and the frequency Doppler shift, $f_{d_{max}}$, that can be measured unambiguously as

$$f_{d_{max}} = \pm \frac{f_{PR}}{2}, \tag{2.8}$$

which can be rewritten as

$$f_{PR_{min}} = 2f_{d_{max}} = \frac{4V_{r_{max}}}{\lambda}. \tag{2.9}$$

2.1.3 Target Detection

Target detection is determining the presence of a target signal in background disturbance from interfering sources such as clutter and thermal noise [3][9]. To perform detection the environmental interference must be approximated. This is achieved by estimating the covariance matrix $\mathbf{R}$. The possible detection of a target is often formulated as a binary hypothesis testing problem,

$$\begin{cases} H_0 : \mathbf{z} = \mathbf{n} + \mathbf{c} \\ H_1 : \mathbf{z} = \alpha\mathbf{v} + \mathbf{n} + \mathbf{c}, \end{cases} \tag{2.10}$$

where H_1 is the hypothesis of a target being present, while H_0 is the hypothesis for target being absent [3]. Here, $\mathbf{z}$ is the processed input vector from the radar, $\mathbf{n}$ is the noise term, $\mathbf{c}$ is the clutter term, $\mathbf{v}$ is the signal to detect, and α is the unknown amplitude of $\mathbf{v}$ [1]. Steering vector $\mathbf{v}$ for a target has a form described as

$$\mathbf{v}_\mathrm{s} = \begin{bmatrix} 1 & e^{j2\pi\frac{d}{\lambda}\sin\theta} & e^{j4\pi\frac{d}{\lambda}\sin\theta} & \dots & e^{j(N-1)2\pi\frac{d}{\lambda}\sin\theta} \end{bmatrix}^T \in \mathbb{C}^N \tag{2.11}$$

$$\mathbf{v}_\mathrm{t} = \begin{bmatrix} 1 & e^{j2\pi f_d T_{PR}} & e^{j4\pi f_d T_{PR}} & \dots & e^{j(M-1)2\pi f_d T_{PR}} \end{bmatrix}^T \in \mathbb{C}^M \tag{2.12}$$

$$\mathbf{v} = \mathbf{v}_s \otimes \mathbf{v}_t \in \mathbb{C}^{NM\times 1} \tag{2.13}$$

where d is inter-element spacing, M the number of pulses, N the number of antenna channels, λ is the wavelength, f_d is the Doppler shift, θ is the angle to the present target, and $\otimes$ the Kronecker product. The spatial and temporal vectors are further explained along with an clutter modeling example in Section 2.3.

Mismatched signal is a reflected signal received from a deviant angle than the nominal, or with a Doppler frequency deviating from the actual one of the target [10]. This can occur due to side-lobe interferer or imperfect modeling of the main lobe target. Reasons behind this can be either environmental or instrumental factors, for example, incomplete knowledge of the system such as calibration and range compression [3]. Because of the mismatched signals, the echo from the target can be described to be in the direction of the vector $\mathbf{p}$, rather than aligned with the nominal steering vector $\mathbf{v}$. Therefore the hypothesis testing problem can be rewritten to consider the mismatched signals

$$\begin{cases} H_0 : \mathbf{z} = \mathbf{n} + \mathbf{c} \\ H_1 : \mathbf{z} = \alpha\mathbf{p} + \mathbf{n} + \mathbf{c}. \end{cases} \tag{2.14}$$

The level of the mismatch can be measured as the angle between the nominal steering vector $\mathbf{v}$, and the actual one, referred to as $\mathbf{p}$, described as

$$cos^2\theta = \frac{\left|\mathbf{p}^H\mathbf{R}^{-1}\mathbf{v}\right|^2}{\mathbf{p}^H\mathbf{R}^{-1}\mathbf{p}\mathbf{v}^H\mathbf{R}^{-1}\mathbf{v}}. \tag{2.15}$$

This can be understood as if the target signal is equal to the steering vector, $cos^2\theta = 1$ meaning that the steering vectors are identical, and if $cos^2\theta = 0$ the steering vectors are orthogonal, maximal error between nominal and actual direction [3].

When solving these types hypothesis testing problem, a function for the decision statistics $t(\mathbf{z})$ is obtained, the detector, which gives a decision in line with the detection rule described as

$$t(\mathbf{z}) \underset{H_0}{\overset{H_1}{\gtrless}} \eta, \tag{2.16}$$

where the signal from the chosen detector $t(\mathbf{z})$ is compared with the threshold η [3]. If the received and processed signal exceeds the threshold, a target is detected [7].

The optimal test statistics $t(\mathbf{z})$ uses the Neyman-Pearson (NP) approach [3]. This approach states that the best detector is given by the ratio of the probability density function (PDF) of H_1, and the PDF of H_0, giving a so called likelihood ratio test, which can be expressed as

$$\frac{f(\mathbf{z}|H_1)}{f(\mathbf{z}|H_0)} \underset{H_0}{\overset{H_1}{\gtrless}} \eta, \tag{2.17}$$

where $f(\mathbf{z}|H)$ is the PDF under H_1 and H_0 respectively. Together with the energy detector (ED), the optimal NP test can be obtained, giving

$$\frac{||\mathbf{z}||^2}{\sigma^2} \underset{H_0}{\overset{H_1}{\gtrless}} \eta. \tag{2.18}$$

However, in reality, often more than one parameter in the binary hypothesis testing problem in equation 2.14 is unknown, making it inapplicable to use the NP approach. Instead, the test statistics $t(\mathbf{z})$ is often obtained by the generalized likelihood ratio test (GLRT), which replaces the unknown parameters with estimates, for example using secondary data to estimate the characteristics of the noise.

To evaluate the detector in question, both for matched and mismatched signals, there are two common metrics, the probability of detection P_D and the probability of false alarm P_{FA} [3]. Other methods to analyze the behaviors of the detector are by looking at the SINR, Receiver Operating Characteristics (ROC), Area Under the Curve (AUC), and obtained P_D for different levels of SNR.

Detectors have different properties, especially regarding selectivity and robustness to mismatched signals [1]. One of the most pioneering works is Kelly's detector, based on the GLRT. It is a detector where the detection statistic is independent of any unknown parameters for the H_0 hypothesis, leading to the constant false alarm rate, mentioned further below. Kelly's statistics can be written as

$$t_{Kelly} = \frac{\left|\mathbf{z}^H\mathbf{S}^{-1}\mathbf{v}\right|^2}{\mathbf{v}^H\mathbf{S}^{-1}\mathbf{v}(1+\mathbf{z}^H\mathbf{S}^{-1}\mathbf{z})} \tag{2.19}$$

where $\mathbf{S}^{-1}$ is is an estimate of the inverse of the scaled version of covariance matrix $\mathbf{R}$. This leads to Kelly's detector being a selective one, meaning that signals that do not come from the nominal direction are being rejected [3].

Another detector is the Adaptive Matched Filter (AMF) which can be expressed as

$$t_{AMF} = \frac{\left|\mathbf{z}^H \mathbf{S}^{-1} \mathbf{v}\right|^2}{\mathbf{v}^H \mathbf{S}^{-1} \mathbf{v}} \tag{2.20}$$

which is a robust detector [1]. There are a lot of other traditional detectors, and some of them will be presented in subsection 2.2.3 with curve equations and statistics in the CFAR-FP.

2.2 Constant False Alarm Rate

The threshold used in a detector is decided upon to give a constant probability of false alarm [3]. A false alarm is when some source, in the absence of targets, makes the signal exceed the threshold. Radar systems are constructed to maintain a specific false alarm rate, hence their name CFAR detectors. This property makes sure that the test statistics for the hypothesis of no targets, do not depend on any unknown parameters, such as unknown clutter or noise [2]. This leads to the P_{FA} being constant irrespective of changes in noise levels. This property is important in many applications since it makes the performance in different environments predictable and consistent [11].

2.2.1 CFAR-Processors

Data samples from the system are stored in the radar datacube and then range bins are iterated through cell by cell. Each cell will have its threshold determining the presence or absence of potential target [7][3]. To perform detection CFAR algorithms require information about the interfering environment and to solve this, K other independent identically distributed cells are used as secondary data. This information is collected from neighboring cells fulfilling the requirement regarding the identical variance. The secondary data used to estimate the interference statistic is gathered from a leading (direction of iteration) and lagging window and by averaging these output samples an adaptive threshold is obtained for a cell-averaging (CA-CFAR) processor.

2.2.2 CFAR Feature Plane

Radar data can be mapped to 2-D space and for this specific case it forms clusters of points [1]. The reason behind this approach is to analyze the behaviors of the decision boundaries of CFAR detectors when interpreted as linear or non-linear classifiers. These boundaries can then be evaluated based on the ability to separate the targets, denoted H_1, and the mismatched-H_1, from the non-targets H_0, for a robust detector, and the separation of H_1 from mismatched-H_1 and H_0 for selective detectors.

Mapping each range bin with the mapping chain

$$\{\mathbf{z}, \mathbf{Z} = [\mathbf{z}_1 \dots \mathbf{z}_k]\} \mapsto (\mathbf{z}, \mathbf{S}^{-1}) \mapsto (s_1, s_2) \mapsto (\beta, \tilde{t}) \tag{2.21}$$

makes the data appear in the CFAR-FP. Here, $(s_1, s_2) = (\mathbf{z}^H\mathbf{S}^{-1}\mathbf{z}, \frac{|\mathbf{z}^H\mathbf{S}^{-1}\mathbf{v}|^2}{\mathbf{v}^H\mathbf{S}^{-1}\mathbf{v}})$, which leads to the next step of the chain, representing $(\beta, \tilde{t})$ as

$$(\beta, \tilde{t}) = (\frac{1}{1+s_1-s_2}, \frac{s_2}{1+s_1-s_2}) \in (0,1) \times \mathbb{R}_+. \tag{2.22}$$

$\mathbf{S}$ is known, containing surrounding range bins calculated as $\mathbf{S} = \mathbf{Z}\mathbf{Z}^H$, and by dividing $\mathbf{S}$ with number of samples K an estimation of the covariance matrix $\hat{\mathbf{R}}$ is calculated as

$$\hat{\mathbf{R}} = \frac{1}{K}\mathbf{S}. \tag{2.23}$$

This is presented further in Section 2.4.

As mentioned above, by redefining a detector through this chain it will follow the CFAR property, and be represented as a linear or non-linear classifier in the new $\beta - \tilde{t}$ CFAR-FP. The mapping chain can also be presented in a multi-layer scheme, as can be seen in the Figure 2.5.

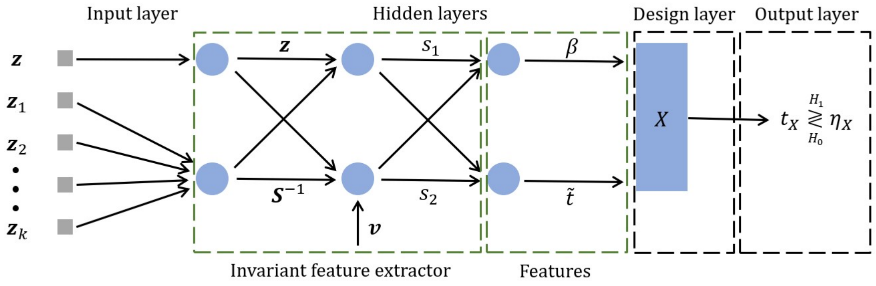

Figure 2.5: Layered representation of the mapping chain.

The mapping chain utilizes maximal invariant statistics, in this specific case using the maximal invariant between Kelly's and AMF's statistics. As visualized in Figure 2.5, the first two layers can be seen as an invariant feature extractor, compressing the data in two steps. The first step ensures secondary data is only used to construct the sample covariance matrix $\mathbf{S}$, guaranteeing the CFAR property. The next step is a reparameterization of the data to get to the two scalars s_1 and s_2, where s_1 can be seen as the energy detector, and s_2 as a correlator. The mapping to β and $\tilde{t}$ is performed to get to two independent variables, that also have well-known distributions. For example, $\tilde{t}$ is Kelly's detector, which is considered to be a standard for matched conditions. This last step of the mapping chain is also a way of getting a more suitable mathematical representation of the problem, than if s_1 and s_2 where to be used.

The covariance matrix for this hypothesis testing problem is an unknown high dimensional parameter that is relevant for the decision-making [12][13]. By transforming the data, each point value is changed while maintaining the distribution, ensuring that the significant parameters are kept in an acceptable region. This transformation divides the data points into different classes that are dependent on sample space, the maximal invariant. This type of test statistic decreases the dimensionality of the problem.

2.2.3 Known Detectors

Traditional model based detectors, such as the ones presented in Subsection 2.1.3, can also be represented in the CFAR-FP. The statistics of the detectors can be rewritten as $t_X(\beta, \tilde{t}) = \eta_X$, only depending on β and $\tilde{t}$, and compared to the threshold η_X for the desired P_{FA}. This makes it possible to express the detector as a function $\tilde{t}$ of β, creating a linear, or non-linear representation of the detector in the CFAR-FP.

Some of the traditional model based detectors are Kelly's detector, AMF, Adaptive coherence detector (ACE), and Adaptive beamformer orthogonal rejection test (ABORT). All of these can be expressed as a function of β and $\tilde{t}$, but their statistics can also be rewritten in terms of these two variables. In Table 2.1 both the decision region boundary and the statistics of the detector can be seen.

Name	Decision Region Boundary Equation	Statistics
Kelly's detector	$\tilde{t} = \eta_K$	$t_{Kelly} = \frac{\tilde{t}}{1+\tilde{t}}$
AMF	$\tilde{t} = \eta_{AMF}\beta$	$t_{AMF} = \frac{\tilde{t}}{\beta}$
ACE	$\tilde{t} = -\frac{\eta_{ACE}}{1-\eta ACE}\beta + \frac{\eta_{ACE}}{1-\eta_{ACE}}$	$t_{ACE} = \frac{\tilde{t}}{\tilde{t}+1-\beta}$
ABORT	$\tilde{t} = -\beta + \frac{\eta_A}{1-\eta_A}$	$t_A = \frac{\tilde{t}+\beta}{\tilde{t}+1-\beta}$

Table 2.1: Decision boundary and statistics of some traditional detectors.

2.2.4 Cluster Characteristics

When mapping data to the CFAR-FP, there are some statistical characteristics of the clusters [1]. First, the center point of the clusters can be expressed as $(\mu_\beta, \mu_{\tilde{t}})$ given

$$\begin{aligned} \mu_\beta &= 1 - \frac{NM-1}{K+1} e^{-\gamma(1-\cos^2\theta)} \\ &\quad \times {}_2F_2(K+1, NM; NM-1, K+2; \gamma(1-\cos^2\theta)) \\ \mu_{\tilde{t}} &= \frac{1+\gamma\mu_\beta\cos^2\theta}{K-NM} \end{aligned} \tag{2.24}$$

where ${}_2F_2$ is the generalized hypergeometric function, NM is the dimension of the CUT, K number of samples used as secondary data, $\cos^2\theta$ the level of mismatch and γ is the SNR in dB defined as

$$\gamma = |\alpha|^2 \mathbf{p}^H \mathbf{C}^{-1} \mathbf{p} \in \mathbb{R}_+. \tag{2.25}$$

This means that when calculating the center of the H_0 cluster, γ can be set to 0, resulting in

$$(\mu_\beta, \mu_{\tilde{t}}) = \left(\frac{K - NM + 2}{K + 1}, \frac{1}{K - NM} \right). \tag{2.26}$$

Also the rotation of the cluster of points $\xi = \begin{bmatrix} \beta \, \tilde{t} \end{bmatrix}^T$ can be described, using a covariance matrix expressed as

$$\mathrm{COV}[\xi] = \begin{bmatrix} \sigma_\beta^2 & \rho \sigma_\beta \sigma_{\tilde{t}} \\ \rho \sigma_\beta \sigma_{\tilde{t}} & \sigma_{\tilde{t}}^2 \end{bmatrix} \tag{2.27}$$

with

$$\begin{aligned} \sigma_\beta^2 = & \frac{NM(NM-1)}{(K+2)(K+1)} e^{-\gamma(1-\cos^2\theta)} \\ & \times {}_2F_2(K+1, NM+1; NM-1, K+3; \gamma(1-\cos^2\theta) \\ & - (1-\mu_\beta)^2 \end{aligned} \tag{2.28}$$

$$\begin{aligned} \sigma_{\tilde{t}}^2 = & \frac{(\gamma \cos^2\theta)^2(\sigma_\beta^2 + \mu_\beta^2) + (1 + 2\gamma\mu_\beta^2 \cos^2\theta)(K - NM + 1)}{(K-NM)^2(K-NM-1)} \\ & + \frac{(\gamma\cos^2\theta)^2\sigma_\beta^2}{(K-NM)^2} \end{aligned} \tag{2.29}$$

$$\rho = \frac{1}{\sigma_\beta \sigma_{\tilde{t}}} \left[\frac{\mu_\beta}{K - NM} + \frac{\gamma(\sigma_\beta^2 + \mu_\beta^2)\cos^2\theta}{K - NM} - \mu_\beta \mu_{\tilde{t}} \right]. \tag{2.30}$$

As for the center of the H_0, since $\gamma = 0$ and $\rho = 0$ for H_0, leading to no rotation of the clutter cluster.

By using the centers of the clusters for perfect matched targets, and totally mismatched ones, a line can be derived describing the movement of the centers of the clusters in relations to each other. The approximation of the line can be seen as a

$$\tilde{t} = m\beta + q, \tag{2.31}$$

where m is the slope of the line, derived from the difference between the centers of the perfect matched cluster and the totally mismatched one. Therefore, m can be expressed as

$$m = \gamma \left(\frac{K - NM - 2}{(K - NM)\left[(K+1)g(\gamma) + 1 - NM\right]} \right), \tag{2.32}$$

making the slope depend on the size of the steering vector and the SNR. Here, $g(\gamma)$ is

$$g(\gamma) = \frac{N-1}{K+1} e^{-\gamma} {}_2F_2(K+1, N; N-1, K+2; \gamma). \tag{2.33}$$

From the expression of m, q can be derived as

$$q = m(g(\gamma) + 1) + \frac{1}{K - NM}. \tag{2.34}$$

As can be understood from the expression of the approximated line, when the size of the CUT increases, the slope approaches zero, making the target clusters approach the H_0 cluster.

2.3 Space-Time Adaptive Processing

Ground clutter is often present with high energy and creates a need for separation from the target signal [8]. As presented earlier, objects with a velocity separated from zero will have a Doppler shift for received reflections. For stationary systems, the received signal can be zero-Doppler filtered which separates non-moving targets from moving ones, removing ground clutter, and leaves the signal of a hypothetical target. This 1-D technique is not sufficient when clutter is Doppler-shifted for moving radar platforms demanding joint space-time processing.

For an airborne radar platform assuming no curved earth effects, ground clutter can be defined within a specified radius and each point scatter will be Doppler shifted [8]. For a radius sufficiently large, elevation angles can be neglected allowing for a 2-D assumption. For a uniform linear array (ULA), the normalized Doppler shift for one point scatter can be described as $f_d = \frac{2v}{\lambda} \sin\theta$ with angle of arrival θ, velocity of platform v and wavelength λ, see Figure 2.6.

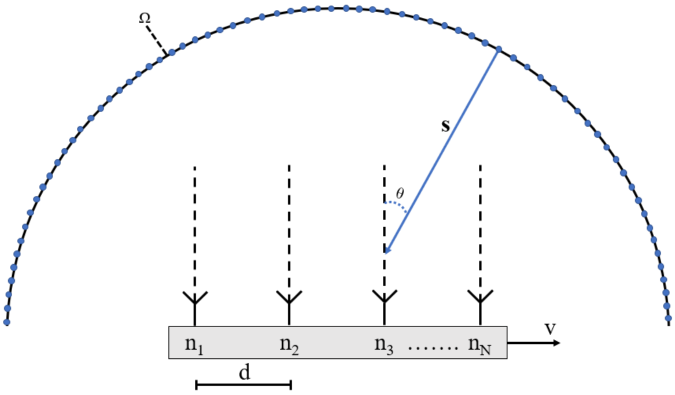

Figure 2.6: Schematic overview of ULA receiving signal from clutter patches in the circle Ω.

The temporal steering vector for all pulses from one clutter patch can be stated as

$$\mathbf{s}_t = \begin{bmatrix}1 & e^{j2\pi f_d T_{PR}} & e^{j4\pi f_d T_{PR}} & \dots & e^{j(M-1)2\pi f_d T_{PR}}\end{bmatrix}^T \in \mathbb{C}^M, \tag{2.35}$$

where M is the number of pulses processed in the CPI. Spatial steering vector is describes as

$$\mathbf{s}_s = \begin{bmatrix}1 & e^{j2\pi\frac{d}{\lambda}\sin\theta} & e^{j4\pi\frac{d}{\lambda}\sin\theta} & \dots & e^{j(N-1)2\pi\frac{d}{\lambda}\sin\theta}\end{bmatrix}^T \in \mathbb{C}^N, \tag{2.36}$$

where N is the number of antennas in the radar array. The NM space-time steering vector is represented by the Kronecker product

$$\mathbf{s}_{st} = \mathbf{s}_s \otimes \mathbf{s}_t \in \mathbb{C}^{NM \times 1}. \tag{2.37}$$

For a monostatic radar ground clutter forms a circle for which the energy received in one antenna is given by

$$\sigma_c^2 = \frac{\lambda^2 P_t}{(4\pi)^3} \sigma_0 \int_\Omega \frac{G_t G_r}{R^4} dA_\Omega \tag{2.38}$$

where Ω corresponds to the circle on the ground for range R, σ_0 is the clutter reflectivity and P_t, G_t, G_r denotes, as previously, transmitted power, transmitted gain and received gain respectively [14]. Since earth is assumed homogeneous in this work σ_0 will be constant. The return energy combined with the steering vectors gives a clutter covariance model (assuming continuous voltage returns for all range bins) described as

$$\mathbf{X}_c = \frac{\lambda^2 P_t}{(4\pi)^3} \sigma_0 \int_\Omega \frac{G_t G_r}{R^4} \cdot \mathbf{s}_{st} \mathbf{s}_{st}^H dA_\Omega, \tag{2.39}$$

where $\mathbf{X}_c$ is the ground clutter covariance matrix, This model can be approximated by summing contributions from clutter patches, for some constant range R, which gives the total space-time clutter-only covariance matrix as

$$\mathbf{R_c} = \frac{1}{N_s} \sum_{n=1}^{N_s} \mathbf{s}_{st,n} \mathbf{s}_{st,n}^H \in \mathbb{C}^{NM \times NM} \tag{2.40}$$

where N_s is the number of synthetic clutter patches. In reality there is a unique factor for every clutter patch depending on the transmitted gain pattern G_t. However, by only studying the received signal this factor can be neglected.

2.4 Sample Covariance Estimation

As mentioned previously, the covariance matrix $\mathbf{R}$ is not known, but can be estimated using secondary data [3]. The secondary data brings information about the noise and clutter. For cases containing colored noise,the amount of samples K needs to be equal to or larger than the size of the CUT, $K \geq NM$, to ensure a non-singular estimation [8]. Using surrounding range bins with assumed equal distribution, the covariance for the CUT can be estimated as

$$\hat{\mathbf{R}} = \frac{1}{K} \sum_{k=1}^{K} \mathbf{z}_k \mathbf{z}_k^H. \tag{2.41}$$

This approximation holds under the criteria of being uncorrelated with shared covariance and can be proven an unbiased estimation since

$$E\left[\hat{\mathbf{R}}\right] = E\left[\frac{1}{K} \sum_{k=1}^{K} \mathbf{z}_k \mathbf{z}_k^H\right] = \frac{1}{K} \sum_{k=1}^{K} E\left[\mathbf{z}_k \mathbf{z}_k^H\right] = \frac{1}{K} \sum_{k=1}^{K} \mathbf{R} = \mathbf{R}. \tag{2.42}$$

If the secondary data follows a Gaussian distribution, equation 2.41 represents the maximum likelihood estimate of $\mathbf{R}$. Reed, Mallet, and Brennan derived a formula, referred to as the RMB loss, to calculate the signal power loss ratio SINR in relation to the amount of secondary data used to estimate the sample covariance matrix formulated as [15]

$$loss = -10\log_{10}\left(\frac{K+2-NM}{K+1}\right). \tag{2.43}$$

This laid the foundation for a rule of thumb as this proofs that using at least $2NM$ of secondary data will result in an average loss ratio below 3 dB from the optimum. This can be rephrased a bit simplified as independent of noise and clutter, using twice the number of samples to estimate $\mathbf{R}$ is close to convergence of optimum regarding number of samples. However, using smaller amounts will result in decreasing performance and as K often is limited in many practical scenarios there are several proposed techniques improving convergence and solutions for when $K < NM$.

For a uniform array with constant f_{PR}, the space-time clutter only covariance is low rank due to oversampling in radar systems with STAP processing [16][17]. Regarding the estimation $\hat{\mathbf{R}}$, only eigenvalues greater than receiver noise floor contributes significantly to clutter approximation and the ones below this level can be ignored [8]. By focusing on these dominant eigenvalues, valuable insights into the radar systems performance can be obtain, particularly in terms of the matrix rank. The rank can be approximated

$$\text{rank}(\hat{\mathbf{R}}) \approx N + (M-1)\beta_r, \tag{2.44}$$

where β_r is a constant for the system calculated as

$$\beta_r = \frac{2v_pT}{d}, \tag{2.45}$$

where v_p is the speed of the platform, T is the T_{PR} and d the inter-element spacing [18]. However, vast amounts of secondary data is required to approximate the noise floor in the covariance estimation, $2NM$ samples does not yield a good approximation. The receiver noise floor for calibrated radars is known and by utilizing this information the estimated covariance can be regularized to enhance performance.

2.4.1 Diagonal Loading

As already mentioned, using less than NM samples results in singular and thus non-invertible $\hat{\mathbf{R}}$. To solve this we can introduce a loading term such that

$$\hat{\mathbf{R}}_{\text{DL}} = \hat{\mathbf{R}} + \mathbf{I}L, \tag{2.46}$$

where $\mathbf{I}$ is the identity matrix and L is a small loading factor [5]. This results in less eigenvalue spread which reduces the effect of randomly shaped noise eigenbeams while also maintaining the same eigenvectors. Eigenvalues for the true covariance matrix $\mathbf{C}$, clutter only covariance matrix $\hat{\mathbf{R}}$ and the scaled estimation $\mathbf{S}$ as original estimate and with diagonal loading (DL) is visualized in Figure 2.7, to show which effect the diagonal loading has on the scaled estimation **S**.

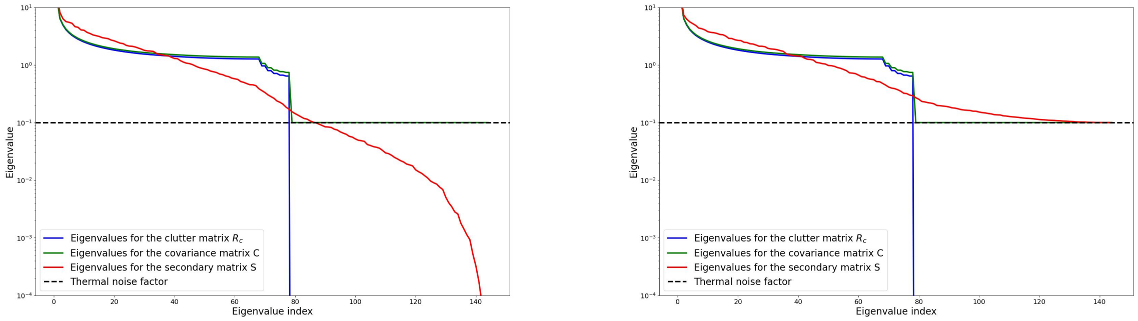

(a) Original estimate **S**.

(b) Diagonally loaded **S**.

Figure 2.7: Eigenvalues for covariance matrices for radar configuration of N = 12 and M = 12.

2.4.2 Fast Maximum Likelihood Estimation

The FML (fast maximum likelihood) estimate is found as [6]

$$\mathbf{R}_{\text{FML}} = \arg\min_{R_0} \left[\ln|\mathbf{R}| + \text{Tr}(\mathbf{R}^{-1}\hat{\mathbf{R}})\right]. \tag{2.47}$$

This can also be found by using the eigendecomposition of the estimated covariance matrix $\hat{\mathbf{R}}$.

$$\hat{\mathbf{R}} = \Phi \, \Lambda \, \Phi^H \tag{2.48}$$

where Λ is the diagonal matrix with the eigenvalues $\lambda_1 \geq \lambda_2 \geq \ldots \geq \lambda_{NM}$ of $\hat{\mathbf{R}}$, and Φ is unitary matrix (orthonormal eigenvectors of $\hat{\mathbf{R}}$). $\hat{M}$ is an approximation of the number of significant eigenvalues in $\mathbf{R}$ and corresponds to the number of eigenvalues greater than noise level σ for $\hat{\mathbf{R}}$. By assigning the lower (below thermal noise floor) eigenvalues to σ referred to as Λ_0, the approximation of $\hat{\mathbf{R}}_{FML}$ can be expressed as

$$\hat{\mathbf{R}}_{\text{FML}} = \Phi \, \Lambda_0 \, \Phi^H. \tag{2.49}$$

See the same example as previously implemented with FML in Figure 2.8.

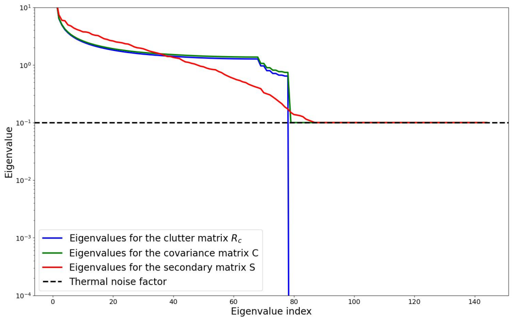

Figure 2.8: Eigenvalues for covariance matrices for radar configuration of N = 12 and M = 12. **S** estimated with using FML.

2.5 Machine Learning

Machine Learning (ML) is a subbranch of Artificial Intelligence (AI) and is built upon the principle of a computer learning to make predictions from a dataset, rather than being exactly programmed what to do [19]. This makes machine learning a powerful tool in many applications, such as pattern recognition and natural language processing. The field of machine learning in turn can be divided into three types of models: supervised learning, unsupervised learning, and reinforcement learning. For the task of radar detection, supervised learning is of greatest interest.

Supervised learning uses data with already labeled output to create a function to describe the relations between the input and the output [19]. The data is divided into at least two subsets, one for training and one for testing. The training set is used to model the function by adjusting its weights based on the output labels. Models of this kind are for example Artificial Neural Networks, different types of regressions, k-nearest neighbors (kNN), and support vector machines (SVM).

2.5.1 Artificial Neural Networks

Artificial Neural Networks (ANN) are inspired by how the animal brain works [20]. ANN is built upon different neuron layers, such as input, hidden, and output layers, which are connected through weights that are being updated throughout the training process, see Figure 2.9. These weights can be updated in different ways, which also is the way to classify these types of networks. Some of the different types are feed-forward networks that model static systems, for example, multilayer perceptrons (MLP), recurrent networks that use feedback to model dynamical systems and convolutional networks that are often used in image analysis.

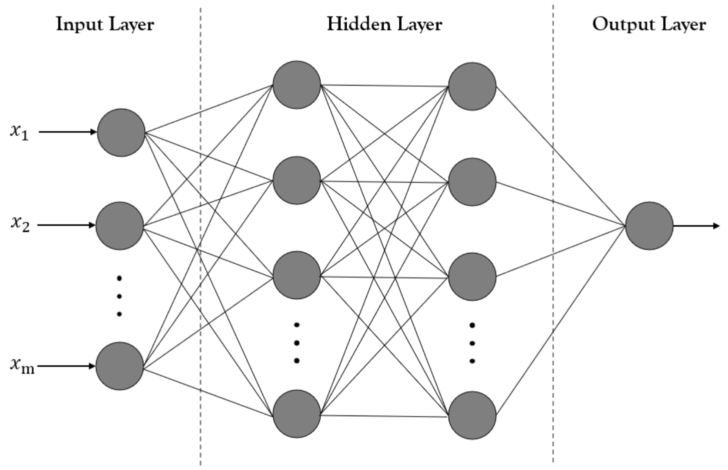

Figure 2.9: Structure of an ANN with two hidden layers.

2.5.2 K-nearest neighbors

K-nearest neighbors is an algorithm that uses known features of the data points in a feature plane to classify an unknown test point based on its neighbors [20]. This classification method is non-parametric and considered a baseline in many classification tasks [21]. This type of algorithm is referred to as a lazy learning algorithm, since no previous offline training is needed, and the classification is done directly based on the training data. The algorithm is based on the Euclidean distance between the unknown data point and its k nearest neighbors, where k is an integer to be chosen [22]. The normalized Euclidean distance between two points, with m input features, can be expressed as

$$dist(A,B) = \sqrt{\frac{\sum_{i=1}^{m}(x_i - y_i)^2}{m}} \tag{2.50}$$

where x_i and y_i are the two points where the distance should be calculated between [21].

2.5.3 Symbolic Classification

Symbolic classification is a type of supervised learning, built upon symbolic regression (SR) [23]. The aim of SR is to describe the relationship between data as a mathematical expression. The expression can contain multiple variables, operators, and coefficients, and the goal is to find the best combination for the specific task. Traditionally, the algorithms used for solving these types of tasks are derived from genetic programming (GP), using binary trees to aim to find the optimal solution. GP works by creating a population of programs that are to be evolved over generations, and use the principle "Survival of the fittest" from Darwin [24].

To be able to use SR as a binary classifier, binary cross entropy (BCE) is used for evaluation, in order to minimize the fitness function [25]. Furthermore, a sigmoid function is used to make the output of the expression a number between 0 and 1 as prediction for absence or presence respectively.

2.5.4 Support Vector Machine

Support vector machine is often used as a tool in classification tasks [26]. It works by creating a hyperplane that separates the data points, while also maximizing the distance between the support vectors and the hyperplane itself, which can be seen in Figure 2.10.

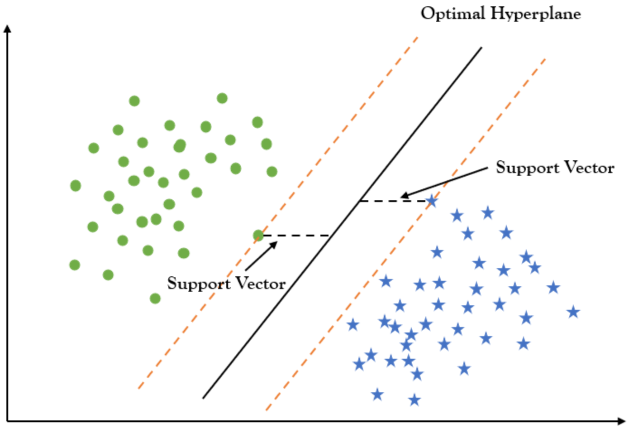

Figure 2.10: Visual description of how SVM works.

SVM can either be done linearly or non-linearly on separable problems, but it can also be a great tool for non-separable problems [26]. The one shown in Figure 2.10 is a linearly separable problem. As mentioned above, the goal is to create the optimal hyperplane for the specified task, and this is done in different ways depending one which of the three problems that are of interest. For linearly separable problems, the optimal hyperplane is stated as

$$w^T x + b = 0, \tag{2.51}$$

where w are the weights and b the threshold, also referred to as the bias term. The relation between a point x and the hyperplane can therefore be described as

$$f(x) = w^T x + b, \tag{2.52}$$

and the distance to the support vectors to be maximized are expressed as

$$r = |\frac{f(x)}{||w||}|. \tag{2.53}$$

In real life, there are more non-linearity, and the data must be mapped to a lower dimension feature space. For this mapping, a kernel function K needs to be used [26]. These function can, for example, either be polynomial, a Gaussian Radial Basis Function, or a Multi-Layer Perceptron, and uses parameters such as γ_{SVM} for defining the influence of a single training point [27].

For the case of non separable data, there are no hyperplane to accurately separate the the different classes from each other [26]. Therefore a variable ξ_i for the misclassifications error, and a coefficient C, for punishing the the outliers, are introduced to lower the effect of the noise.

3

Methods

This work will be divided into three major tasks, based on the research questions presented in section 1.2, which also will divide this section. The method will present how data was generated using different covariance matrices and which parameter values used. Then cluster behavior will be analyzed and characterized to finally implement both traditional model-based detectors as new machine learning implementations.

As the objective of this study was to evaluate the performance and robustness of data-driven machine learning models compared to traditional ones, an adjustable data simulator was needed. As the spatial dimension was added, this created a need for STAP-processing to separate clutter from targets. This allowed for a comparison regarding cluster characteristics between temporal only covariance and STAP-covariance to draw conclusions about CFAR-FP feasibility for different radar scenarios.

3.1 Data Generation

For radar scenarios with only temporal dimension, the covariance matrix used in article [1] was used where the clutter covariance matrix was calculated using

$$\mathbf{R}_c = e^{-2\pi^2\sigma_f^2(m_1-m_2)^2} \in \mathbb{C}^{NM\times NM} \tag{3.1}$$

where m_1 and m_2 represent the index corresponding to row and column respectively. σ_f is the one-lag correlation coefficient, set to $\sigma_f \approx 0.051$.

To model colored Gaussian interference with an additional spatial dimension, 500 synthetic clutter patches were evenly distributed in angles of $\pm\frac{\pi}{2}$ relative to the normal direction perpendicular to the moving radar platform. The moving platform was modeled with a speed of 150 m/s which induced a Doppler shift for the stationary ground clutter patches. The individual steering vectors for all clutter patches were derived by calculating the Kronecker product in equation 2.37. The total space-time clutter-only covariance matrix was determined by summing over all individual steering vectors for each synthetic clutter patch and the total clutter interference was therefore calculated as

$$\mathbf{R_c} = \frac{1}{500}\sum_{n=1}^{500} \mathbf{s}_{st,n}\mathbf{s}_{st,n}^H \in \mathbb{C}^{NM\times NM}. \tag{3.2}$$

By adding thermal noise set to be 10 dB weaker than the diagonal elements ($\sigma^2 = 0.1$) the total covariance matrices was calculated as

$$\mathbf{C} = \mathbf{R}_c + \sigma^2 \mathbf{I} \tag{3.3}$$

where $\mathbf{I}$ is an identity matrix. The generated targets had a steering vector formulated as

$$\mathbf{v} = \begin{bmatrix} 1 & e^{j2\pi f_d T_{PR}} & e^{j4\pi f_d T_{PR}} & \dots & e^{j(M-1)2\pi f_d T_{PR}} \end{bmatrix}^T \in \mathbb{C}^M \tag{3.4}$$

were $f_d T_{PR} = 0.08$. α is the target amplitude for a given steering vector and SNR, obtained by solving 2.25. The mapping was performed using the mapping chain from equation 2.21 and 2.22. For mismatched targets, another steering vector $\mathbf{p}$ was used defined as $\mathbf{v}$ but with $f_d = 0.08 + \frac{q}{M}$, where q is a float used to obtain different levels of mismatches. Steering vector p becomes

$$\mathbf{p} = \begin{bmatrix} 1 & e^{j2\pi(0.08+\frac{q}{M})} & e^{j4\pi(0.08+\frac{q}{M})} & \dots & e^{j(M-1)2\pi(0.08+\frac{q}{M})} \end{bmatrix}^T \in \mathbb{C}^M \tag{3.5}$$

Targets with space-time steering vectors was modeled as

$$\mathbf{v}_\mathrm{s} = \begin{bmatrix} 1 & e^{j2\pi\frac{d}{\lambda}\sin\theta} & e^{j4\pi\frac{d}{\lambda}\sin\theta} & \dots & e^{j(N-1)2\pi\frac{d}{\lambda}\sin\theta} \end{bmatrix}^T \in \mathbb{C}^N \tag{3.6}$$

$$\mathbf{v}_\mathrm{t} = \begin{bmatrix} 1 & e^{j2\pi f_d T_{PR}} & e^{j4\pi f_d T_{PR}} & \dots & e^{j(M-1)2\pi f_d T_{PR}} \end{bmatrix}^T \in \mathbb{C}^M \tag{3.7}$$

$$\mathbf{v} = \mathbf{v}_s \otimes \mathbf{v}_t \in \mathbb{C}^{NM\times 1} \tag{3.8}$$

with $\lambda = 0.1$ m, $T_{PR} = 10^{-3}$, $d = \frac{\lambda}{2}$ m, target speed $v = 100$ m/s and spatial angle to target $\theta = \frac{\pi}{4}$. These parameters cause the target to compete with the ground clutter. Various values were tested, but they did not significantly affect the clusters, as long as the Doppler frequency deviated from clutter patch Doppler frequency for that spatial angle. Mismatched targets was generated as $\mathbf{v}$ but with an additional terms $\frac{k}{N-1}$ and $\frac{k}{M-1}$, were k is a float used to obtain some level of mismatch, which gives

$$\mathbf{p}_\mathrm{s} = \begin{bmatrix} 1 & e^{j2\pi(\frac{d}{\lambda}\sin\theta+\frac{k}{N-1})} & e^{j4\pi(\frac{d}{\lambda}\sin\theta+\frac{k}{N-1})} & \dots & e^{j(N-1)2\pi(\frac{d}{\lambda}\sin\theta+\frac{k}{N-1})} \end{bmatrix}^T \in \mathbb{C}^N \tag{3.9}$$

$$\mathbf{p}_\mathrm{t} = \begin{bmatrix} 1 & e^{j2\pi(f_d T_{PR}+\frac{k}{M-1})} & e^{j4\pi(f_d T_{PR}+\frac{k}{M-1})} & \dots & e^{j(M-1)2\pi(f_d T_{PR}+\frac{k}{M-1})} \end{bmatrix}^T \in \mathbb{C}^M \tag{3.10}$$

$$\mathbf{p} = \mathbf{p}_s \otimes \mathbf{p}_t \in \mathbb{C}^{NM\times 1} \tag{3.11}$$

3.1.1 Radar Configurations

Two antenna and pulse configurations were established to analyze and compare the usability of CFAR-FP and implement new detectors

- **Case 1:** N = 1 antenna and M = 20 pulses
- **Case 2:** N = 20 antennas and M = 20 pulses.

For both configurations, data were mapped to CFAR-FP using different estimates of the covariance matrix. The amount of samples used as secondary data varied, with K equal to 0.5, 1, and 2 times the length of the vectorized CUT. Additionally, diagonal loading was implemented and evaluated, as well as FML for cases where the eigenvalues are below noise level. All generated data had SNR between 10 and 20 dB, with a step size of 2, and the level of mismatch was $\cos^2\theta = 0.65, 0.83, 1$ (1 corresponds to perfect match). By using the covariance matrices, samples from H_0 and H_1 were Monte Carlo simulated from these distributions

$$H_0 : \mathbf{z}_k \sim \mathcal{CN}(0, \mathbf{R}) \tag{3.12}$$

$$H_1 : \mathbf{z}_k \sim \mathcal{CN}(\alpha\boldsymbol{v}, \mathbf{R}) \tag{3.13}$$

with mean 0 and $\alpha\mathbf{v}$ (or $\alpha\mathbf{p}$) respectively. Each simulated sample represents a CUT from one of the hypotheses. A full overview of all simulated cases can be seen in Table 3.1.

Estimation of **S**	Case 1 (1x20)	Case 2 (20x20)
K = NM	x	x
K = 2NM	x	x
K = 0.5NM with DL	x	x
K = NM with DL	x	x
K = 2NM with DL	x	x
K = 0.5NM with FML	x	x
K = NM with FML	x	x
K = 2NM with FML	x	x

Table 3.1: All simulated cases.

3.2 Cluster Characteristics

To be able to draw conclusions about the cluster characteristics in CFAR-FP, several parameters were evaluated. These included SNR, level of mismatch, and the amount of secondary data K (in combination with FML estimation and diagonal loading). The amount of secondary data was varied in size, with K equal to 1, 2, and additionally to the simulation, also 5 times the size of the CUT, instead of 0.5. The SNRs evaluated was 10, 15, and 20, and the levels of mismatch used were in decreasing order $\cos^2\theta = 0.2, 0.65, 0.83, 1$. For all cases mentioned, 5,000 CUTs belonging to H_0, and 5,000 CUTs of H_1 for each level of mismatch were plotted. The same was also done by varying the SNR, changing γ between 10, 15, and 20 dB. This was also plotted for the same mismatches as before but only analyzed for $K = 2NM$.

3.3 Detection Models

Traditional detectors were evaluated. The ones chosen were Kelly, AMF, ACE, and ABORT, and for all of those, a threshold for $P_{FA} = 10^{-4}$ was set. Since the threshold depends on clutter only, 10^6 H_0 CUTs were generated. The threshold for each detector was determined by adjusting it until a ratio of H_0 points misclassified as targets reached 10^{-4}.

To evaluate the performance of the detectors, ROC-curves were made for SNR = 15 dB, and a range of P_{FA} from 10^{-4} to 10^0, using a logarithmic scale. 1,000 samples for H_1 in both perfect match and mismatched conditions were used to calculate P_D for every P_{FA}.

3.3.1 Machine Learning Implementations

For the machine learning part, multiple algorithms were implemented, trained, and then evaluated. The dataset used for training, validation, and testing has a size of 40,000 samples, where 20,000 are clutter points, 10,000 targets, resulting in 2,000 for each SNR between 14-20 dB, and 1,000 for each mismatched target level for each SNR. This data was then split into test, validation, and training, with 20% of the data to test, and 30% of the remaining data for validation. This results in a training set of 22,400 samples, 11,200 of label 1, representing a target of some kind, and 11,200 of label 0, indicating clutter. The models that were implemented were a MLP, a symbolic classifier, henceforth referred to as SR, a kNN classifier, and a SVM classifier.

3.3.2 Cases for ML

As for the training, all data generated was not used for training. This depends on the formation of the clusters, since excessive overlap of the clusters generate no meaningful results. Therefore the case of NM samples as secondary data will not be used in the machine learning implementations. As mentioned in the section about *Radar Configurations*, two different cases will be generated, one antenna channel and 20 pulses, and 20 antenna channels and 20 pulses. These two cases will also be the cases when trained on the ML algorithms. A full overview of all cases can be seen in Table 3.2.

Estimation of **S**	Case 1 (1x20)	Case 2 (20x20)
K = NM	–	–
K = 2NM	x	x
K = 0.5NM with DL	x	x
K = NM with DL	x	x
K = 2NM with DL	x	x
K = 0.5NM with FML	x	x
K = NM with FML	x	x
K = 2NM with FML	x	x

Table 3.2: Cases used for training and evaluation of ML algorithms.

3.3.3 Implementations

A MLP with one hidden layer, using 50 neurons, were implemented using pytorch [28]. Between each layer, a ReLU activation function were used, and for the output a sigmoid function to get the output between 0 and 1. As an optimizer, Adam was used with a learning rate of 0.005, and the loss function used was binary cross entropy, since this is a binary classification problem between targets and clutter. The training was done for 10 epochs, in batches of size 64. Furthermore, the model was evaluated on both validation and test data.

The SR was implemented using GPlearn Genetics, which is an extension of the scikit-learn library [29]. After doing gridsearch, it was decided to use a population size of 500, and train for 40 generations. As for the MLP, binary cross entropy was used, as well as a sigmoid for the output. In contrary to the MLP, no validation was done, only testing.

To be able to decide which P_{FA} the model should have, a threshold needed to be set for both methods. Since a sigmoid function was used for the output in both models, it was possible to look at the output probability to be able to set a threshold. The threshold was set to the output probability that gave the ratio of clutter misclassified as targets equal to the requested P_{FA}.

The implementation of the kNN classifier was done with KNeighborsClassifier from scikit-learn, together with an algorithm for faster calculations for low dimension data, called *KD tree*, with a leaf size of 9000 [30]. The way of getting to the specified P_{FA} was not done in a similar way to the two previous presented algorithms. Instead of setting a threshold for the decision boundary for a specific P_{FA}, the number of neighbors k, were increased to achieve the desired P_{FA}. The number of neighbors tested was 1, 2, 50, 100, 500, 1000, 5000, 7500 and 9000, leading to longer runtime for the algorithm to make predictions when larger values of k are used.

SVM was implemented in a similar way as kNN in terms of P_{FA}, with a variation of the variable γ_{SVM}, that decides the influence of each training sample, to get to a certain level P_{FA}. The SVM used was SVC from scikit-learn, which uses a Polynomial as a kernel, together with a punishment coefficient $C = 100$ [31]. For γ_{SVM}, six different values was used to try to achieve the desire threshold of 10^{-4}. These were 0.06, 0.07, 0.09, 0.5, 1 and 10.

3.3.4 Evaluation

Evaluation of the first two models in the CFAR-FP was done in three ways, by visualization, ROC-curves, and SNR-P_d -plots. Visualization of decision region boundary was done in the CFAR-FP for all detectors, both model based and data driven, to be able to see how they differed visually. Moreover, ROC-curves were made for P_{FA} from 10^{-4} to 10^{0}, using a logarithmic scale, and evaluated on data for SNR = 16 dB. Furthermore, the relation between the SNR and performance of the detectors were investigated by plotting this for each detector, for $P_{FA} = 10^{-4}$.

For the evaluation of the kNN classifier, no decision region boundary were visualized due computational complexity, only ROC-curves and SNR-P_d -plots, and for the SVM all three evaluation methods were used for cases when possible. For the ROC-curves, instead of plotting P_{FA} for an evenly spread logarithmic scale, the P_{FA} achieved for the set k neighbors, and γ_{SVM} values respectively, were used. For each chosen k neighbor or γ_{SVM}, a P_{FA} with corresponding P_D were obtained, and plotted as a ROC-curve. This does not lead to an even distribution of P_{FA}, as for the other algorithms, making it slightly harder to compare. As for the SNR-P_d -plot, the P_{FA} closest to 10^{-4} were used to plot the performance for different SNR. For case where a P_{FA} not low enough was reached, allowing a deviation of 2×10^{-4}, no visualization, SNR-P_d -plots, or comparison of ROC-curve with the other algorithms were done, since no fair evaluation could be made.

4

Results

In this section, the results from the different parts of the work will be presented. Firstly cluster dependency of size of steering vector, SNR, and amount of samples used as secondary data will be analyzed. Moreover, a presentation of the data generated for case 2 (20x20) with the STAP-processing will be made together with an analysis of the eigenvalues and behavior of the clusters for larger steering vectors. Furthermore, the performances of the machine learning algorithms implemented will be evaluated for the two different radar configurations, 1x20 and 20x20.Finally, the most prominent ML-detectors were evaluated on all other scenarios than the training data, regarding both covariance estimations and size of steering vector. This was of importance to evaluate their robustness to changes of test data.

Worth noticing when comparing the algorithms are that sometimes the SVM or kNN is not included, which occurs because they did not reach within the limit of the desired P_{FA}. Furthermore, the comparison between the model based algorithms and the MLP and SR, with kNN and SVM in the SNR-P_d -plots, are not entirely accurate, since the P_{FA} of the latter are not set, and could therefore deviate from the P_{FA} used for plotting the others. Moreover, since some of the covariance estimates yield similar data representations in CFAR-FP, only a selection of detector performance results is presented in this section. The larger set of results can be found in the appendix.

4.1 Cluster Characteristics

To study the characteristics of the data when mapped to the CFAR-FP, plots for different amounts of secondary data, levels of SNR and mismatched targets were made to be able to verify the characteristics mentioned in the article. Plots for different SNR were done, which are presented below. The different cases analyzed are SNR of 10 dB and 20 dB respectively. A plot of three levels of SNR all together was also plotted, to be able to see how the clusters behave in comparison to each other. All plots use $K = 2NM$ samples as secondary data, and the same three levels of mismatch (0.2, 0.65, 0.83), and these can be seen below in Figure 4.1.

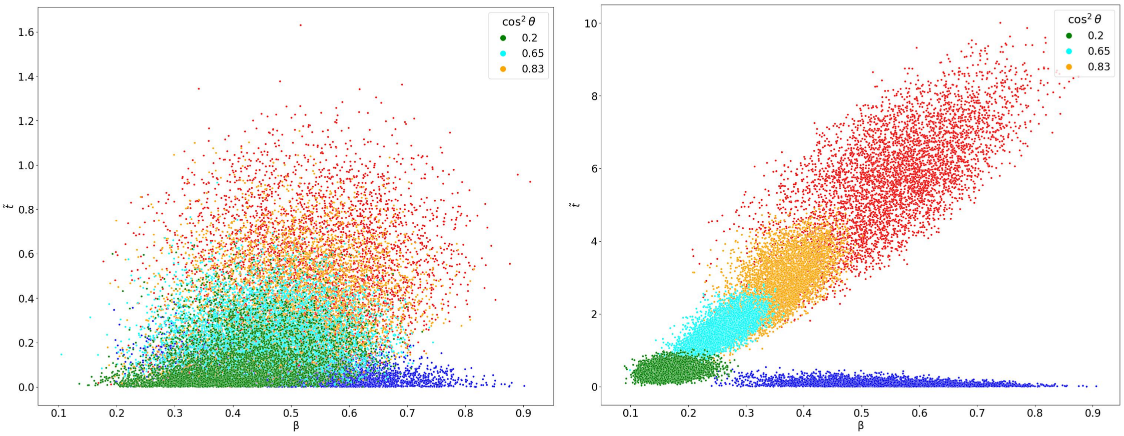

(a) SNR = 10 dB.

(b) SNR = 20 dB.

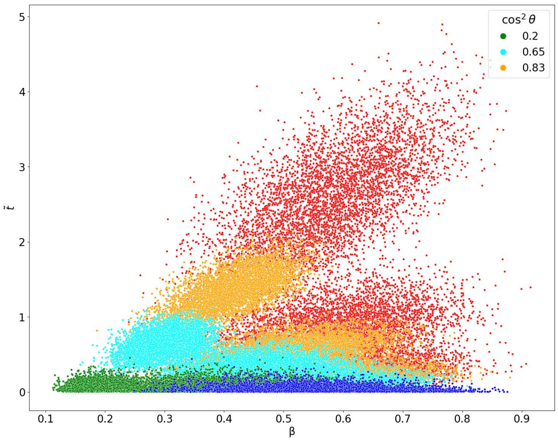

(c) SNR = 10, 15 and 20 dB.

Figure 4.1: Gaussian clutter and targets mapped to the CFAR-FP for different SNR.

What can be seen is that with higher SNR, the targets, both perfect match and mismatched, move upwards in the plane, changing both amplitude and angle. This creates a more distinct separation between the blue clutter, and the different types of targets. Red indicating perfect matched targets in comparison to the nominal steering vector, and the green, orange and cyan clusters are mismatched compared to the same steering vector.

In terms of the level of mismatch, it can be seen that the different clusters of targets are dependent on both β and $\tilde{t}$, making them move according to 2.31 towards the origin with varying level of mismatch. It can also be seen that the rotation of the target clusters decreases with increasing mismatch.

Furthermore, results for three different sizes of secondary data together with the mapping of true covariance using $2NM$ samples can be seen in Figure 4.2. From this, one can see that using $K = 2NM$ samples gives a satisfactory estimate, as expected.

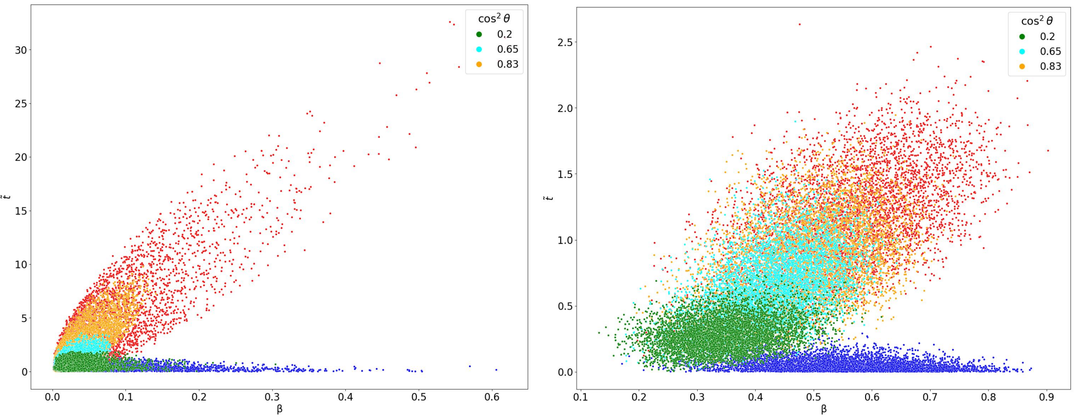

(a) K = NM.

(b) K = 2NM.

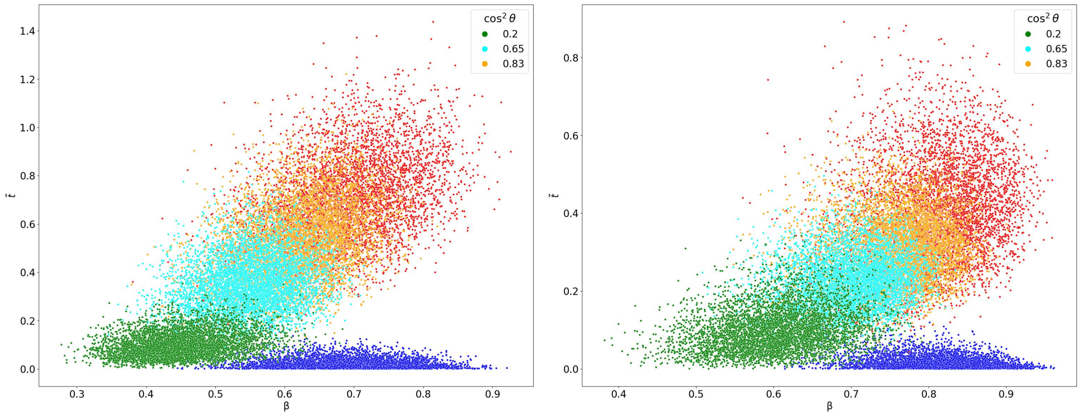

(c) K = 2NM true covariance matrix **C**.

(d) K = 5NM.

Figure 4.2: Gaussian clutter and targets mapped to the CFAR-FP for different values for K. SNR = 15 dB.

Two different methods for regularization were also implemented and evaluated, Diagonal loading and FML. These were used in combination with two different sizes of secondary data, K = NM and K = 2NM, to see how the clusters were affected by the amount of information about the clutter, and if there is a possibility to get separated cluster with just a small amount of secondary data. The results of this can be seen in Figure 4.3.

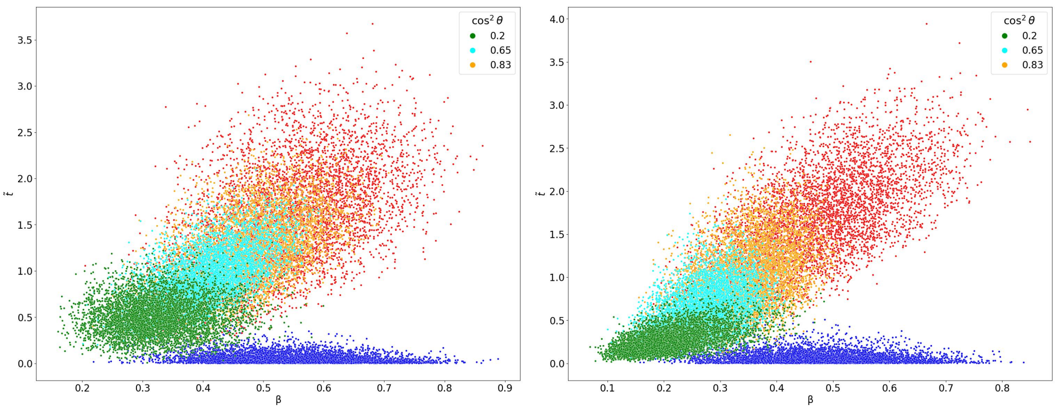

(a) K = NM with DL.

(b) K = NM with FML.

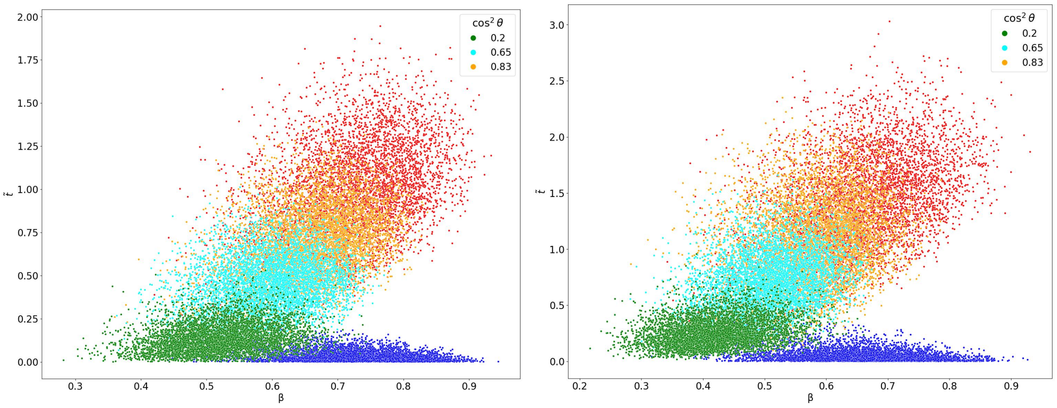

(c) K = 2NM with DL.

(d) K = 2NM with FML.

Figure 4.3: Gaussian clutter and targets for different methods of estimating **S**. SNR = 15 dB.

As can be seen, when the amount of secondary data is increased, all clusters moves towards the right corner (along the x-axis), cluster ellipses for targets is increasing, making them more separable. This also occurs when applying either FML or DL, indicating that the cluster intersection depends on the amount of contributory eigenvalues in the estimated covariance matrix, making it possible to get well separated clusters using a small amount of samples as secondary data. However, it is important to know that when using these regularization techniques CFAR is not guaranteed as the statistics of the covariance becomes unknown.

Visualizations of the resulting clusters and corresponding eigenvalues, for each combination of secondary data size and covariance estimation method, are provided to support interoperability and validate clustering behavior, as shown in Figure 4.4. A complete set of figures is available in Appendix A. The regularization methods affect the eigenvalues as expected, which makes the clusters for clutter and targets separable when $K \leq NM$ for SNR 16 dB. This shows potential for the detector implementations at this SNR. However, as stated earlier, for lower SNR, the amplitude of targets point representation decreases, meaning the performance will decrease. One comment on the case $K = NM$ for both cases: the result from the mapping does not form clusters and the generic behavior in this study disappears.

Hence, these cases were not studied further for detector implementations.

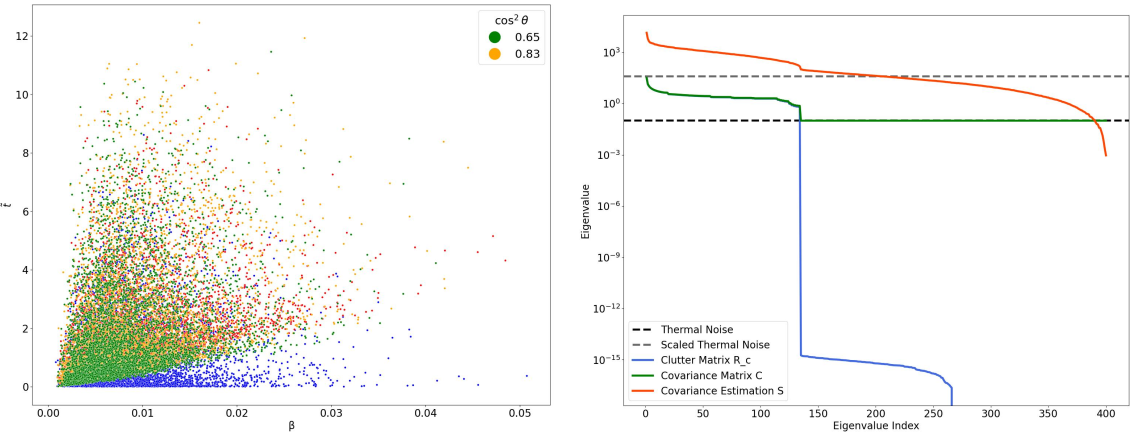

(a) Original estimate **S**.

(b) Eigenvalues for original estimate **S**.

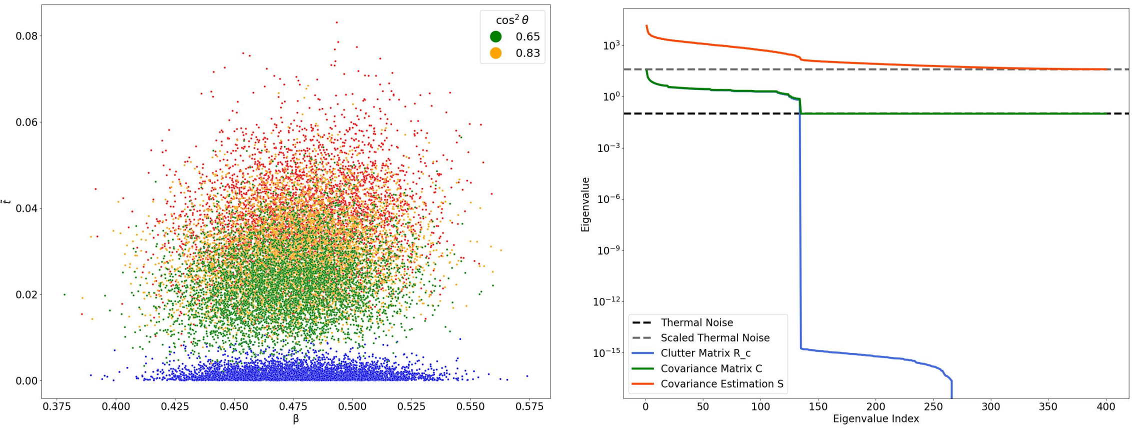

(c) Diagonally loaded **S**.

(d) Eigenvalues for diagonally loaded **S**.

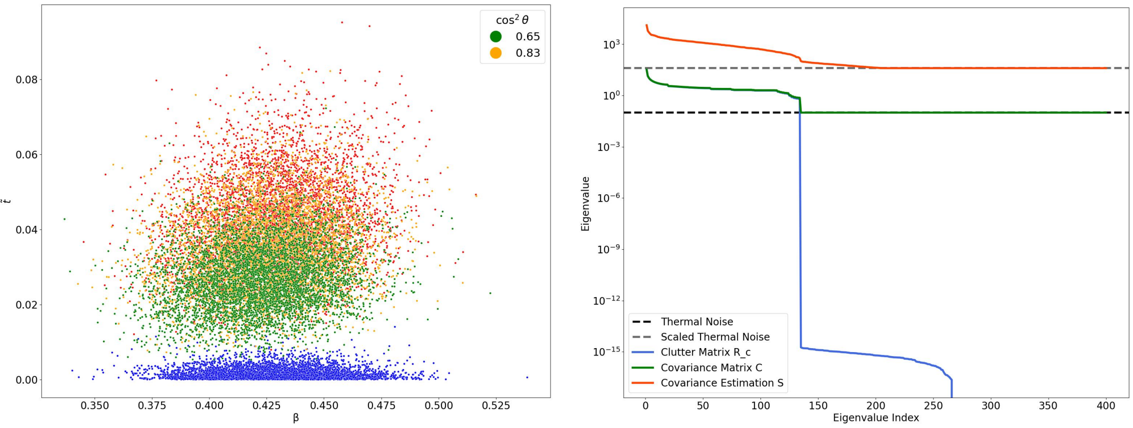

(e) FML estimate **S**.

(f) Eigenvalues for FML estimate **S**.

Figure 4.4: Clusters and eigenvalues of **S** for K = NM, N = 20, M = 20, SNR = 15 dB. Orange lines is eigenvalues for estimated covariance matrix. Green lines is eigenvalues for actual covariance and blue lines is the eigenvalues for clutter only covariance matrix.

Cluster behavior for mapped data for case 2 with configuration N = 20, M = 20, is shown in Figure 4.5.

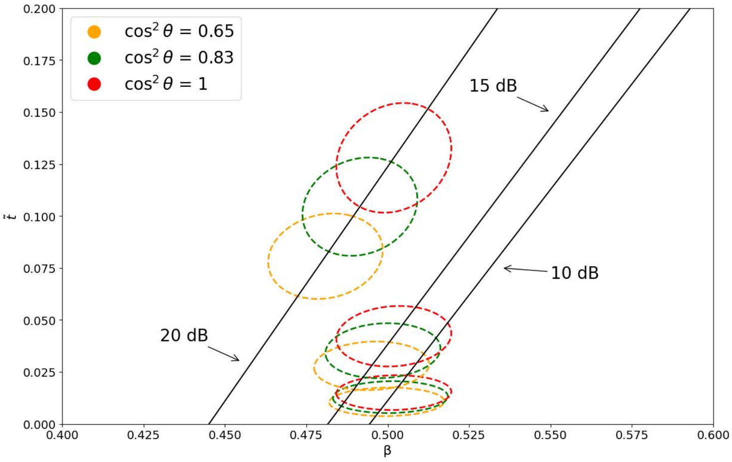

Figure 4.5: Cluster behavior for N = 20 M = 20 for different levels of SNR, K = 2NM.

As can be seen, the previously described cluster behavior does not apply to larger radar configurations as N = 20 and M = 20, and especially for lower SNR levels, where there are a substantial overlap of the different target since they approach the clutter. Additional tests were conducted to investigate how cluster characteristics depend on the dimension of the steering vector, which can be seen in Figure 4.6.

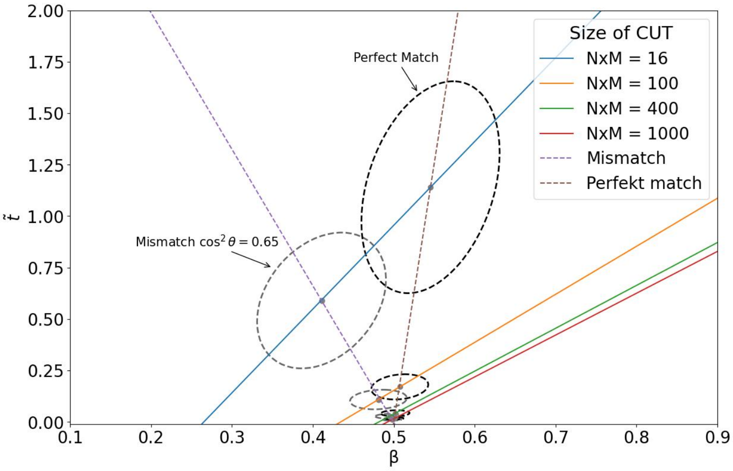

Figure 4.6: Varying length of steering vector, K = 2NM.

In general, longer steering vectors require higher SNR for the clusters to become distinct and exhibit the general behavior previously observed for low-dimensional steering vectors. For the configurations considered in this study, it was found that the case with N = 20, M = 20 tends to exhibit similar cluster behavior to the N = 1 case when the SNR exceeds 15 dB. Below this SNR, the overlap between clusters corresponding to mismatched and perfectly matched targets, and the clutter increases. Additionally, the cluster for mismatched targets shows less dependency on β, leading to further overlap with the clutter cluster.

To describe this further, an analysis of the asymptotic behaviors of the center point of matched and mismatched cluster was made when the size of the CUT grows larger. In Figure 4.7 it can be seen that when the size of NM is increased, all values of β goes towards a value of 0.5, and all values of $\tilde{t}$ approaches zero, which indicates that all clusters goes towards the clutter center.

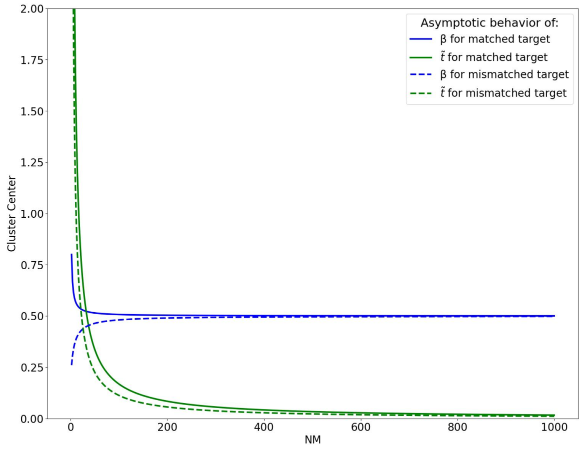

Figure 4.7: Asymptotic behavior of the center of matched and mismatched clusters, SNR = 15 dB, K = 2NM.

4.2 Detection Models

After the mapping was done for the different radar scenarios, multiple detectors were implemented. As a start, traditional model-based detectors were implemented and evaluated, to get a performance benchmark. Moreover, data-driven ML-detectors were also implemented and evaluated together with the model-based ones.

4.2.1 Traditional Detectors

Some of the traditional detectors were plotted and evaluated in the feature plane. This was done for a P_{FA} of 10^{-4}, using the data from Figure 4.8. Here, the blue clusters are clutter, red perfect matched targets, and cyan mismatched targets with a level of 0.65.

The traditional detectors plotted were Kelly, AMF, ABORT, and ACE, and the following plots show their appearance in different types of data with the same amount of secondary data ($K = 2NM$), and all with the same P_{FA}.

Since the appearance of the detectors in the CFAR-FP only depends on the clutter, all of those will have the same appearance and P_{FA}, but what will differ is their performance for different types of data.

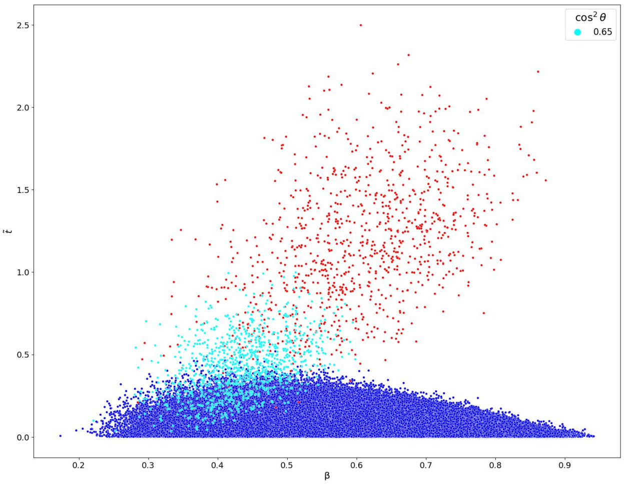

Figure 4.8: Data used for threshold tuning.

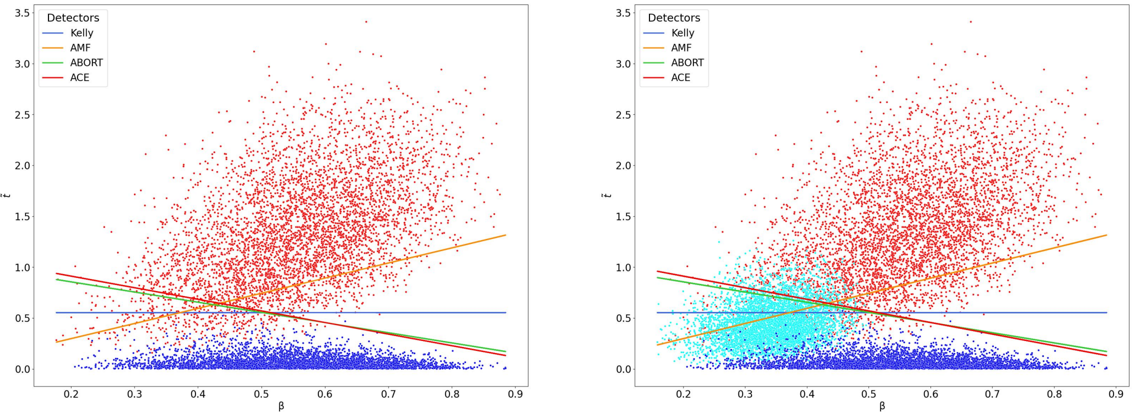

(a) Matched, SNR = 15 dB. (b) Mismatched, SNR = 15 dB.

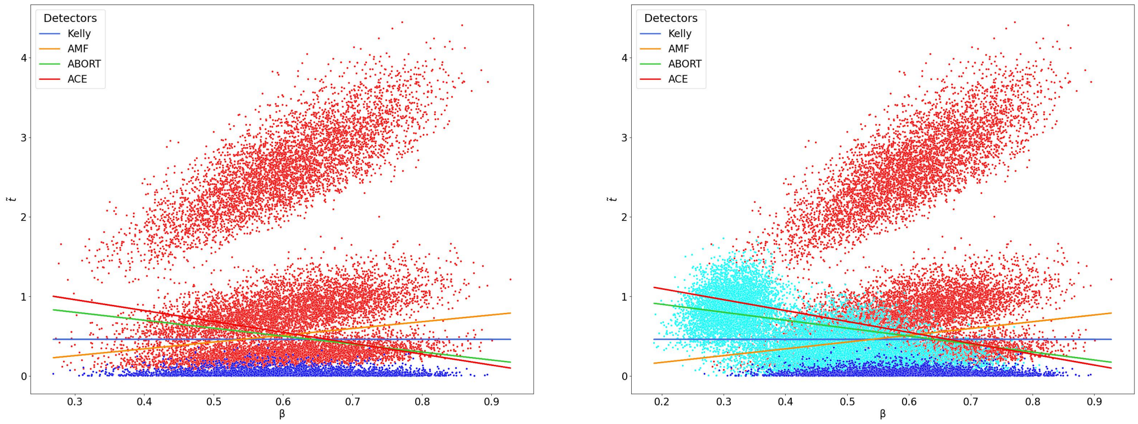

(c) Matched, SNR = 10, 15 and 20 dB. (d) Mismatched, SNR = 10, 15 and 20 dB.

Figure 4.9: Traditional detectors in the CFAR-FP.

To evaluate the performance of the detectors, ROC-curves were plotted for the scenarios with SNR = 15 dB, and also for the case with multiple levels of SNR, for targets and mismatched targets separately.

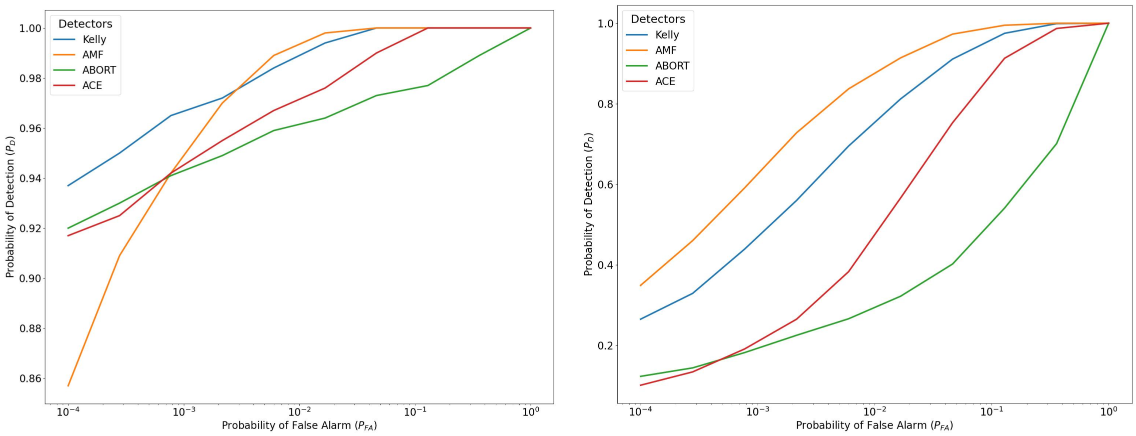

(a) Matched conditions.

(b) Mismatched conditions.

Figure 4.10: ROC-curves for SNR = 15 dB.

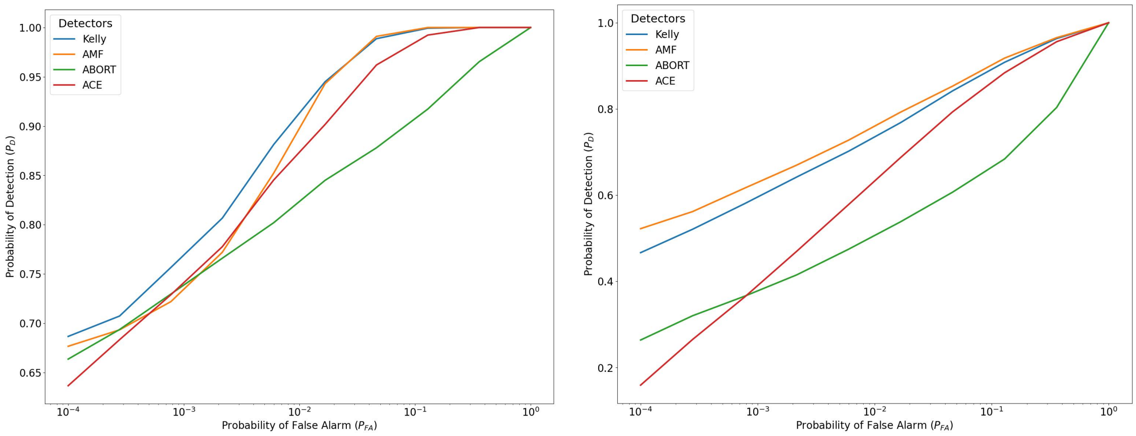

(a) Matched conditions.

(b) Mismatched conditions.

Figure 4.11: ROC-curves for SNR = 10, 15 and 20 dB combined.

As can be seen in figure 4.10, Kelly performs best at low P_{FA} for matched targets, while AMF performs best at mismatched targets. For the case with multiple SNRs, Kelly still performs best under matched conditions, and AMF for mismatched conditions.

4.2.2 Detector Performance Evaluation

Results from the detector implementations, both model based and new implementations will be presented here in metrics of ROC-curves and SNR-P_D -plots. Performance of the detectors for a selection of covariance estimates are shown in Figure 4.12 - 4.15, all results can be found in Appendix B for 1 antenna and in Appendix C for 20 antennas.

The overall performance is high, and the implementations remain effective under matched and mismatched conditions for most covariance estimates when compared to Kelly's pioneering detector and AMF under matched and mismatched conditions respectively. The MLP demonstrates strong robustness and consistently ranks among the top-performing detectors. Regarding the SR detector, since it fits a function to separate the data which differs a lot between the different cases and runs, this model can be seen as somewhat more sensitive to the distribution of the training data. Both kNN and SVM performs, for the most cases, worse than both the MLP and SR, but still in line with most of the model based ones.

4.2.2.1 Case 1

For diagonally loaded $K = 2NM$, the trained and threshold-tuned MLP and SR demonstrates performance comparable and even better than Kelly's detector. This also illustrates why Kelly's detector is as renowned with a ROC-curve close to the optimal and P_D close to 1 from and above $\gamma = 14$ dB. This similarity is explained by the corresponding decision boundaries, which are similar, although the MLP has a slightly positive slope (see Figure 4.12). Regarding both kNN and SVM, their performance does not compare to the MLP or SR, with SVM performing a bit better than kNN on lower SNR, but not as good as the others. For two of the estimations of **S**, the kNN did not reach the desired P_{FA} and will not be included in the comparison. In Table 4.1 and 4.2, the variables used and their corresponding P_{FA}, for kNN and SVM can be seen.

Estimation of **S**	# of Neighbors (k)	P_{FA}
K = 2NM	-	-
K = 0.5NM with DL	-	-
K = NM with DL	1000	3.2×10^{-4}
K = 2NM with DL	1000	2.8×10^{-5}
K = 0.5NM with FML	7500	6×10^{-5}
K = NM with FML	5000	4×10^{-5}
K = 2NM with FML	500	1.7×10^{-4}

Table 4.1: Number of neighbors and corresponding P_{FA} for kNN.

Estimation of **S**	γ_{SVM}	P_{FA}
K = 2NM	0.09	1.4×10^{-4}
K = 0.5NM with DL	0.07	1.2×10^{-4}
K = NM with DL	0.09	5×10^{-5}
K = 2NM with DL	0.09	8×10^{-5}
K = 0.5NM with FML	0.09	4×10^{-5}
K = NM with FML	0.09	4×10^{-5}
K = 2NM with FML	0.09	2×10^{-5}

Table 4.2: Value of γ_{SVM} and corresponding P_{FA} for SVM.

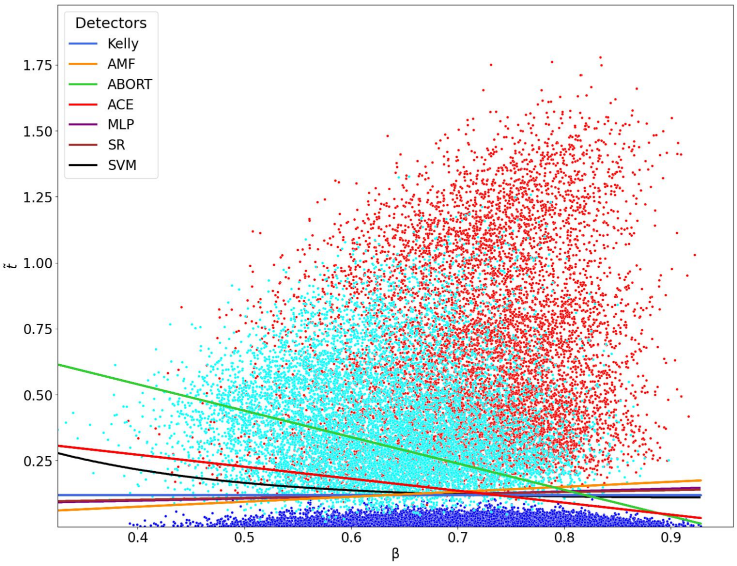

(a) Different detectors in the CFAR-FP for 1 antenna.

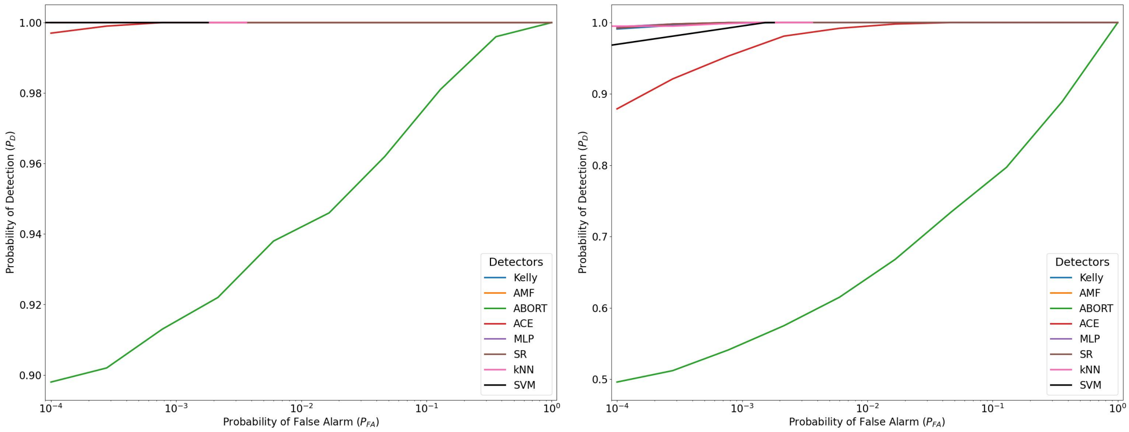

(b) ROC matched targets.

(c) ROC mismatched targets.

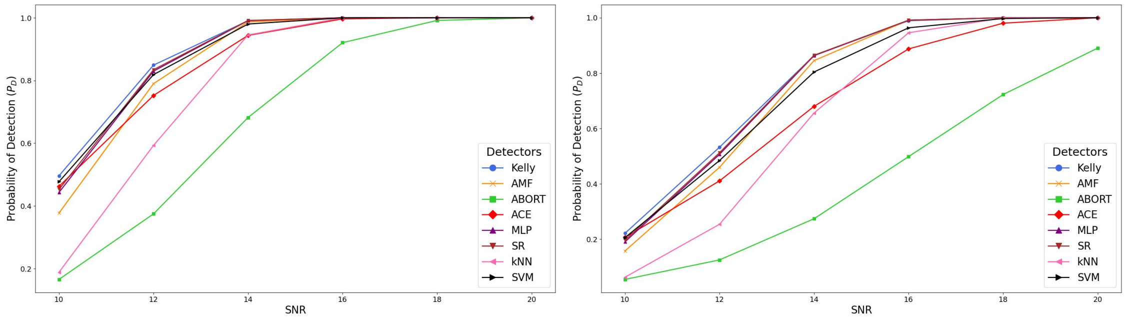

(d) SNR-P_D matched targets.

(e) SNR-P_D mismatched targets.

Figure 4.12: Results for K = 2NM, **S** diagonally loaded. (a) SNR = 14-20 dB, (b)-(c) SNR = 16 dB, (d)-(e) SNR = 10-20 dB.

The developed detectors show particularly promising results when using covariance estimates with $K = 0.5NM$ samples as secondary data, in combination with diagonal loading or FML estimate. The latter is shown in Figure 4.13. Although the overall probability of detection decreases in these scenarios, the proposed detectors outperforms traditional methods and has relatively high performance at smaller SNR.

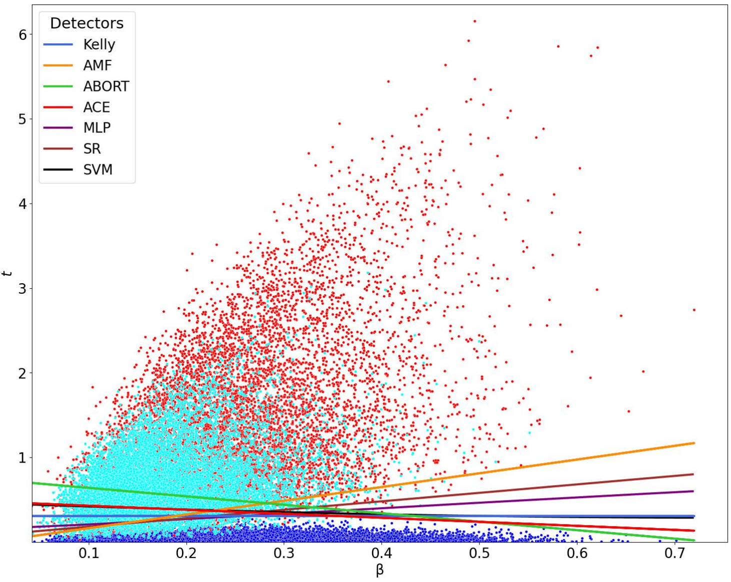

(a) Different detectors in the CFAR-FP for 1 antenna.

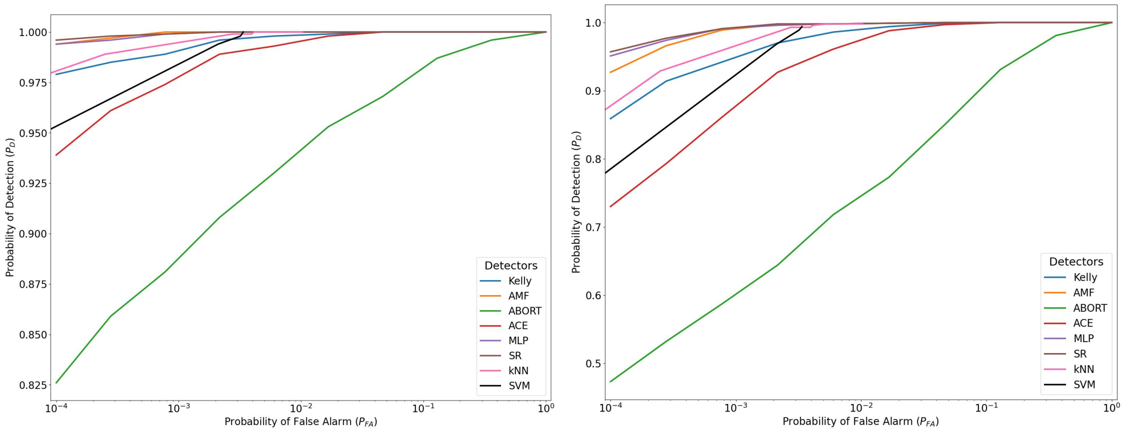

(b) ROC matched targets.

(c) ROC mismatched targets.

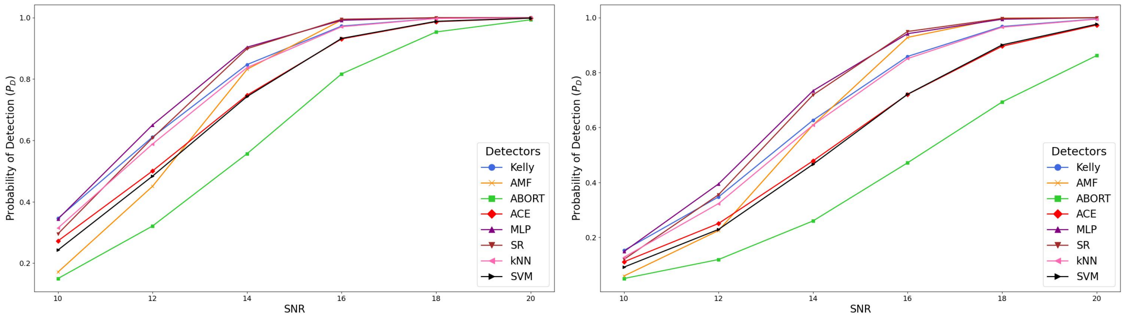

(d) SNR-P_D matched targets.

(e) SNR-P_D mismatched targets.

Figure 4.13: Results for K = 0.5NM, **S** FML estimate. (a) SNR = 14-20 dB, (b)-(c) SNR = 16 dB, (d)-(e) SNR = 10-20 dB.

4.2.2.2 Case 2

Figures 4.14 and 4.15 show results for the configuration N = 20, M = 20, where performance across all detectors evaluated are very similar. This similarity is a consequence of the distribution of points in the CFAR-FP, where nested clusters emerge. As a result, all detectors begin to converge toward the statistics of Kelly's detector, which becomes efficient when classifying binary data with this distribution. As for case 1, for some estimations of **S**, SVM will not reach the desired P_{FA} and will therefore not be shown. The variables used and their corresponding P_{FA}, can be seen in Table 4.3 and 4.4 for kNN and SVM respectively.

Estimation of **S**	# of Neighbors (k)	P_{FA}
K = 2NM	5000	10^{-4}
K = 0.5NM with DL	9000	5×10^{-5}
K = NM with DL	1000	2.8×10^{-4}
K = 2NM with DL	1000	3×10^{-5}
K = 0.5NM with FML	9000	10^{-4}
K = NM with FML	1000	2.2×10^{-4}
K = 2NM with FML	500	1.2×10^{-4}

Table 4.3: Number of neighbors and corresponding P_{FA} for kNN.

Estimation of **S**	γ_{SVM}	P_{FA}
K = 2NM	-	-
K = 0.5NM with DL	0.5	10^{-5}
K = NM with DL	0.5	1.2×10^{-4}
K = 2NM with DL	0.5	4×10^{-5}
K = 0.5NM with FML	-	-
K = NM with FML	0.5	3×10^{-5}
K = 2NM with FML	0.5	4×10^{-5}

Table 4.4: Value of γ_{SVM} and corresponding P_{FA} for SVM.

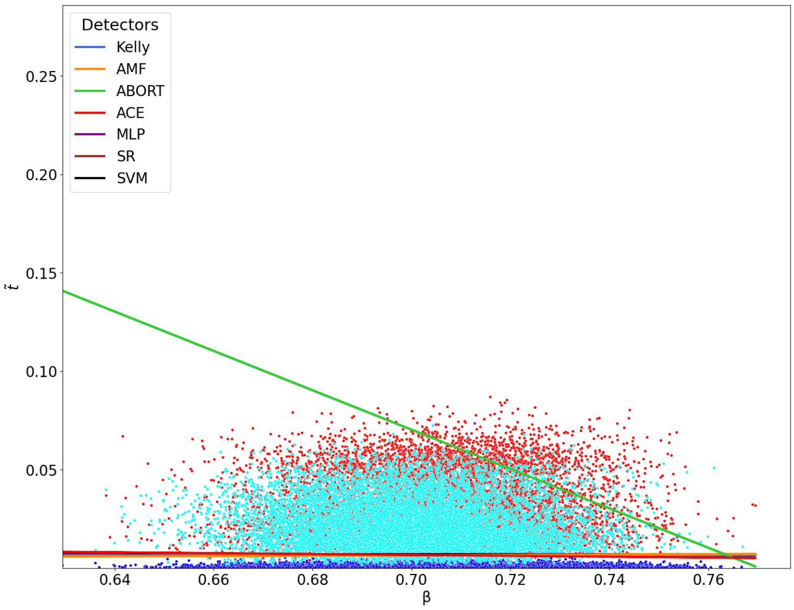

(a) Different detectors in the CFAR-FP for 20 antennas.

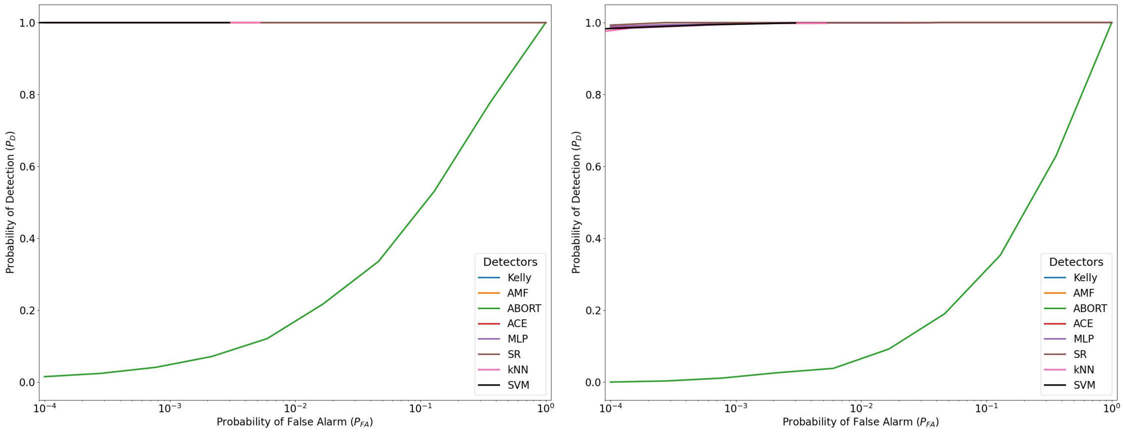

(b) ROC matched targets.

(c) ROC mismatched targets.

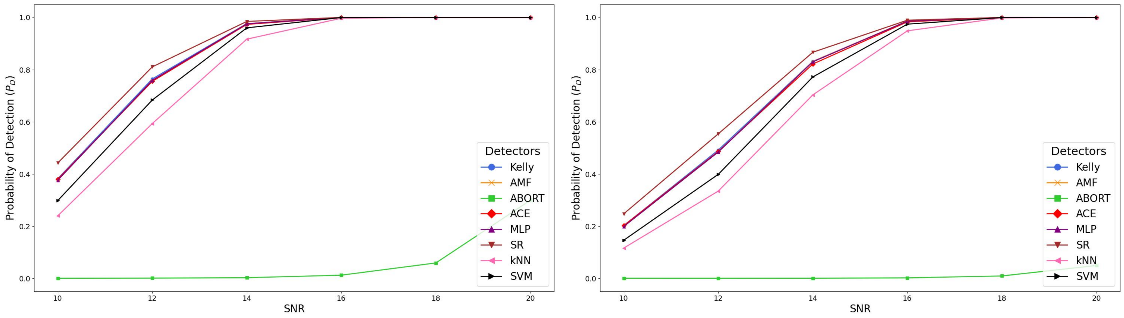

(d) SNR-P_D matched targets.

(e) SNR-P_D mismatched targets.

Figure 4.14: Results for K = 2NM, **S** diagonally loaded. (a) SNR = 14-20 dB, (b)-(c) SNR = 16 dB, (d)-(e) SNR = 10-20 dB.

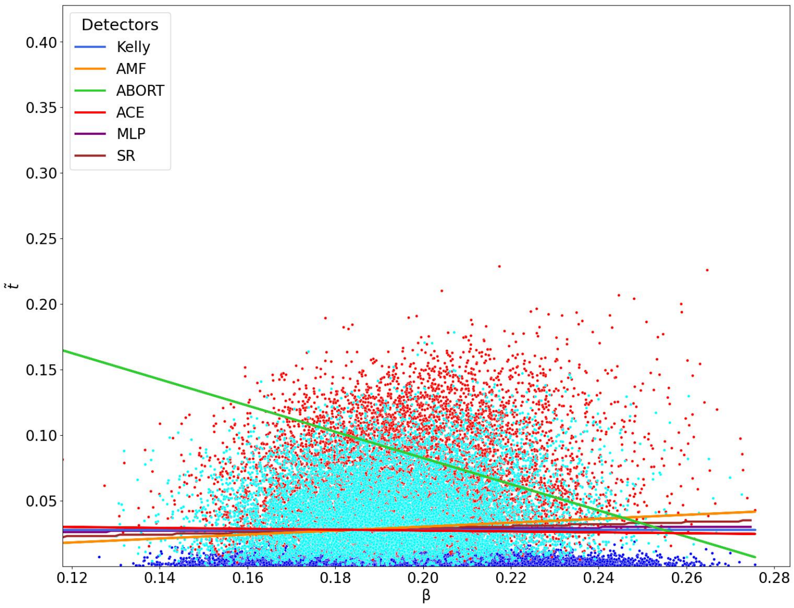

(a) Different detectors in the CFAR-FP for 20 antennas.

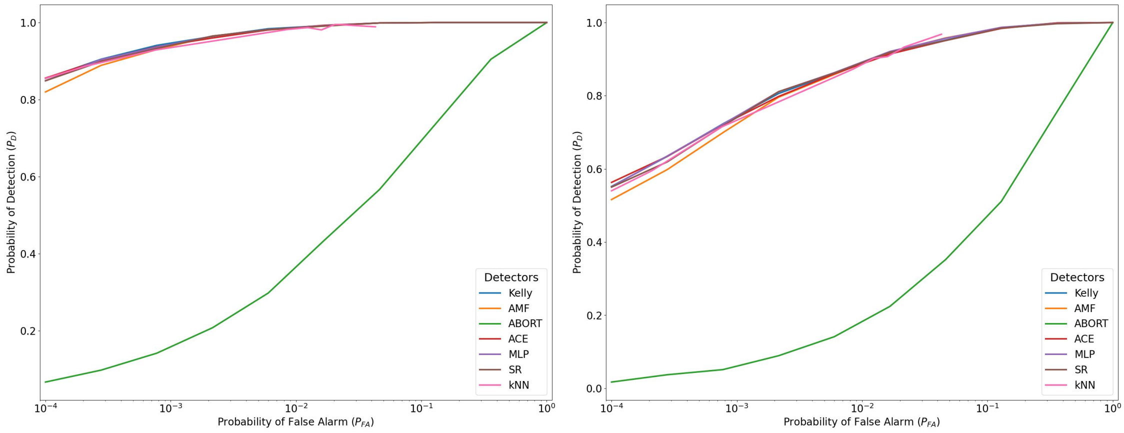

(b) ROC matched targets. (c) ROC mismatched targets.

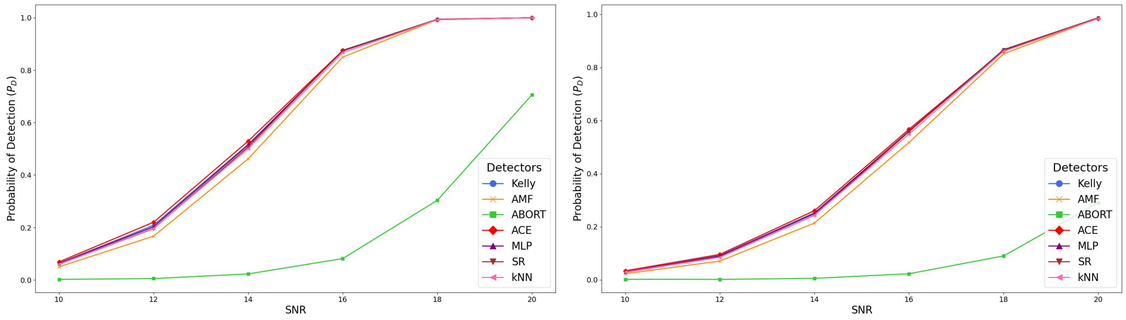

(d) SNR-P_D matched targets. (e) SNR-P_D mismatched targets.

Figure 4.15: Results for K = 0.5NM, **S** FML estimate. (a) SNR = 14-20 dB, (b)-(c) SNR = 16 dB, (d)-(e) SNR = 10-20 dB.

4.2.2.3 Final Evaluation

Since the MLP and SR performs very well on most of the radar scenarios, it was decided to evaluate the models trained on the most prominent case for other scenarios than the training data. The models trained on $K = 0.5NM$ with FML for case 1 were chosen, since this was where the performance of the ML-algorithms stood out the most. The results from the the use of these algorithms on case 2 for $K = 0.5NM$ with FML, and on case 1 and 2 for $K = 2NM$, will be presented, and the rest can be seen in Appendix D.

What can be seen is that the two trained detectors does not perform well on data other than the training scenario. Especially, it performs much worse than most of the other detectors on larger radar cases, see Figure 4.16 and 4.18. For case 1, the difference in performance is not that remarkable. They can not compete with, for example Kelly, in any of the scenarios, but the MLP still shows a decent performance for low P_{FA}. For lower levels of SNR, non of the ML-detectors performs satisfactory. What can be concluded from this is that the ML-detectors are not robust to changes of test data, and only performs well on training data, making them unfeasible to use in real-time applications at current stage.

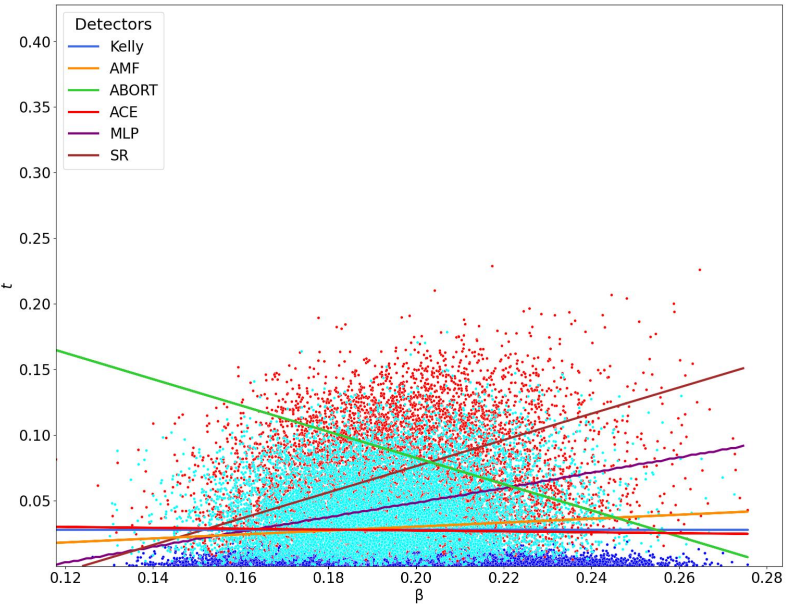

(a) Different detectors in the CFAR-FP for 20 antennas.

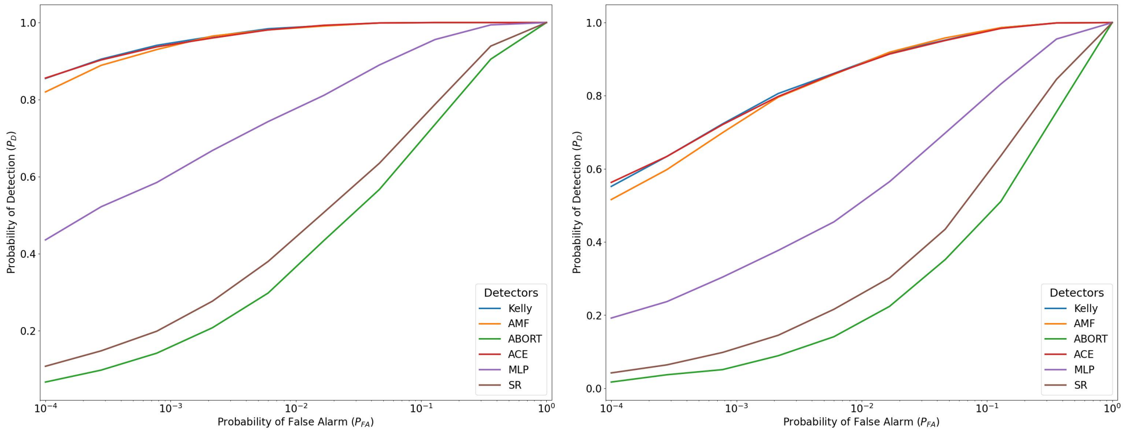

(b) ROC matched targets.

(c) ROC mismatched targets.

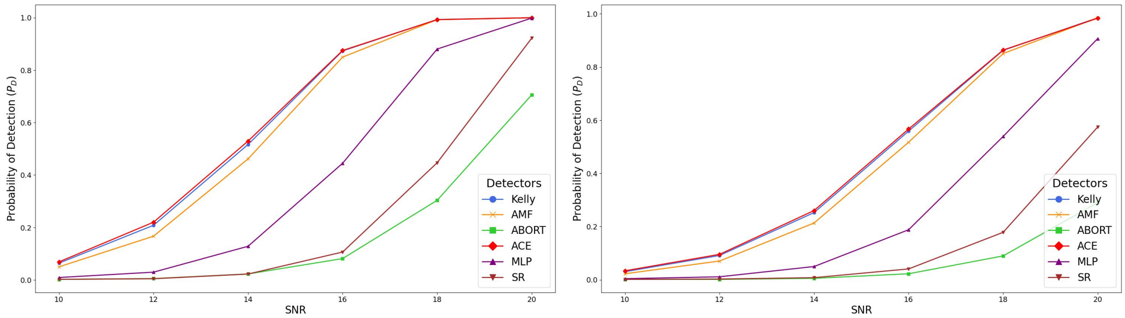

(d) SNR-P_D matched targets.

(e) SNR-P_D mismatched targets.

Figure 4.16: Results for K = 0.5NM for Case 2, **S** FML estimated with detectors trained on K = 0.5NM with FML for Case 1. (a) SNR = 14-20 dB, (b)-(c) SNR = 16 dB, (d)-(e) SNR = 10-20 dB.

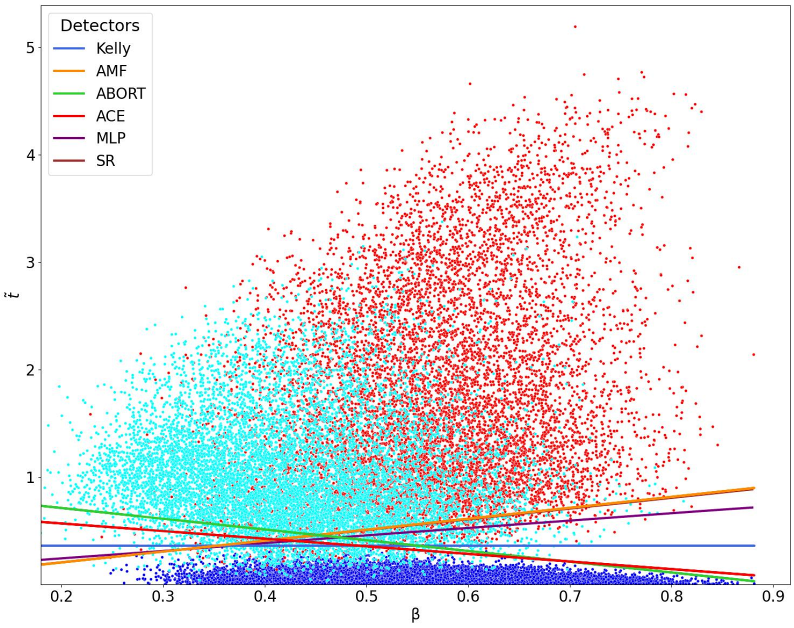

(a) Different detectors in the CFAR-FP for 1 antenna.

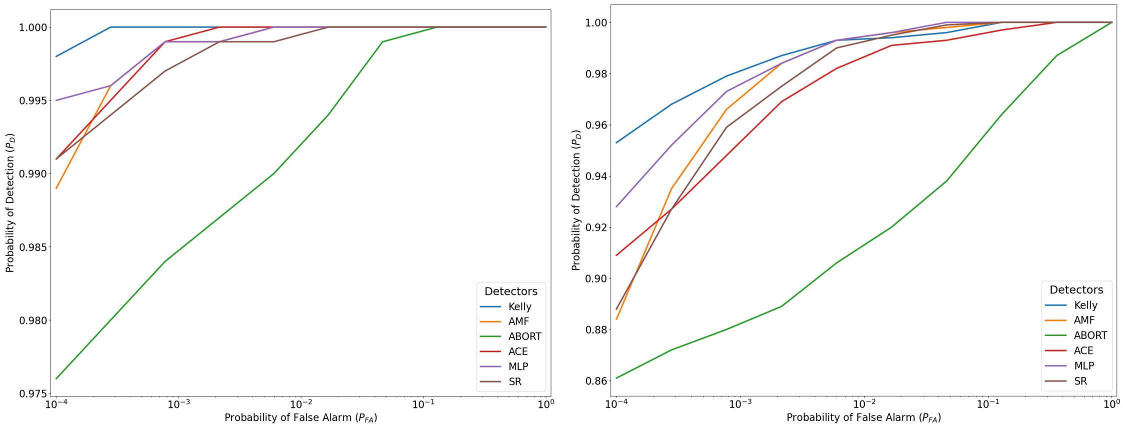

(b) ROC matched targets. (c) ROC mismatched targets.

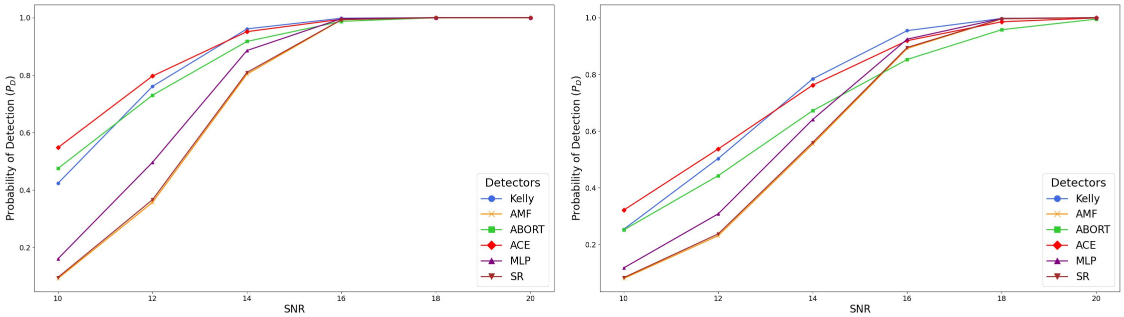

(d) SNR-P_D matched targets. (e) SNR-P_D mismatched targets.

Figure 4.17: Results for K = 2NM for Case 1 with detectors trained on K = 0.5NM with FML for Case 1. (a) SNR = 14-20 dB, (b)-(c) SNR = 16 dB, (d)-(e) SNR = 10-20 dB.

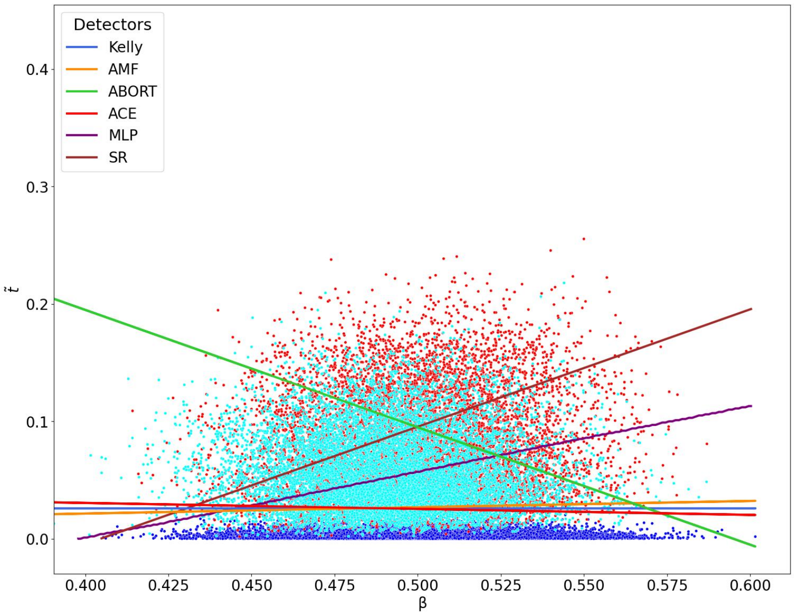

(a) Different detectors in the CFAR-FP for 20 antennas.

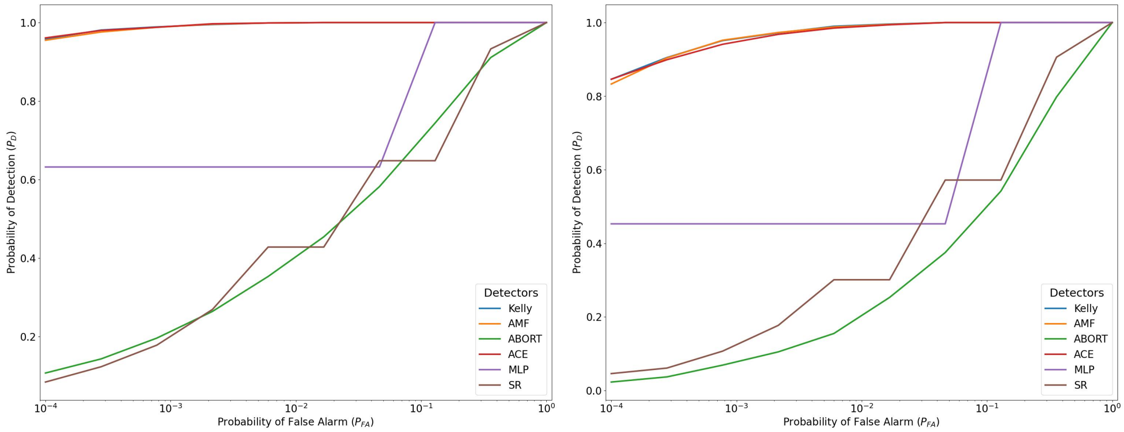

(b) ROC matched targets.

(c) ROC mismatched targets.

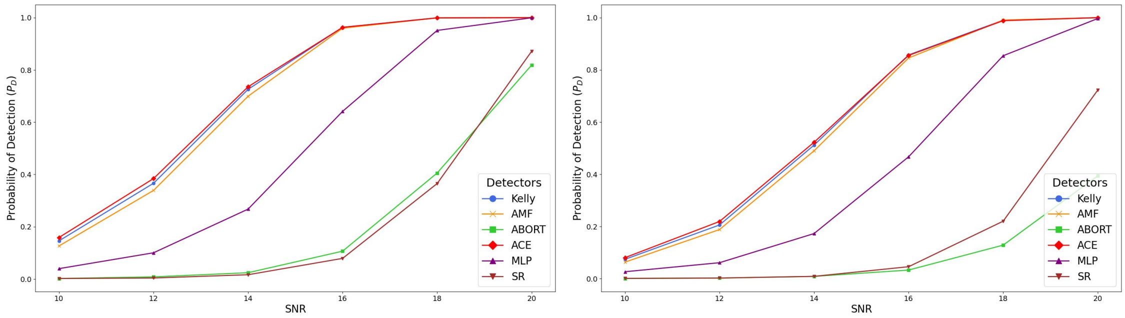

(d) SNR-P_D matched targets.

(e) SNR-P_D mismatched targets.

Figure 4.18: Results for K = 2NM for Case 2 with detectors trained on K = 0.5NM with FML for Case 1. (a) SNR = 14-20 dB, (b)-(c) SNR = 16 dB, (d)-(e) SNR = 10-20 dB.

5

Conclusion

From this work, multiple conclusions can be drawn regarding both cluster behavior in CFAR-FP, as well as the performance of implemented data-driven machine learning detectors. Regarding the clusters, it was found that for smaller steering vectors, the clutter, but also the different targets, were highly affected of how the covariance matrix was estimated. When larger amount of secondary data was used for estimation, the clusters became more separable, since the center of the cluster of clutter moved towards the maximum value of β in the feature plane. The same behavior could be seen for DL and FML used as methods for regularization, indicating that the more information used when estimating $\mathbf{S}$, the better separation of the clusters are presented. As for the influence of the level of mismatch on the targets, it could be seen that if the mismatch increased in terms of the angle between the nominal and actual steering vector, the targets moved towards the origin, getting closer to the clutter in terms of $\tilde{t}$. The same occurs when observing lower levels of SNR, the amplitude of targets approaches the clutter cluster.

When increasing the size of the radar case, it was found the the behavior observed for smaller CUTs was no longer as strong, and therefore removing a lot of the dependencies useful when implementing data-driven detectors. The most prominent change of behavior found when the dimensions were increased was the impact on the mismatch. As mentioned above, when the mismatch for lower dimension data was increased, the targets moved towards the origin, still depending on β. When the dimensions then were increased, the impact on $\tilde{t}$ still remained, but the dependency of β decreased significantly, leading to a great overlap of targets, mismatched targets, and clutter, even for higher levels of SNR. This lead to almost no distinct clusters to classify for lower SNR. After an analysis of how the centers of all the target clusters moved in terms the size of the steering vector, it was found that all centers approaches the clutter when the size is increased, leading to a need of higher SNR to be able to separate them from each other.

Conclusions about the detectors can also be made. Regarding the smaller case (case 1), both the MLP and SR performs as good as, or sometimes even better, than both Kelly's detector for matched targets, and AMF for mismatched targets, with the MLP being a bit more robust to the distribution of the data, as well as the different estimations of $\mathbf{S}$. Regarding both kNN and SVM, they did not outperform the majority of the model based detectors, nor the other two data-driven ones. Those results in comparison with the fact that their prediction time is relatively long, they can not be seen as suitable options for detection at this stage. MLP and SR, on the other hand, can be since their performance excels for both matched and mismatched data for most of the estimations of $\mathbf{S}$. Especially the MLP could be seen as a great addition to the traditional detector because of its robustness to the distribution of the data, together with its promising performance.

Regarding the performance of the detectors for case 2, it could be seen that they were highly affected by the appearance of the clusters. Almost all detectors, model based and data driven, approached the appearance of the Kelly detector, giving next to no deviation in the results. What can be concluded from this is that Kelly's detector is the best for handling all sorts of data in the CFAR-FP for higher dimensions.

Finally, implemented ML-detectors is sensitive and limited to its trained scenario and does not generalize well to other settings, this is regarding both covariance estimations and size of radar case. A reason for this could be, for example, that the covariance estimation and steering vector is used when mapping the data to the CFAR-FP, affecting the clusters highly. If the ML-detector is trained to learn only the parameters β and $\tilde{t}$ of the data, and those differs a lot for different cases, it will not be able to classify the data. A third dimension not differing between different cases would be needed to be able to get a ML-detector robust to changes in the data.

5.1 Future work

There are multiple ways to extend this work further. One interesting approach could be to add another dimension to CFAR-FP, and analyze how this affects the clusters, to hopefully be able to see some kind of separation even for higher dimensions, and possibly train data driven detectors to outperform the model based ones.

Furthermore, the computational complexity and execution time for detection of the implemented machine learning detectors should be investigate, since time is of great importance when detecting targets in real time.

To extend towards a real application of the problem, the CFAR-FP should be evaluated for non gaussian clutter as well, since clutter would not follow this distribution for practical scenarios.

Bibliography

[1] A. Coluccia, A. Fascista, and G. Ricci, “CFAR feature plane: A novel framework for the analysis and design of radar detectors,” *IEEE Transactions on Signal Processing*, vol. 68, Jul. 3, 2020.

[2] A. Coluccia, A. Fascista, and G. Ricci, “Design of customized adaptive radar detectors in the CFAR feature plane,” *IEEE Transactions on Signal Processing*, vol. 70, Nov. 7, 2022.

[3] A. Coluccia, *Adaptive Radar Detection: Model-based, Data-driven, and Hybrid Approaches*. Boston, London: Artech House, 2023.

[4] A. Coluccia, A. Fascista, and G. Ricci, “Robust cfar radar detection using a k-nearest neighbors rule,” in *ICASSP 2020 - 2020 IEEE International Conference on Acoustics, Speech and Signal Processing (ICASSP)*, 2020, pp. 4692–4696. DOI: `10.1109/ICASSP40776.2020.9054283`.

[5] B. Carlson, “Covariance matrix estimation errors and diagonal loading in adaptive arrays,” *IEEE Transactions on Aerospace and Electronic Systems*, vol. 24, no. 4, pp. 397–401, Jul. 1988, ISSN: 00189251. DOI: `10.1109/7.7181`. [Online]. Available: `http://ieeexplore.ieee.org/document/7181/` (visited on 04/10/2025).

[6] K. Gerlach and M. Steiner, “Fast converging adaptive processor or a structured covariance matrix,” *IEEE Transactions on Aerospace and Electronic Systems*, vol. 36, no. 4, pp. 1115–1126, Oct. 2000, ISSN: 00189251. DOI: `10.1109/7.892662`. [Online]. Available: `http://ieeexplore.ieee.org/document/892662/` (visited on 04/09/2025).

[7] M. A. Richards, J. A. Scheer, and W. A. Holm, *Principles of Modern Radar, Volume I - Basic Principles*. SciTech Publishing, Aug. 3, 2011, vol. I.

[8] J. R. Guerci, *Space-time adaptive processing for radar* (Artech House radar series), eng, Second edition. Boston London: Artech House, 2015, ISBN: 9781608078202.

[9] A. Hero, “Signal Detection and Classification,” en, in *Digital Signal Processing Fundamentals*, vol. 20094251, CRC Press, Nov. 2009, pp. 1–15, ISBN: 9781420046069 9781420046076. DOI: `10.1201/9781420046076-c13`. [Online]. Available: `http://www.crcnetbase.com/doi/abs/10.1201/9781420046076-c13` (visited on 01/27/2025).

[10] F. Bandiera, D. Orlando, and G. Ricci, *Advanced Radar Detection Schemes Under Mismatched Signal Models* (Synthesis Lectures on Signal Processing), en. Cham: Springer International Publishing, 2009, ISBN: 9783031014048 9783031025327. DOI: `10.1007/978-3-031-02532-7`. [Online]. Available: `https://link.springer.com/10.1007/978-3-031-02532-7` (visited on 01/27/2025).

[11] T. Diskin, Y. Beer, U. Okun, and A. Wiesel, "CFARnet: Deep learning for target detection with constant false alarm rate," *Signal Processing*, vol. 223, p. 109 543, Oct. 1, 2024, ISSN: 0165-1684. DOI: `10.1016/j.sigpro.2024.109543`. [Online]. Available: `https://www.sciencedirect.com/science/article/pii/S0165168424001622` (visited on 01/27/2025).

[12] S. Bose and A. Steinhardt, "A maximal invariant framework for adaptive detection with arrays," in *[Proceedings] ICASSP-92: 1992 IEEE International Conference on Acoustics, Speech, and Signal Processing*, vol. 5, 1992, 357–360 vol.5. DOI: `10.1109/ICASSP.1992.226609`.

[13] A. De Maio, "Invariance theory for adaptive radar detection in heterogeneous environment," *IEEE Signal Processing Letters*, vol. 26, no. 7, pp. 996–1000, 2019. DOI: `10.1109/LSP.2019.2916749`.

[14] J. Klintberg, T. McKelvey, and P. Dammert, "A parametric approach to space-time adaptive processing in bistatic radar systems," *IEEE Transactions on Aerospace and Electronic Systems*, vol. 58, no. 2, pp. 1149–1160, 2022. DOI: `10.1109/TAES.2021.3122520`.

[15] I. Reed, J. Mallett, and L. Brennan, "Rapid Convergence Rate in Adaptive Arrays," *IEEE Transactions on Aerospace and Electronic Systems*, vol. AES-10, no. 6, pp. 853–863, Nov. 1974, ISSN: 0018-9251. DOI: `10.1109/TAES.1974.307893`. [Online]. Available: `http://ieeexplore.ieee.org/document/4101326/` (visited on 04/10/2025).

[16] C. Peckham, A. Haimovich, T. Ayoub, J. Goldstein, and I. Reid, "Reduced-rank stap performance analysis," *IEEE Transactions on Aerospace and Electronic Systems*, vol. 36, no. 2, pp. 664–676, 2000. DOI: `10.1109/7.845257`.

[17] A. Coluccia, A. Fascista, D. Orlando, and G. Ricci, "Adaptive radar detection in heterogeneous clutter plus thermal noise via the expectation-maximization algorithm," *IEEE Transactions on Aerospace and Electronic Systems*, vol. 60, no. 1, pp. 212–225, 2024. DOI: `10.1109/TAES.2023.3322389`.

[18] J. Ward, "Space-time adaptive processing for airborne radar," in *1995 International Conference on Acoustics, Speech, and Signal Processing*, vol. 5, 1995, 2809–2812 vol.5. DOI: `10.1109/ICASSP.1995.479429`.

[19] N. Yüksel, H. R. Börklü, H. K. Sezer, and O. E. Canyurt, "Review of artificial intelligence applications in engineering design perspective," *Engineering Applications of Artificial Intelligence*, vol. 118, p. 105 697, Feb. 1, 2023, ISSN: 0952-1976. DOI: `10.1016/j.engappai.2022.105697`. [Online]. Available: `https://www.sciencedirect.com/science/article/pii/S095219762200687X` (visited on 01/27/2025).

[20] Ø. G. Martinsen and A. Heiskanen, "Chapter 9 - data and models," in *Bioimpedance and Bioelectricity Basics (Fourth Edition)*, Ø. G. Martinsen and A. Heiskanen, Eds., Oxford: Academic Press, Jan. 1, 2023, pp. 345–433, ISBN: 9780128191071. DOI: `10.1016/B978-0-12-819107-1.00011-X`. [Online]. Available: `https://www.sciencedirect.com/science/article/pii/B978012819107100011X` (visited on 01/27/2025).

[21] L.-Y. Hu, M.-W. Huang, S.-W. Ke, and C.-F. Tsai, "The distance function effect on k-nearest neighbor classification for medical datasets," *SpringerPlus*, vol. 5, no. 1, p. 1304, Aug. 9, 2016, ISSN: 2193-1801. DOI: `10.1186/s40064-016-2941-7`. [Online]. Available: `https://doi.org/10.1186/s40064-016-2941-7` (visited on 04/10/2025).

[22] Z. Zhang, "Introduction to machine learning: K-nearest neighbors," *Annals of Translational Medicine*, vol. 4, no. 11, p. 218, Jun. 2016, ISSN: 2305-5839. DOI: `10.21037/atm.2016.03.37`. [Online]. Available: `https://www.ncbi.nlm.nih.gov/pmc/articles/PMC4916348/` (visited on 01/27/2025).

[23] M. Wu, W. Li, L. Yu, L. Sun, J. Liu, and W. Li, "Discovering mathematical expressions through DeepSymNet: A classification-based symbolic regression framework," *IEEE Transactions on Neural Networks and Learning Systems*, vol. 36, no. 1, pp. 1356–1370, Jan. 2025, ISSN: 2162-2388. DOI: `10.1109/TNNLS.2023.3332400`. [Online]. Available: `https://ieeexplore.ieee.org/document/10327762` (visited on 04/10/2025).

[24] R. G. S. Asthana, "CHAPTER 6 - evolutionary algorithms and neural networks," in *Soft Computing and Intelligent Systems*, ser. Academic Press Series in Engineering, N. K. Sinha and M. M. Gupta, Eds., San Diego: Academic Press, Jan. 1, 2000, pp. 111–136, ISBN: 9780126464900. DOI: `10.1016/B978-012646490-0/50009-3`. [Online]. Available: `https://www.sciencedirect.com/science/article/pii/B9780126464900500093` (visited on 04/10/2025).

[25] D. Ferrari, V. Guidetti, Y. Wang, and V. Curcin, "Multi-objective symbolic regression to generate data-driven, non-fixed structure and intelligible mortality predictors using EHR: Binary classification methodology and comparison with state-of-the-art," *AMIA ... Annual Symposium proceedings. AMIA Symposium*, vol. 2022, pp. 442–451, 2022, ISSN: 1942-597X.

[26] H. Wang, J. Xiong, Z. Yao, M. Lin, and J. Ren, "Research survey on support vector machine," in *Proceedings of the 10th EAI International Conference on Mobile Multimedia Communications*, Chongqing, People's Republic of China: EAI, 2017, ISBN: 9781631901560. DOI: `10.4108/eai.13-7-2017.2270596`. [Online]. Available: `http://eudl.eu/doi/10.4108/eai.13-7-2017.2270596` (visited on 04/29/2025).

[27] "1.4. support vector machines," scikit-learn. (), [Online]. Available: `https://scikit-learn/stable/modules/svm.html` (visited on 05/05/2025).

[28] "Torch.nn — PyTorch 2.7 documentation." (), [Online]. Available: `https://docs.pytorch.org/docs/stable/nn.html` (visited on 06/05/2025).

[29] "Introduction to GP — gplearn 0.4.2 documentation." (), [Online]. Available: `https://gplearn.readthedocs.io/en/stable/intro.html` (visited on 06/05/2025).

[30] "KNeighborsClassifier," scikit-learn. (), [Online]. Available: `https://scikit-learn/stable/modules/generated/sklearn.neighbors.KNeighborsClassifier.html` (visited on 06/05/2025).

[31] "SVC," scikit-learn. (), [Online]. Available: `https://scikit-learn/stable/modules/generated/sklearn.svm.SVC.html` (visited on 06/05/2025).

A

Eigenvalues and Clusters

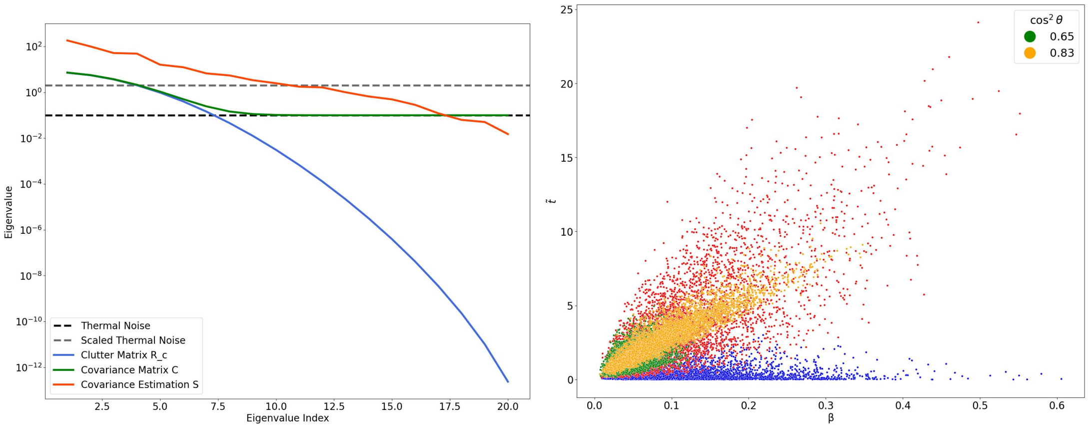

(a) K = NM eigenvalues. (b) K = NM.

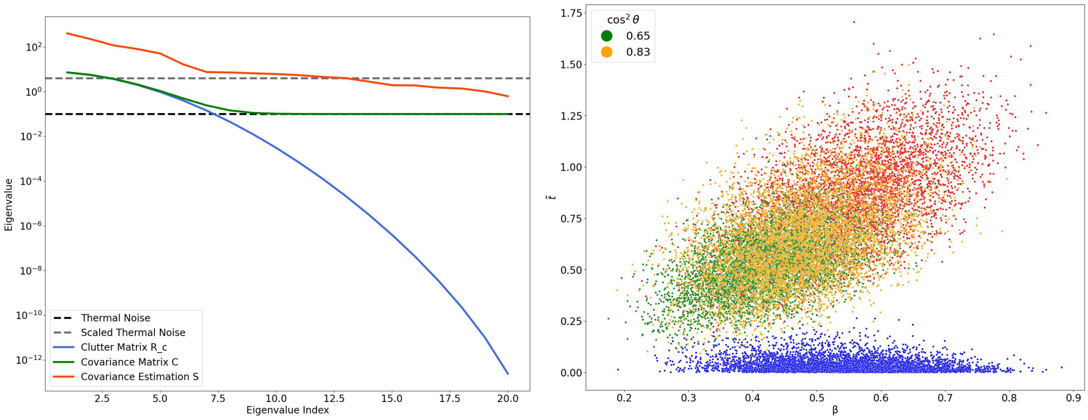

(c) K = 2NM eigenvalues. (d) K = 2NM.

Figure A.1: Eigenvalues and clusters at different values of K, N = 1 and M = 20, SNR = 16 dB.

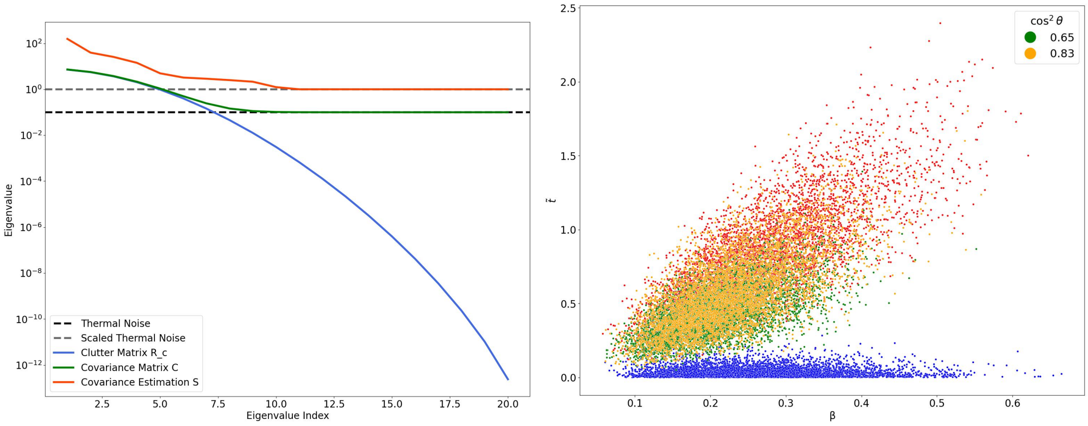

(a) K = 0.5NM, DL eigenvalues.

(b) K = 0.5NM, DL.

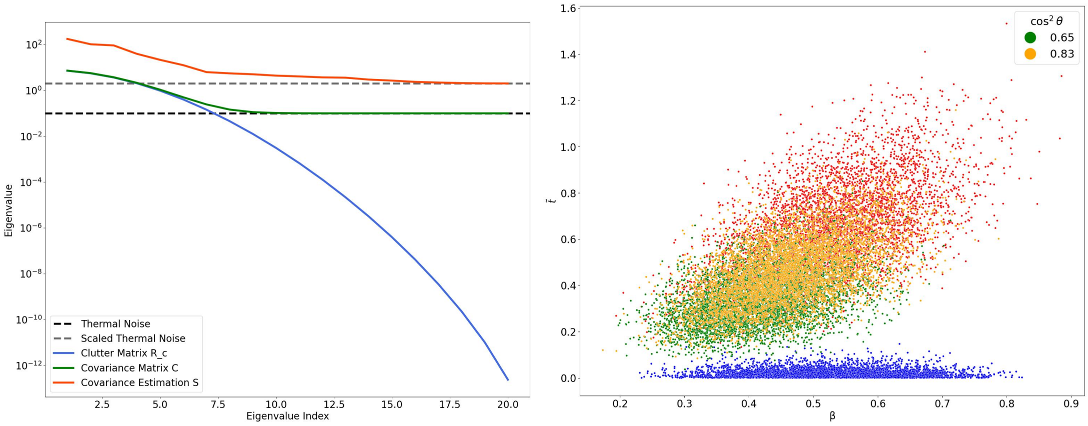

(c) K = NM, DL eigenvalues.

(d) K = NM, DL.

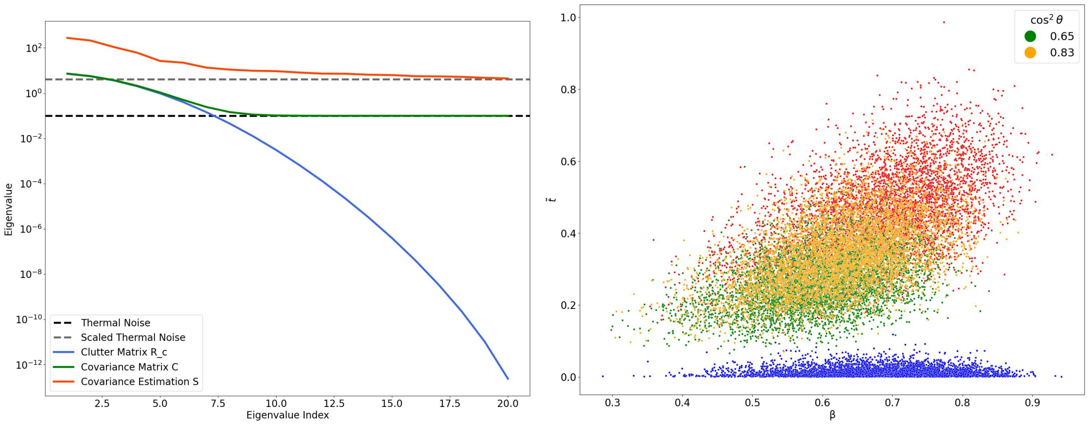

(e) K = 2NM, DL eigenvalues.

(f) K = 2NM, DL.

Figure A.2: Clustering results for diagonally loaded at different values of K, N = 1 and M = 20, SNR = 16 dB.

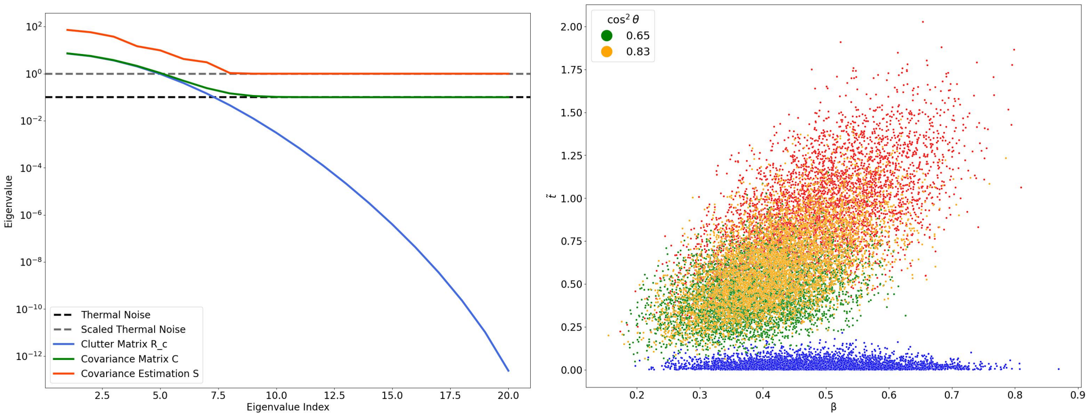

(a) K = 0.5NM, FML eigenvalues.

(b) K = 0.5NM, FML estimate.

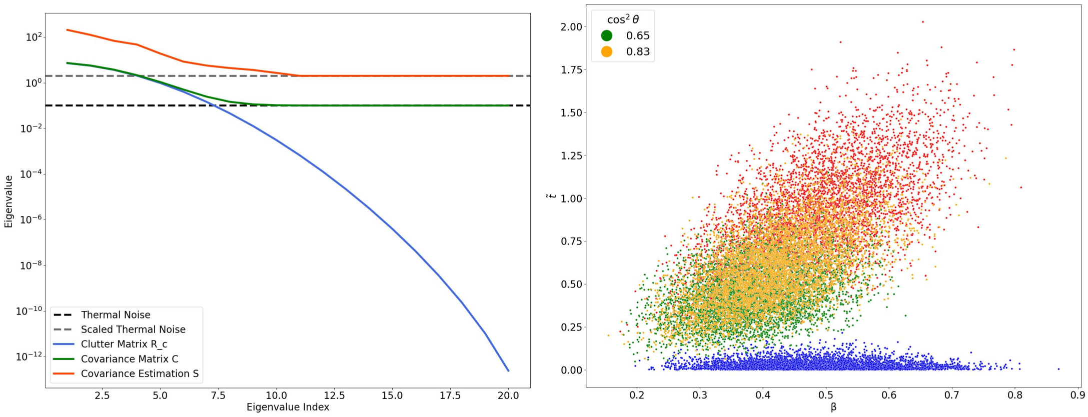

(c) K = NM, FML eigenvalues.

(d) K = NM, FML estimate.

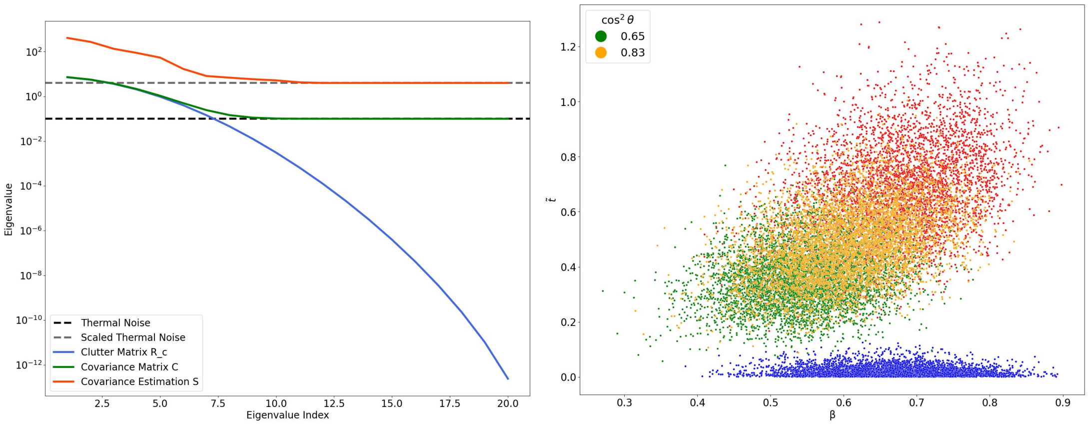

(e) K = 2NM, FML eigenvalues.

(f) K = 2NM, FML estimate.

Figure A.3: Eigenvalues and clusters at different values of K using FML, N = 1 and M = 20, SNR = 16 dB.

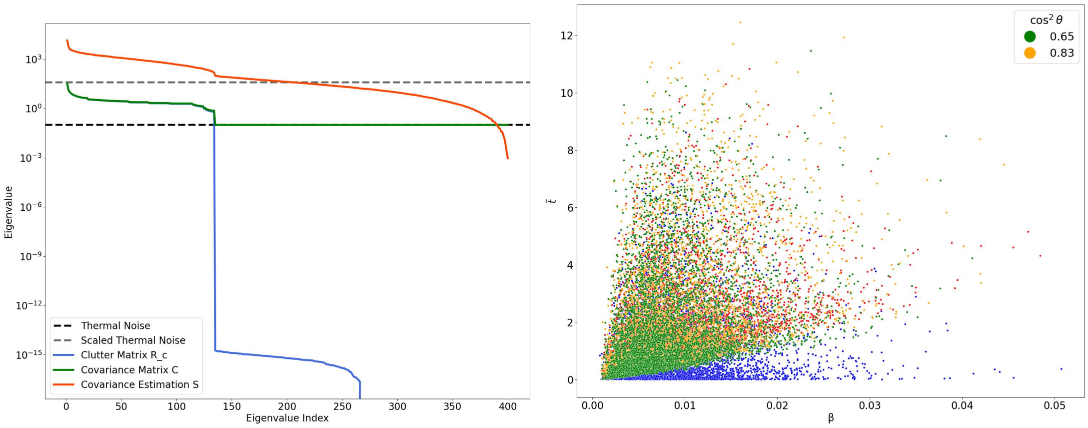

(a) K = NM eigenvalues.

(b) K = NM.

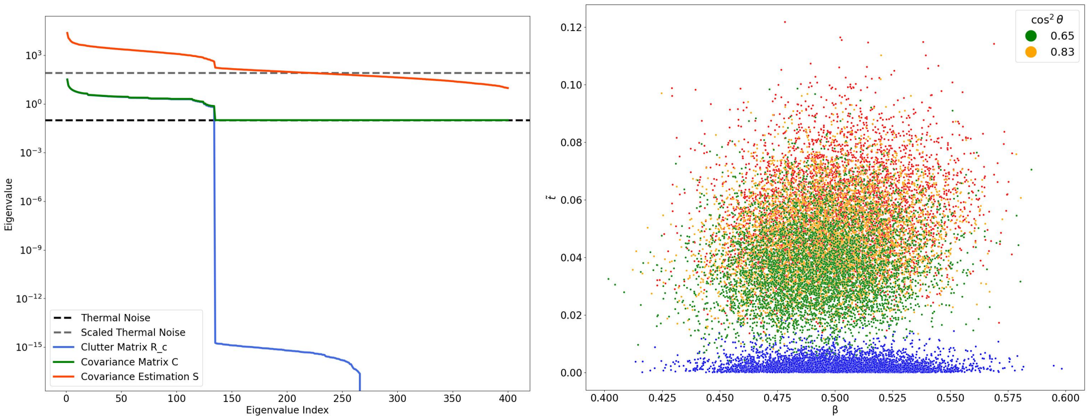

(c) K = 2NM eigenvalues.

(d) K = 2NM.

Figure A.4: Eigenvalues and clusters at different values of K, N = 20 and M = 20, SNR = 16 dB.

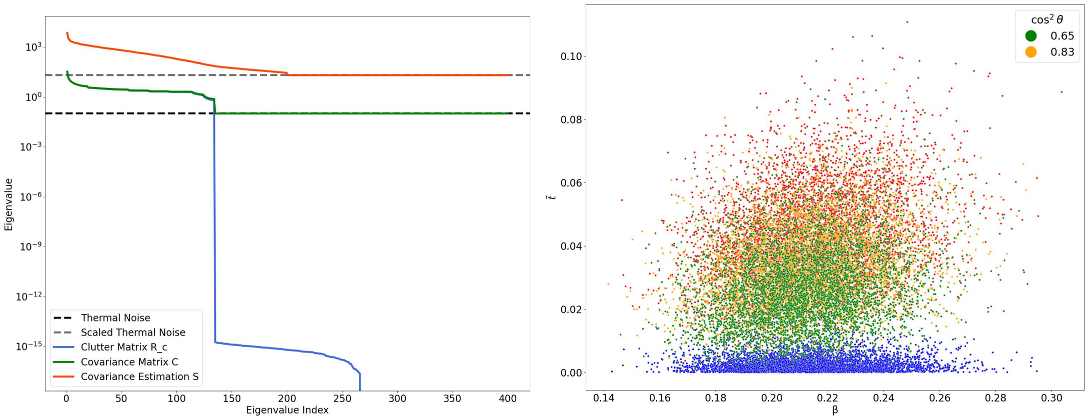

(a) K = 0.5NM, DL eigenvalues.

(b) K = 0.5NM, DL.

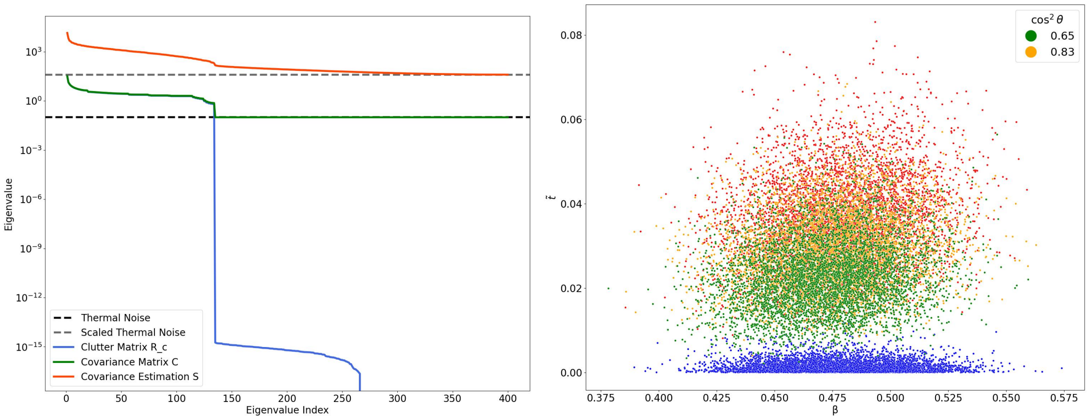

(c) K = NM, DL eigenvalues.

(d) K = NM, DL.

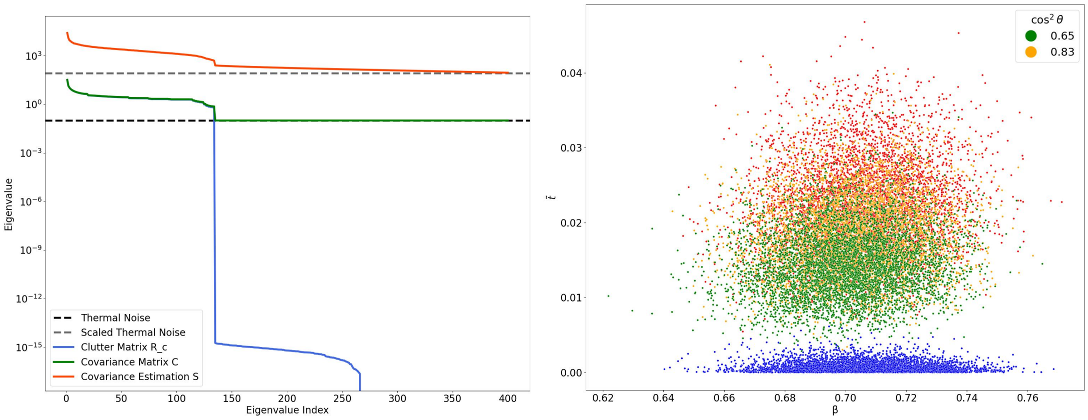

(e) K = 2NM, DL eigenvalues.

(f) K = 2NM, DL.

Figure A.5: Eigenvalues and clusters at different values of K using DL, N = 20 and M = 20, SNR = 16 dB.

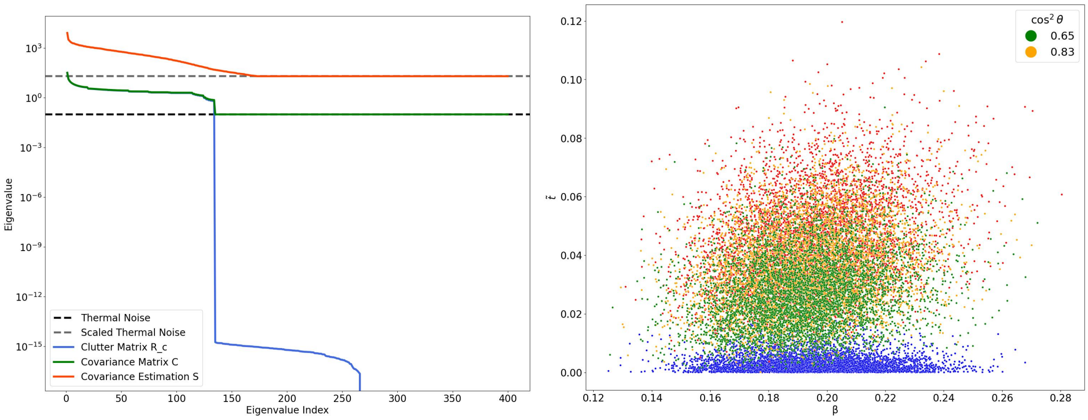

(a) K = 0.5NM, FML eigenvalues.   (b) K = 0.5NM, FML estimate.

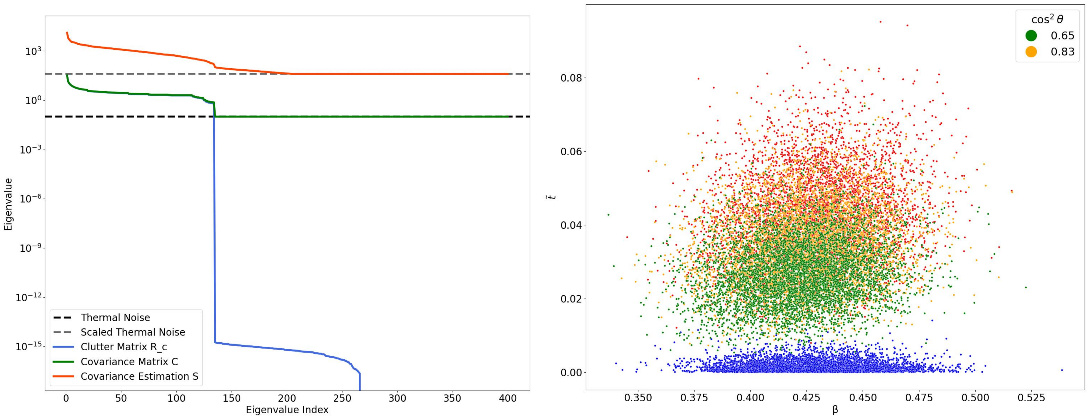

(c) K = NM, FML eigenvalues.   (d) K = NM, FML estimate.

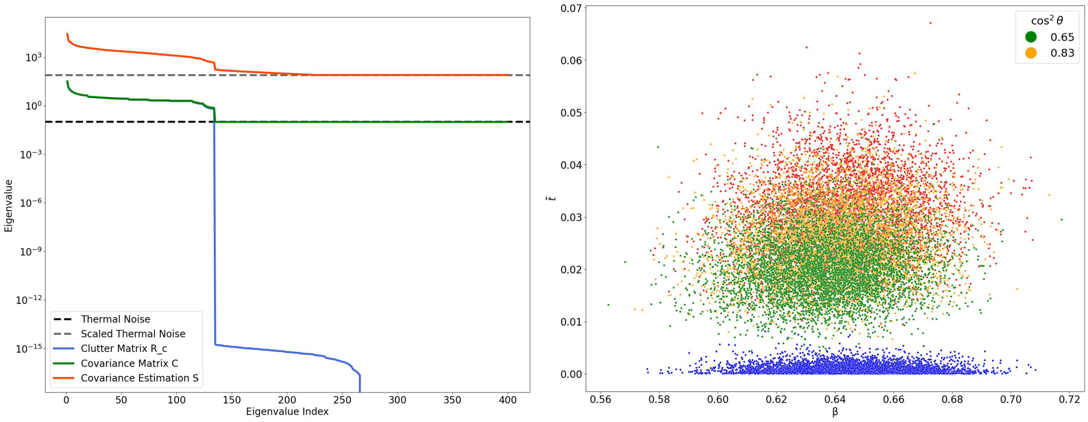

(e) K = 2NM, FML eigenvalues.   (f) K = 2NM, FML estimate.

Figure A.6: Eigenvalues and clusters at different values of K using FML, N = 20 and M = 20, SNR = 16 dB.

B

ML detectors - 1 antenna

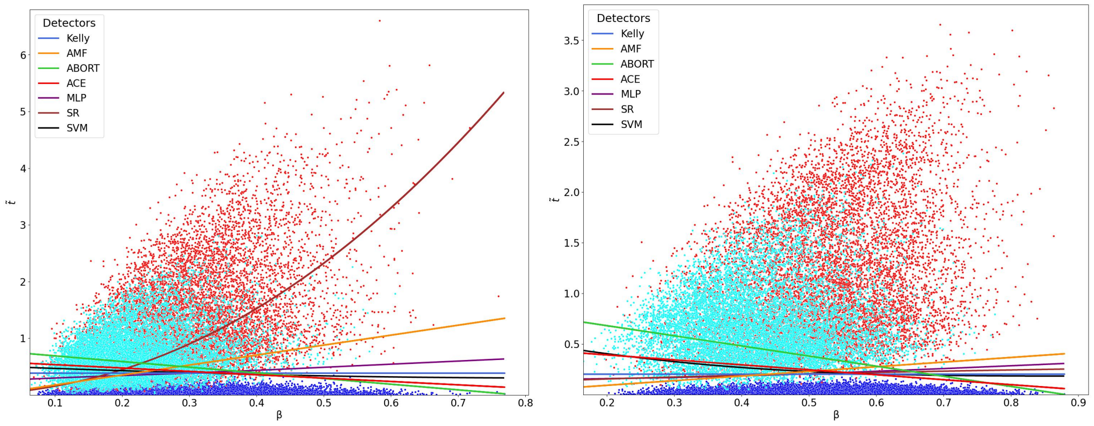

(a) K = 0.5NM with DL (b) K = NM with DL

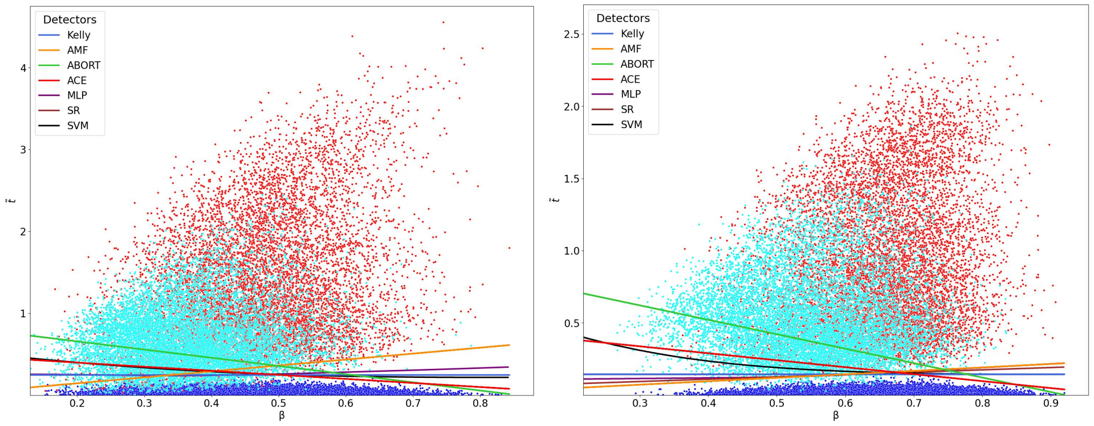

(c) K = NM with FML (d) K = 2NM with FML

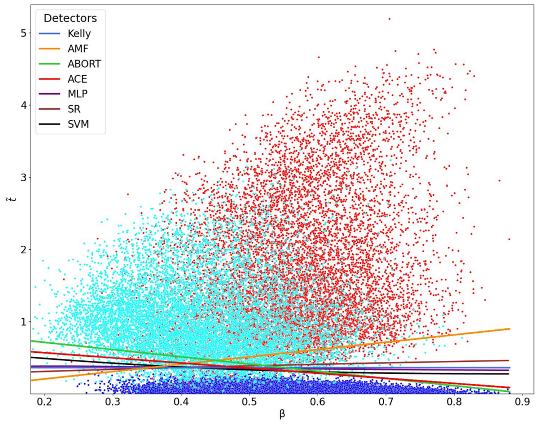

(e) K = 2NM

Figure B.1: Different detectors in CFAR-FP for 1 antenna

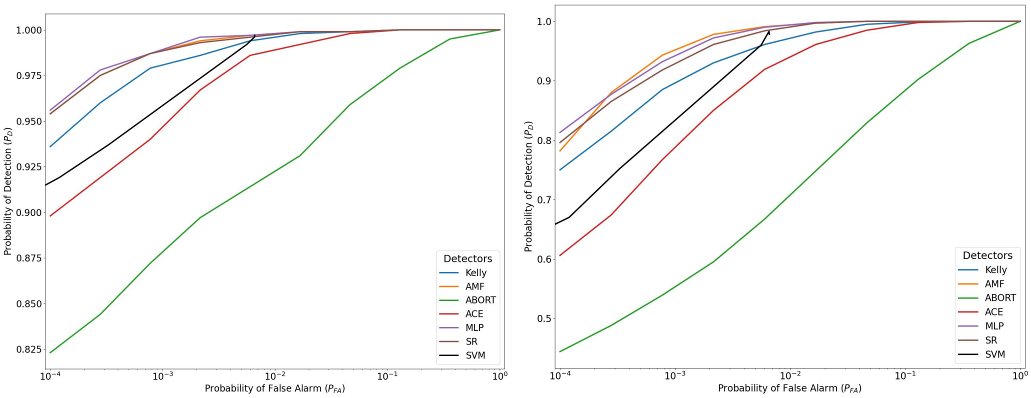

(a) ROC matched targets (b) ROC mismatched targets

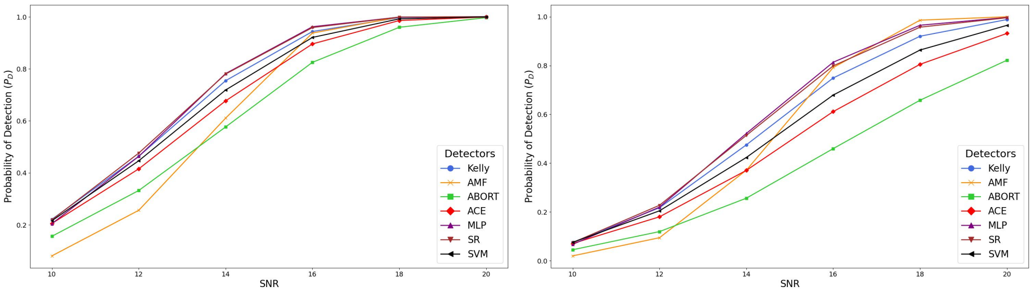

(c) SNR-P_d matched targets (d) SNR-P_d mismatched targets

Figure B.2: K = 0.5NM, Diagonally loaded

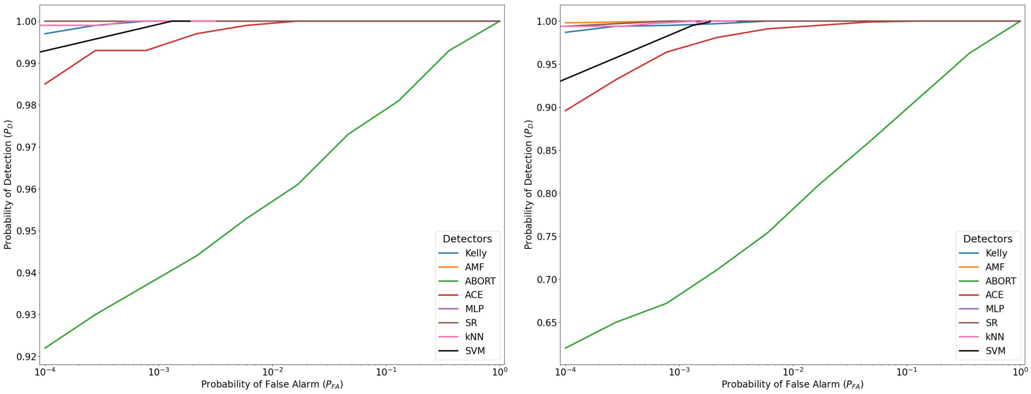

(a) ROC matched targets (b) ROC mismatched targets

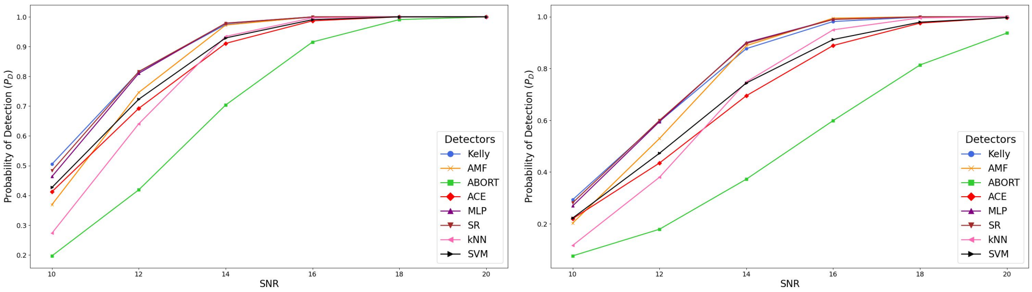

(c) SNR-P_d matched targets (d) SNR-P_d mismatched targets

Figure B.3: K = NM, Diagonally loaded

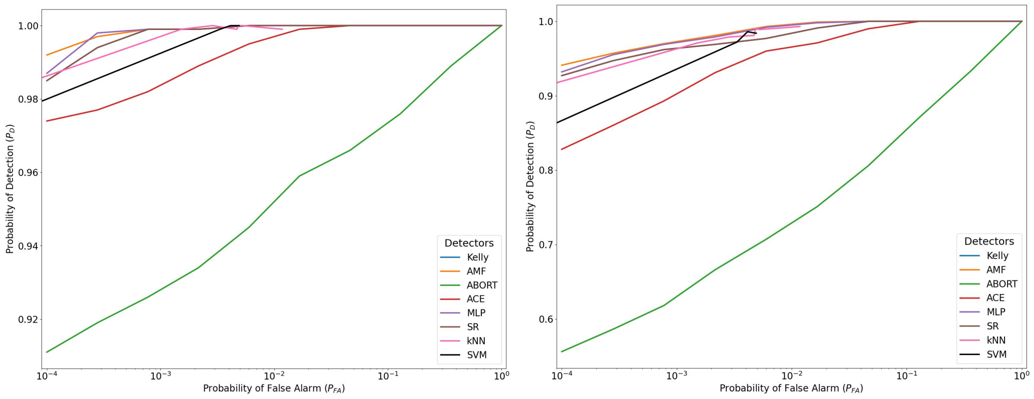

(a) ROC matched targets (b) ROC mismatched targets

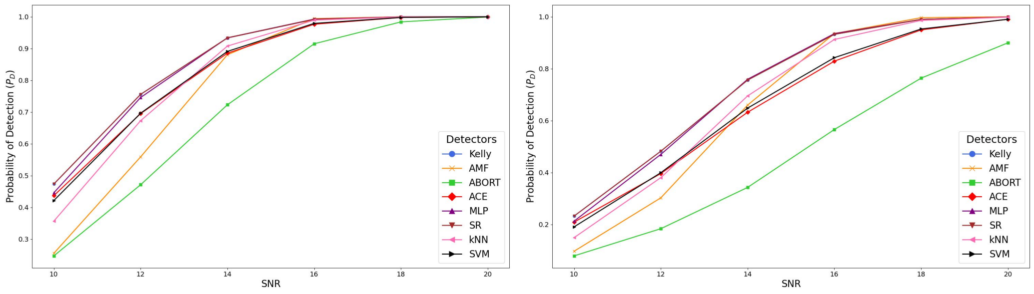

(c) SNR-P_d matched targets (d) SNR-P_d mismatched targets

Figure B.4: K = NM, FML estimate

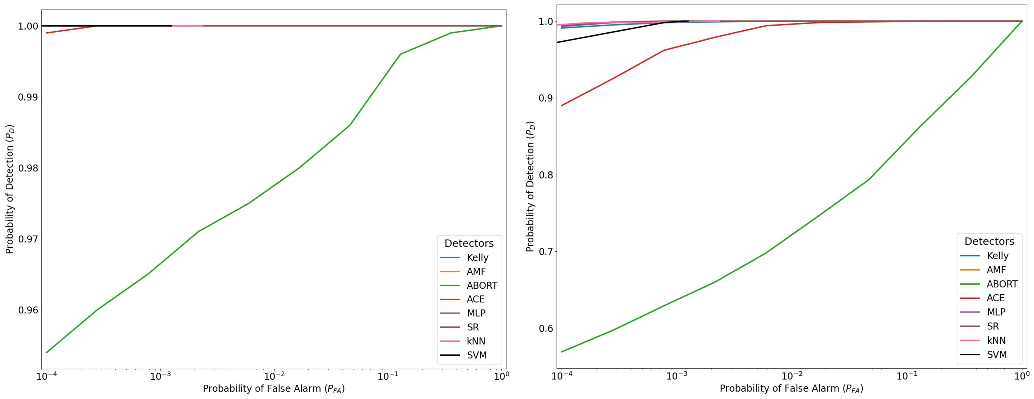

(a) ROC matched targets (b) ROC mismatched targets

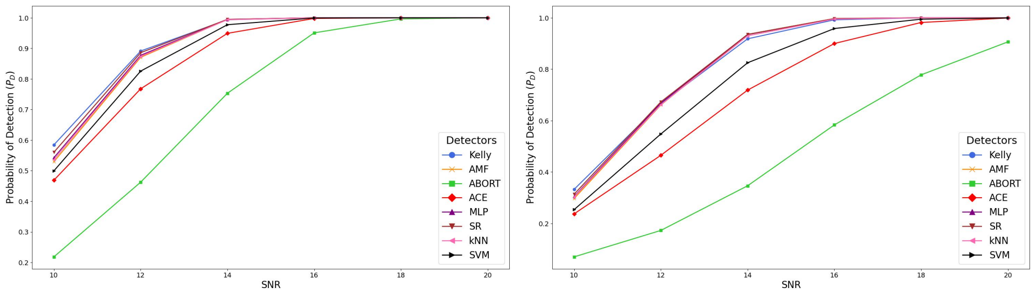

(c) SNR-P_d matched targets (d) SNR-P_d mismatched targets

Figure B.5: K = 2NM, FML estimate

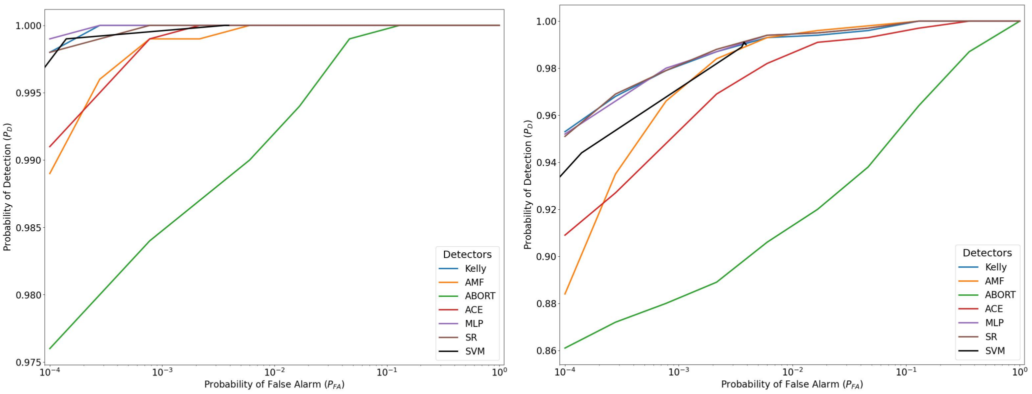

(a) ROC matched targets (b) ROC mismatched targets

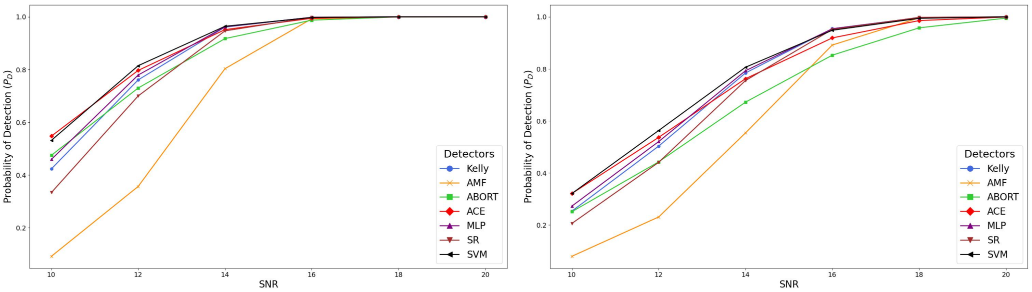

(c) SNR-P_d matched targets (d) SNR-P_d mismatched targets

Figure B.6: K = 2NM

C

ML detectors - 20 antennas

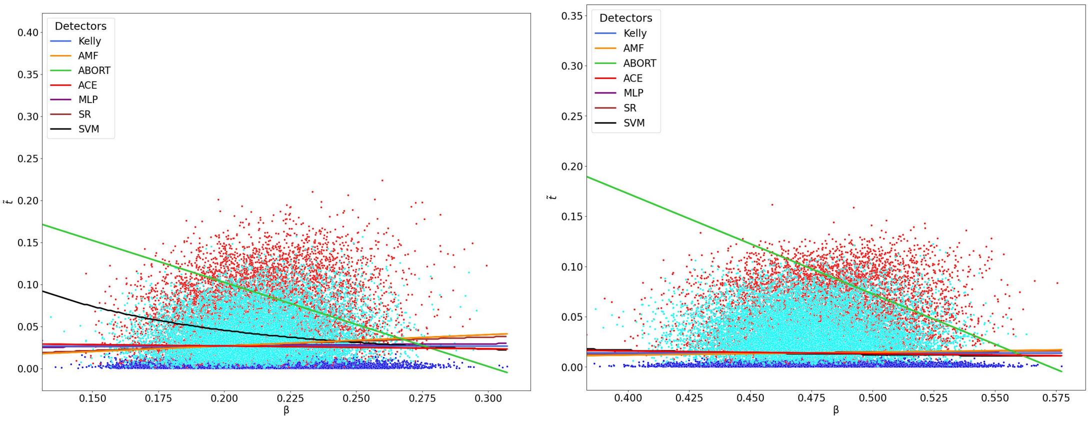

(a) K = 0.5NM with DL

(b) K = NM with DL

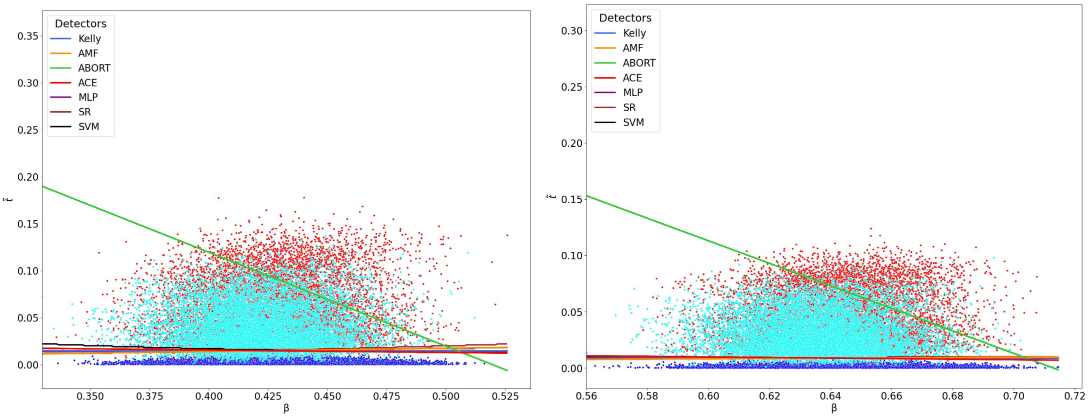

(c) K = NM with FML

(d) K = 2NM with FML

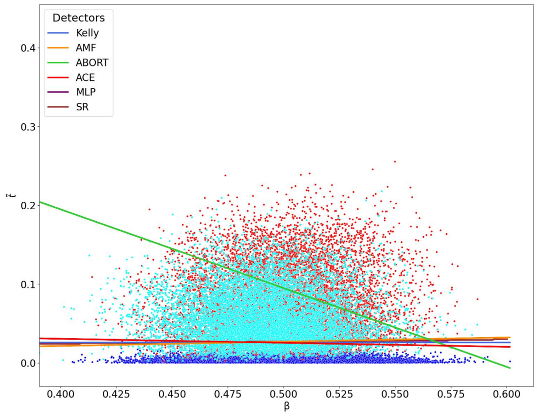

(e) K = 2NM

Figure C.1: Different detectors in the CFAR-FP for 20 antennas

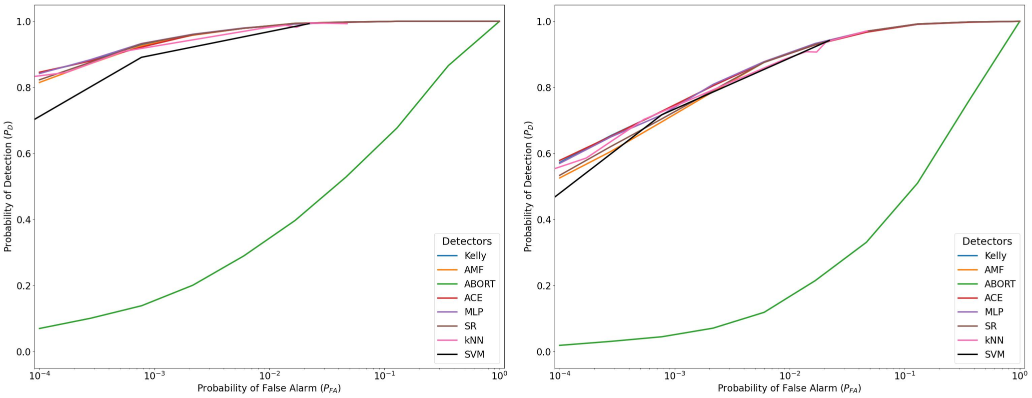

(a) ROC matched targets (b) ROC mismatched targets

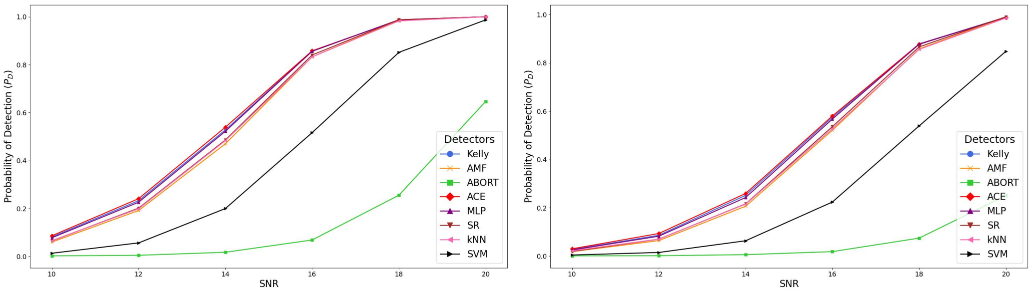

(c) SNR-P_d matched targets (d) SNR-P_d mismatched targets

Figure C.2: K = 0.5NM, Diagonally loaded

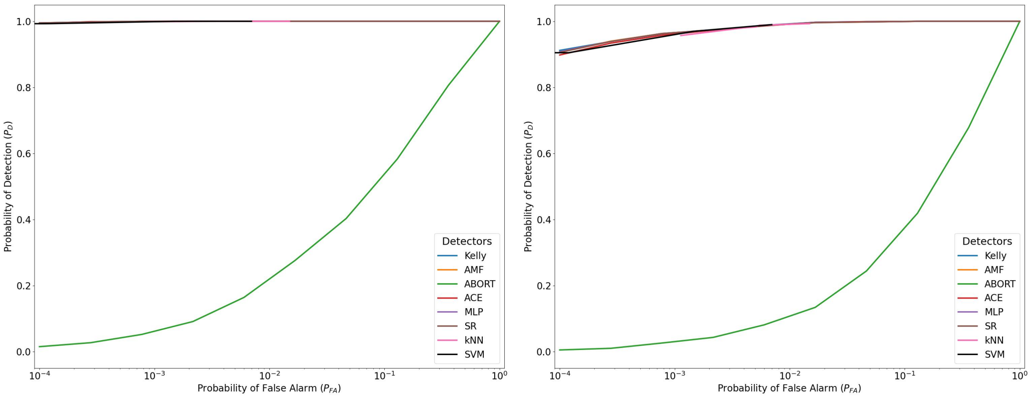

(a) ROC matched targets (b) ROC mismatched targets

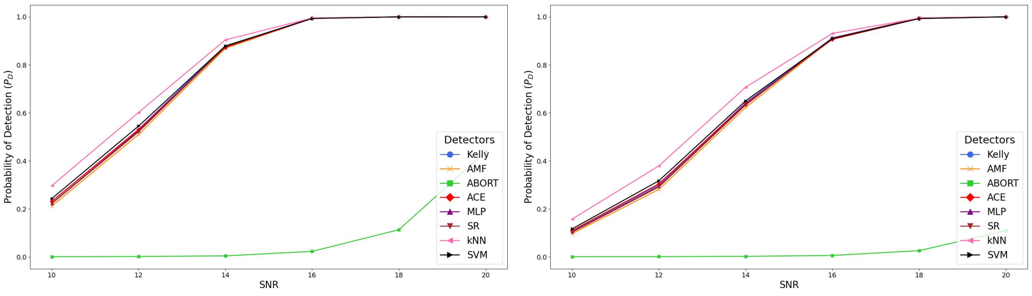

(c) SNR-P_d matched targets (d) SNR-P_d mismatched targets

Figure C.3: K = NM, Diagonally loaded

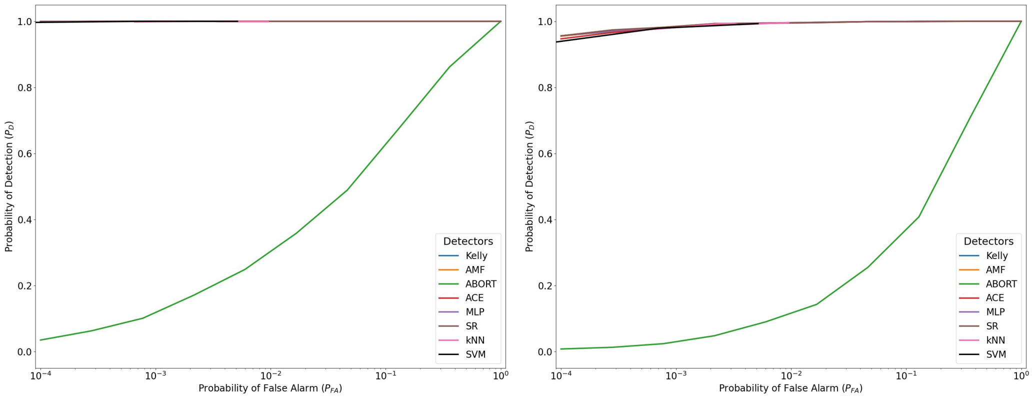

(a) ROC matched targets (b) ROC mismatched targets

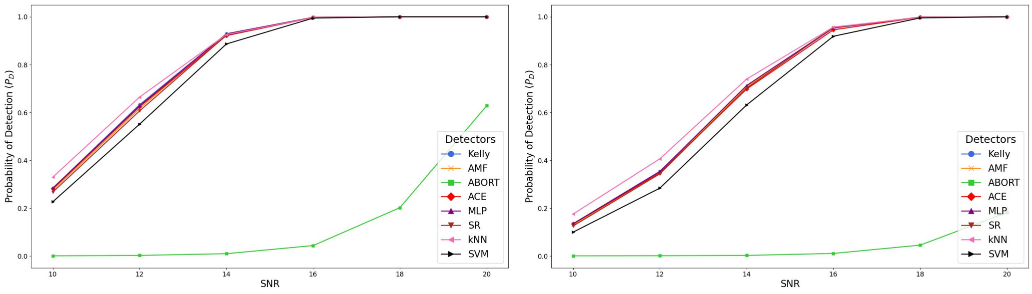

(c) SNR-P_d matched targets (d) SNR-P_d mismatched targets

Figure C.4: K = NM, FML estimate

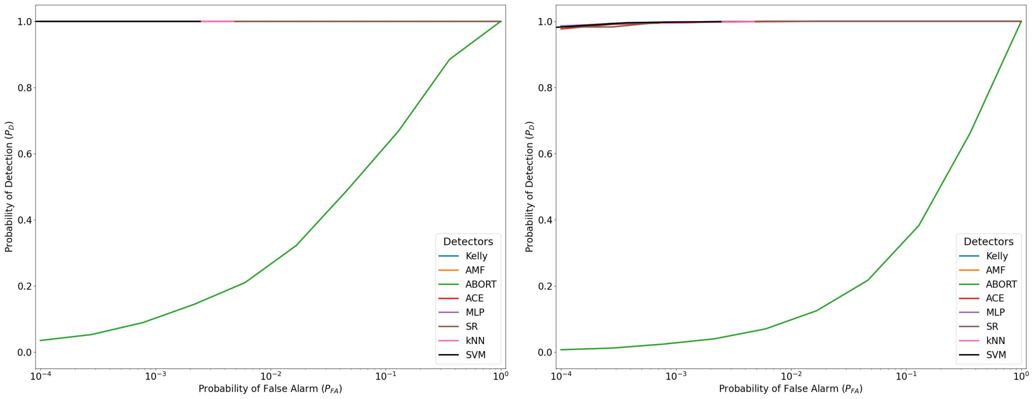

(a) ROC matched targets (b) ROC mismatched targets

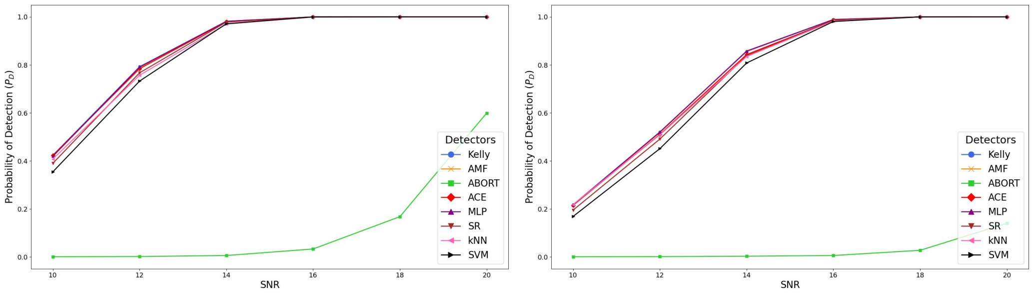

(c) SNR-P_d matched targets (d) SNR-P_d mismatched targets

Figure C.5: K = 2NM, FML estimate

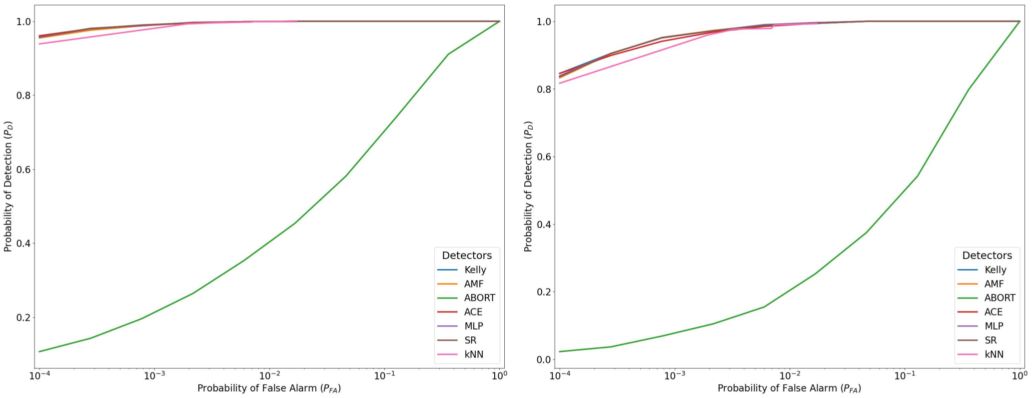

(a) ROC matched targets (b) ROC mismatched targets

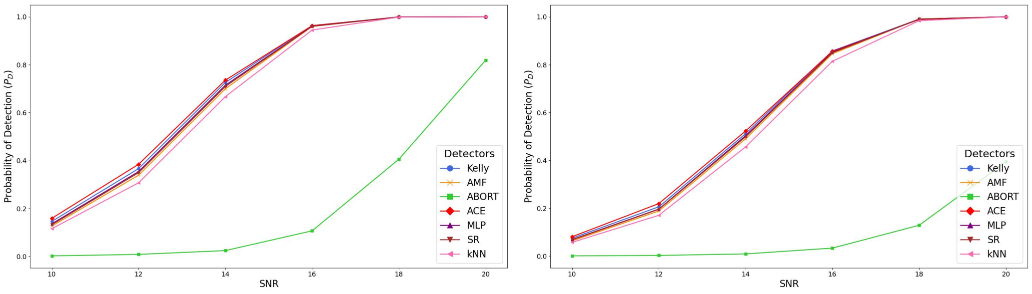

(c) SNR-P_d matched targets (d) SNR-P_d mismatched targets

Figure C.6: K = 2NM

D

Final Evaluation

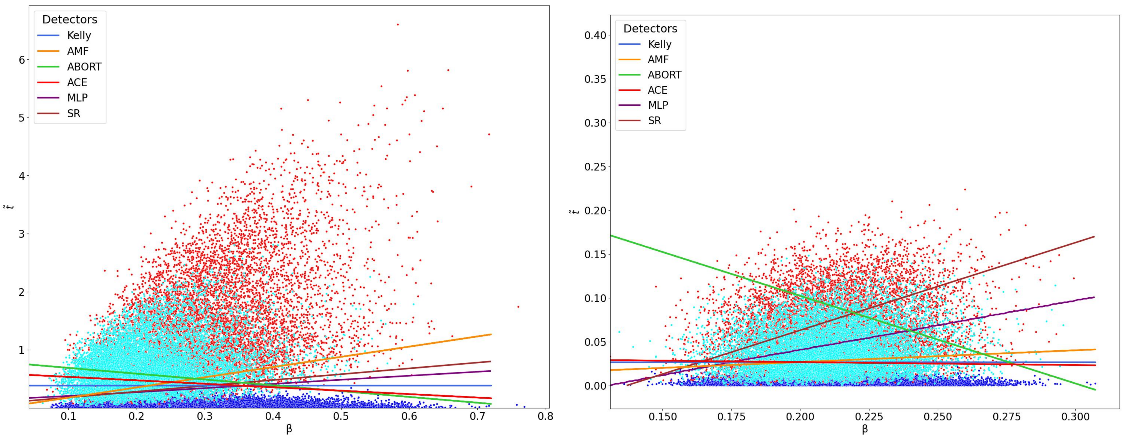

(a) K = 0.5NM with DL, Case 1

(b) K = 0.5NM with DL, Case 2

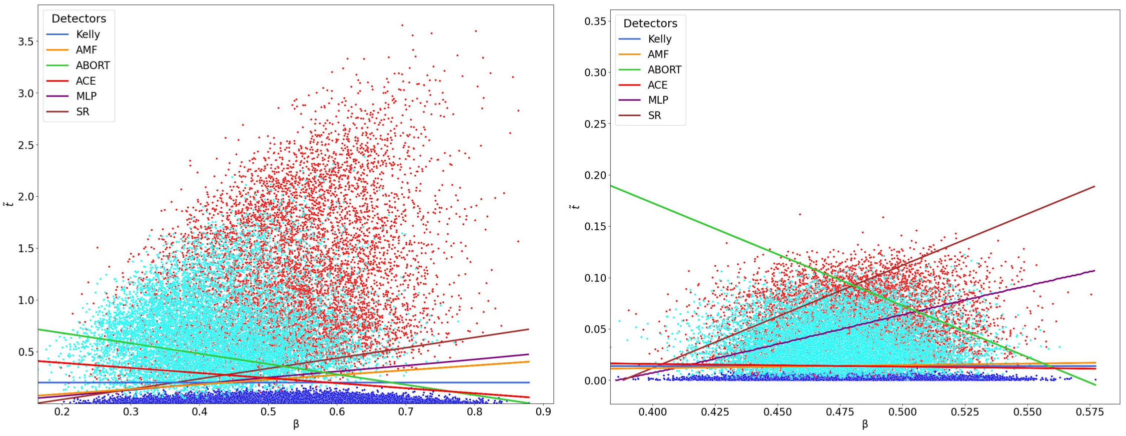

(c) K = NM with DL, Case 1

(d) K = NM with DL, Case 2

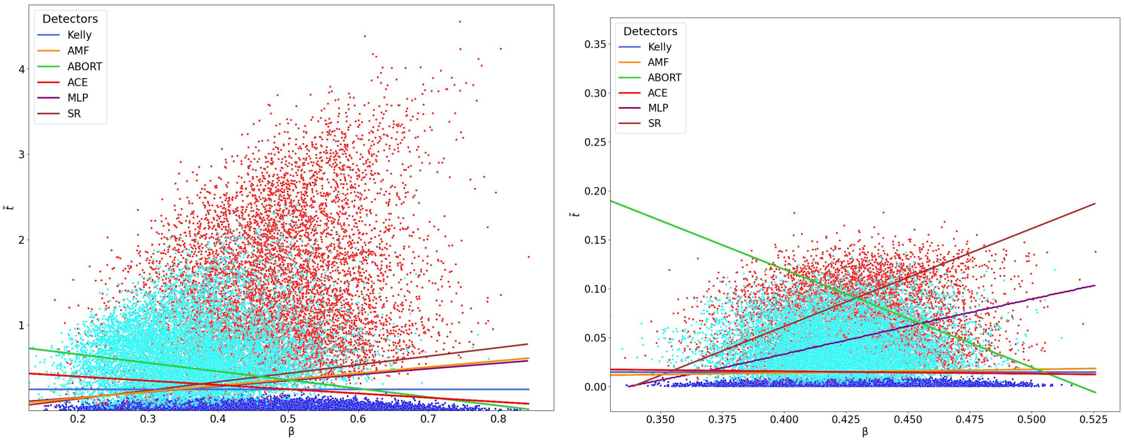

(e) K = NM with FML, Case 1

(f) K = NM with FML, Case 2

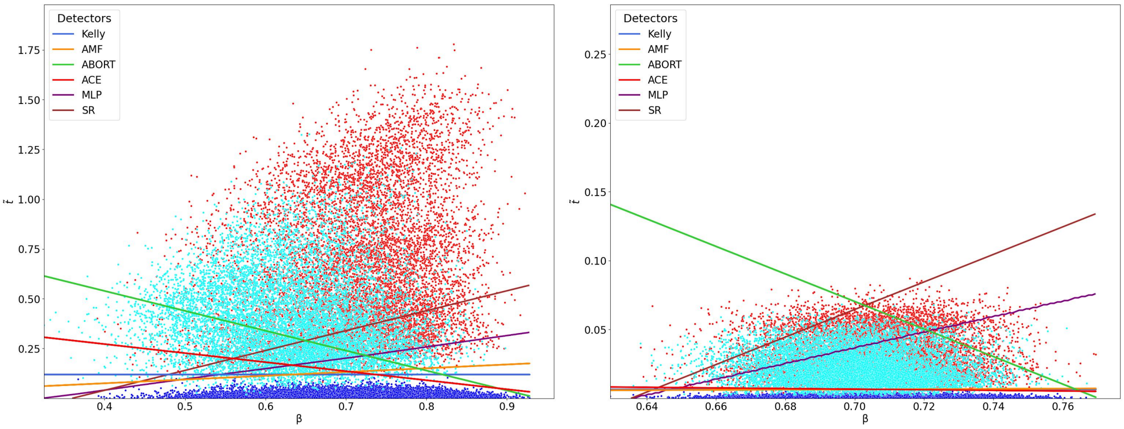

(g) K = 2NM with DL, Case 1

(h) K = 2NM with DL, Case 2

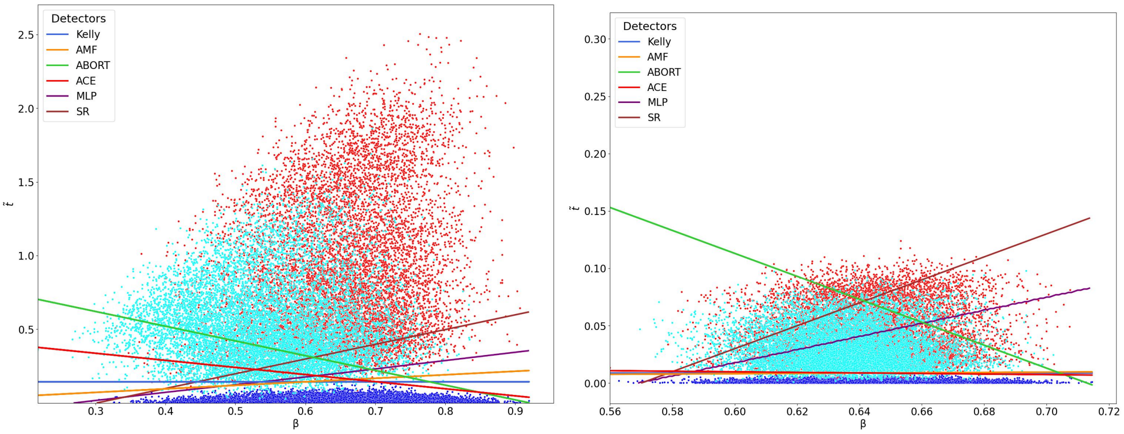

(i) K = 2NM with FML, Case 1

(j) K = 2NM with FML, Case 2

Figure D.1: Different detectors in the CFAR-FP with detectors trained on K = 0.5NM with FML for Case 1.

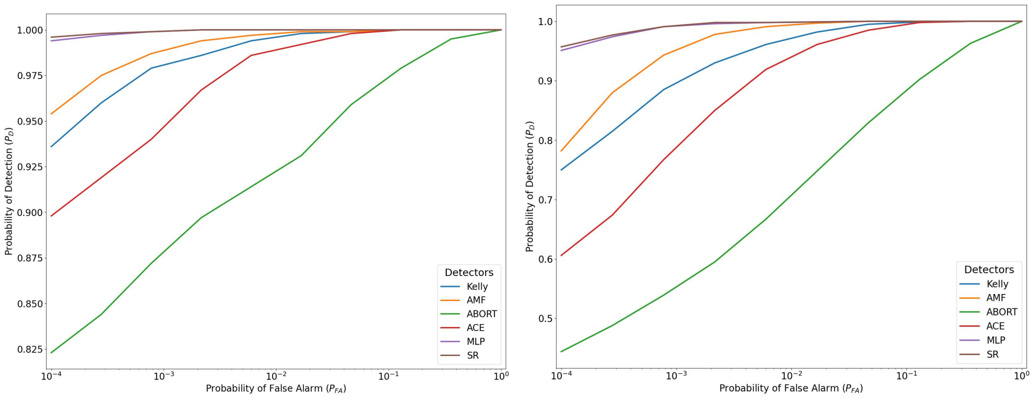

(a) ROC matched targets (b) ROC mismatched targets

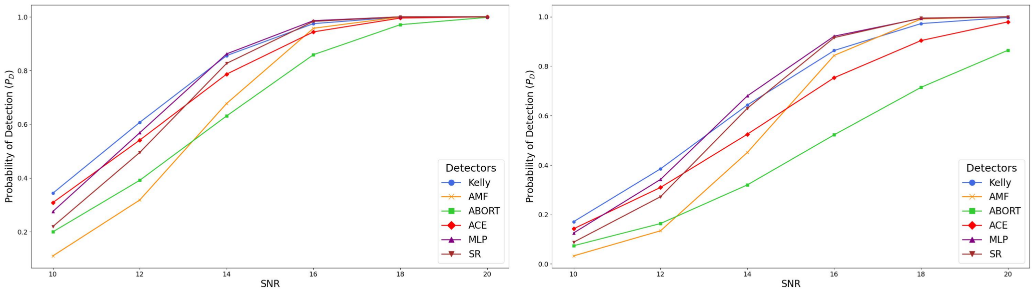

(c) SNR-P_d matched targets (d) SNR-P_d mismatched targets

Figure D.2: K = 0.5NM, Diagonally loaded, Case 1

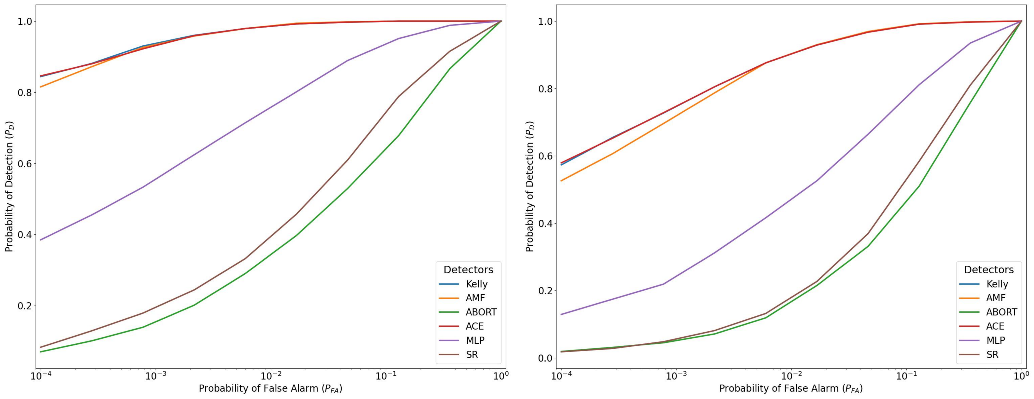

(a) ROC matched targets (b) ROC mismatched targets

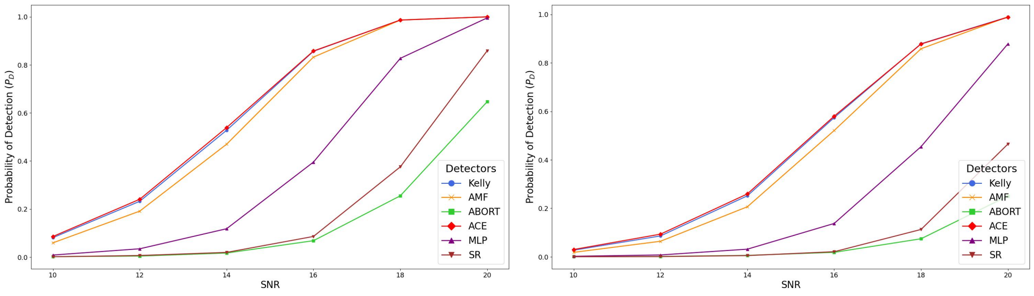

(c) SNR-P_d matched targets (d) SNR-P_d mismatched targets

Figure D.3: K = 0.5NM, Diagonally loaded, Case 2

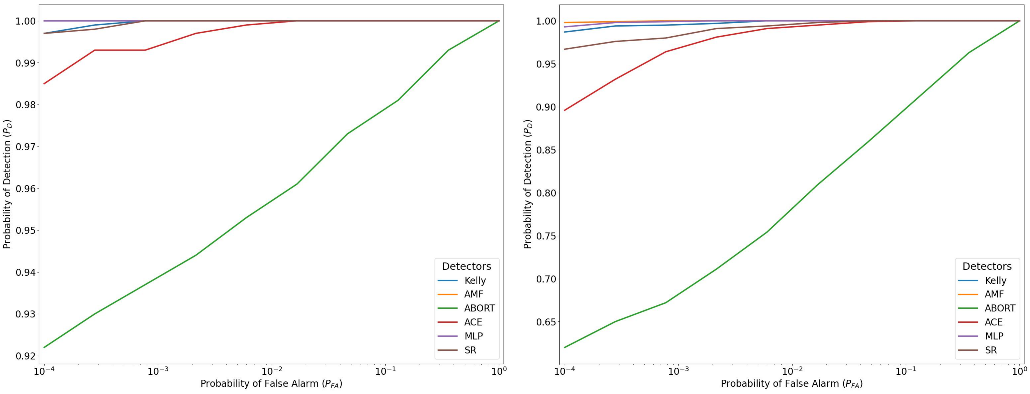

(a) ROC matched targets (b) ROC mismatched targets

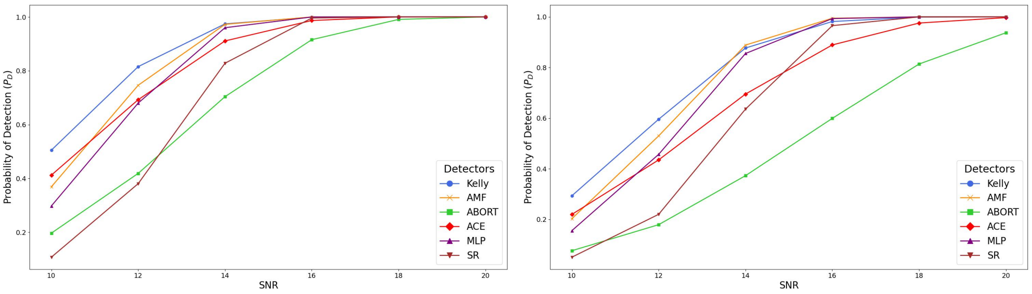

(c) SNR-P_d matched targets (d) SNR-P_d mismatched targets

Figure D.4: K = NM, Diagonally loaded, Case 1

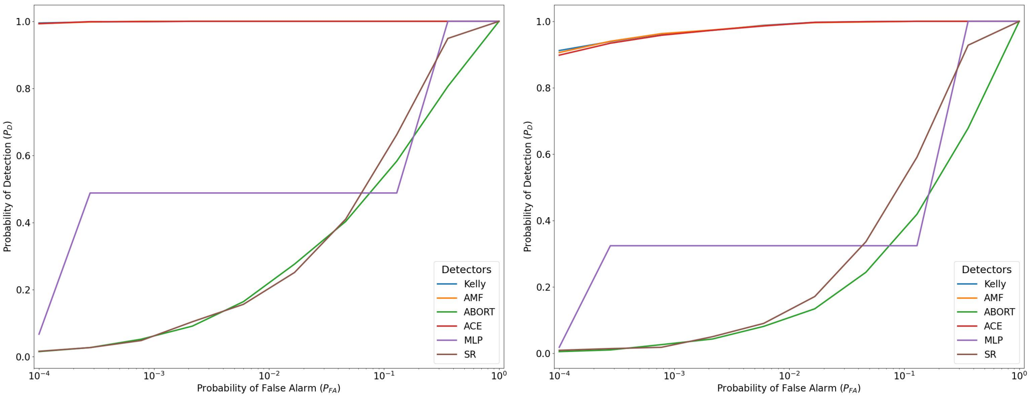

(a) ROC matched targets (b) ROC mismatched targets

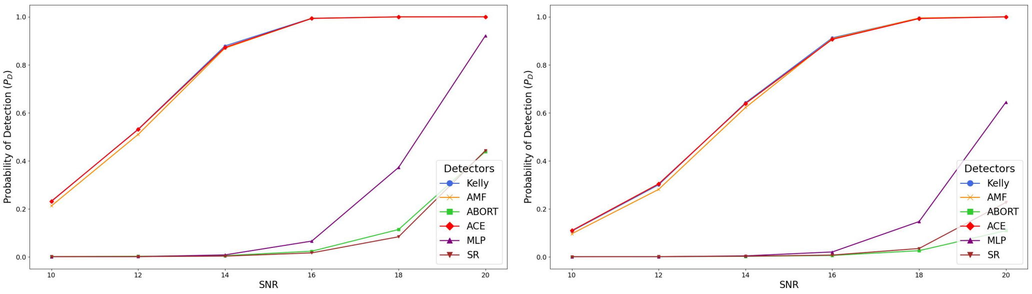

(c) SNR-P_d matched targets (d) SNR-P_d mismatched targets

Figure D.5: K = NM, Diagonally loaded, Case 2

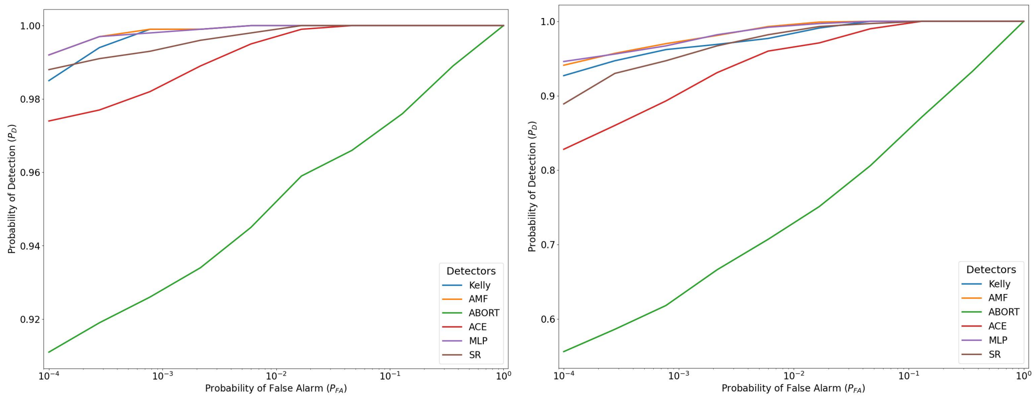

(a) ROC matched targets (b) ROC mismatched targets

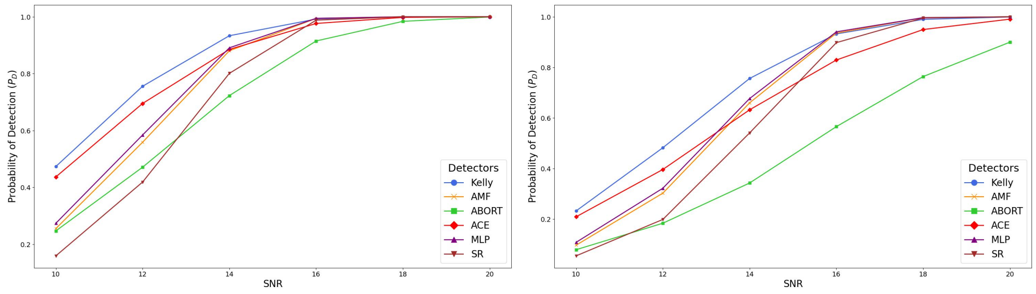

(c) SNR-P_d matched targets (d) SNR-P_d mismatched targets

Figure D.6: K = NM, FML estimated, Case 1

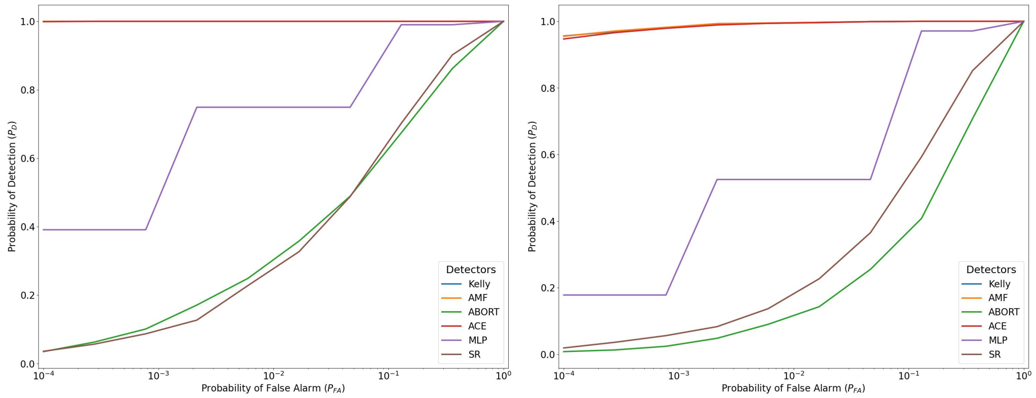

(a) ROC matched targets (b) ROC mismatched targets

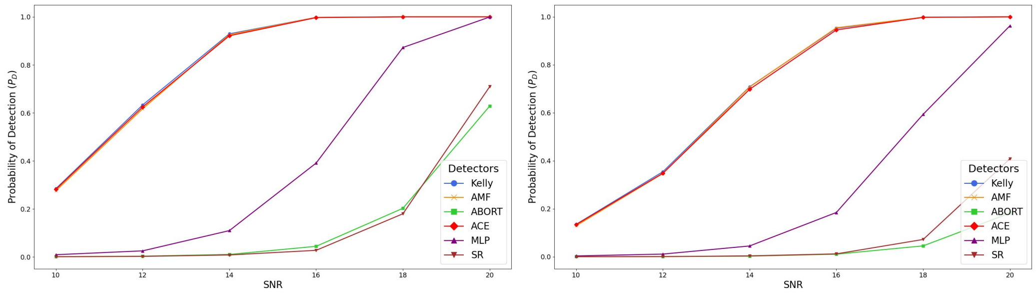

(c) SNR-P_d matched targets (d) SNR-P_d mismatched targets

Figure D.7: K = NM, FML estimated, Case 2

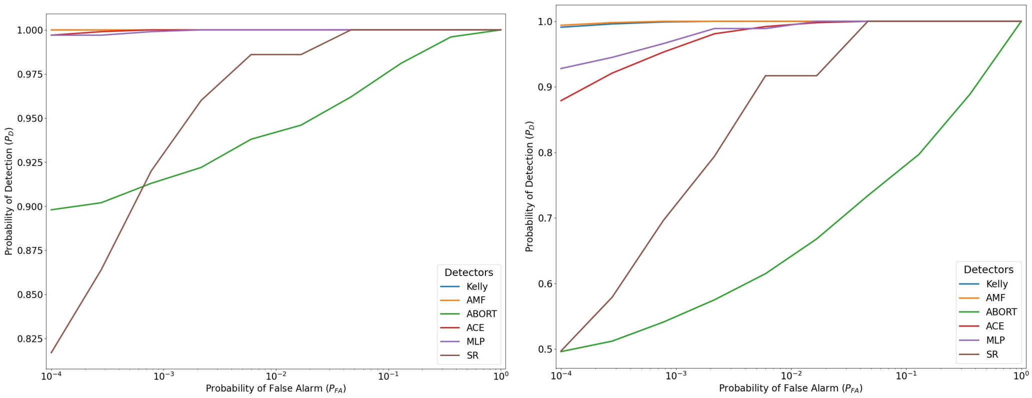

(a) ROC matched targets (b) ROC mismatched targets

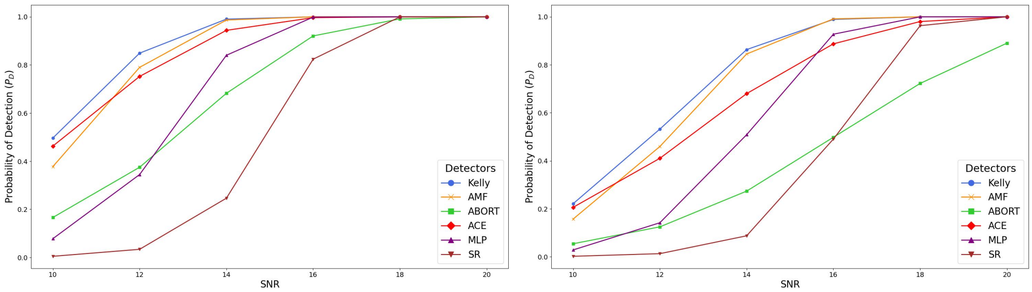

(c) SNR-P_d matched targets (d) SNR-P_d mismatched targets

Figure D.8: K = 2NM, Diagonally Loaded, Case 1

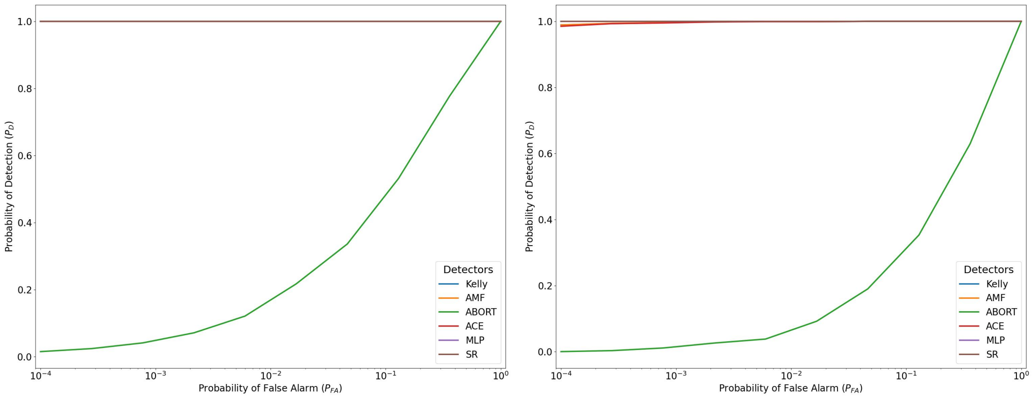

(a) ROC matched targets (b) ROC mismatched targets

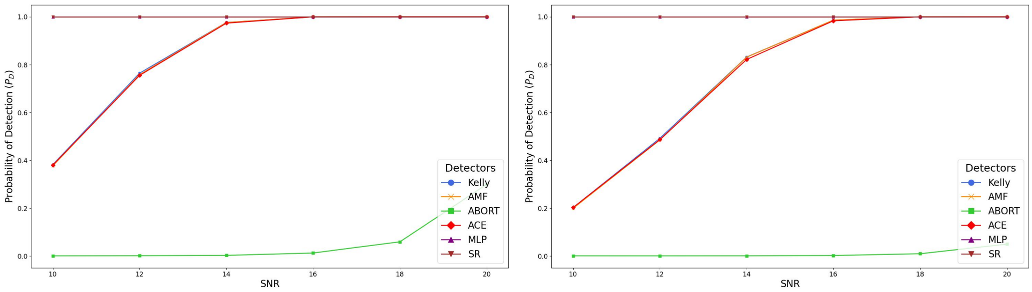

(c) SNR-P_d matched targets (d) SNR-P_d mismatched targets

Figure D.9: K = 2NM, Diagonally loaded, Case 2

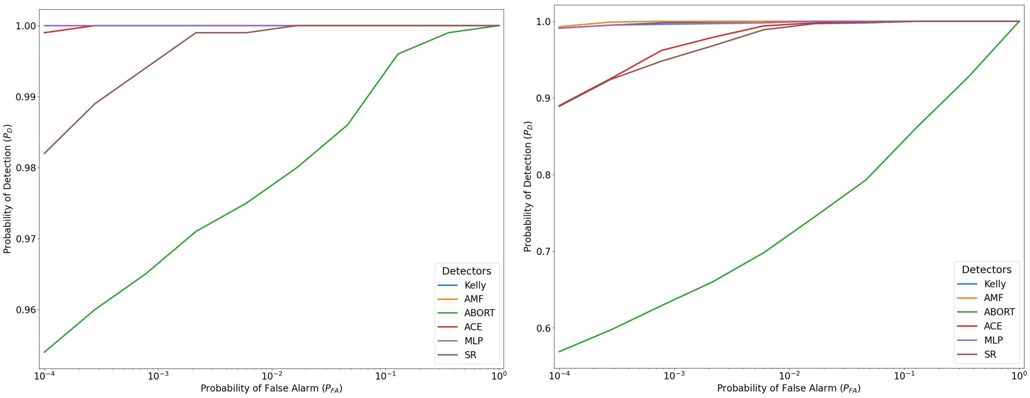

(a) ROC matched targets (b) ROC mismatched targets

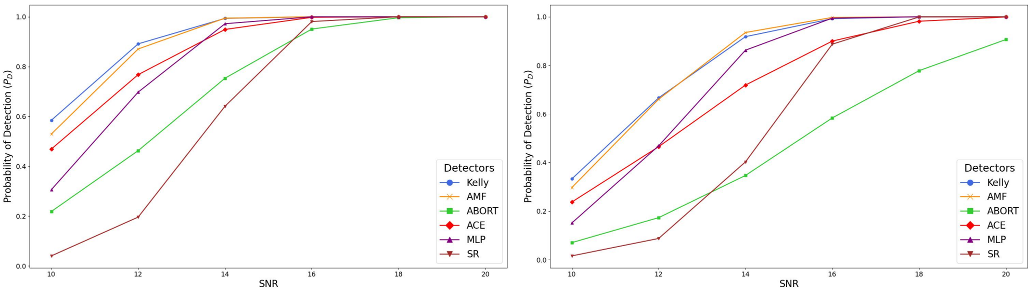

(c) SNR-P_d matched targets (d) SNR-P_d mismatched targets

Figure D.10: K = 2NM, FML estimated, Case 1

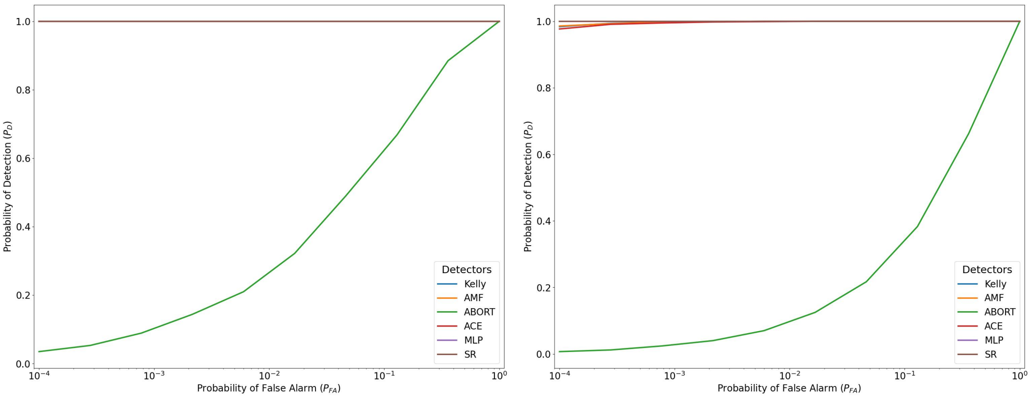

(a) ROC matched targets (b) ROC mismatched targets

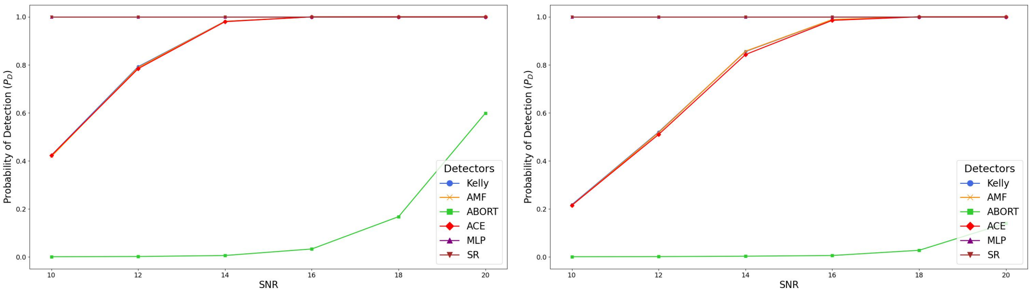

(c) SNR-P_d matched targets (d) SNR-P_d mismatched targets

Figure D.11: K = 2NM, FML estimated, Case 2

DEPARTMENT OF ELECTRICAL ENGINEERING
CHALMERS UNIVERSITY OF TECHNOLOGY
Gothenburg, Sweden
www.chalmers.se